

GAMMA-RAY SPECTROSCOPY AND
LIFETIME MEASUREMENTS OF
NUCLEI IN THE $A = 70$, $N = Z$
REGION

ADAM JACOB NICHOLS

PH.D

UNIVERSITY OF YORK

PHYSICS

May 2014

Abstract

An experiment was performed at the National Superconducting Cyclotron Laboratory at Michigan State University, USA. Transition strengths for γ decays from low-lying excited states in $A \sim 70$ nuclei have been deduced from lifetime measurements using the recoil distance Doppler shift and γ -ray lineshape methods in conjunction with nucleon knockout and inelastic scattering reactions. The results confirm the collectivity previously reported for the $2_1^+ \rightarrow 0_{gs}^+$ decay in ^{68}Se and reveal a relative decrease in collectivity in ^{70}Br . This trend is reproduced by shell model calculations using the GXPF1A interaction in the fp model space including the Coulomb, spin-orbit and isospin non-conserving interactions. The $3_1^+ \rightarrow 2_1^+$ decay in ^{70}Br is found to have a very small $B(M1)$ value, which is consistent with the configuration of the state being dominated by the coupling of $f_{5/2}$ and $p_{1/2}$ nucleons. The results suggest the $g_{9/2}$ orbit does not play an important role at low spin in these nuclei. The $B(E2)$ values for the decays of the ($\mathbf{T} = 1$) 2_1^+ states in ^{70}Br and ^{70}Se are almost identical, suggesting there is no major shape change between the two nuclei at low spin. New γ rays have been identified in ^{68}Se and ^{69}Se . γ - γ coincidence measurements have allowed one of the two new γ rays observed in ^{69}Se to be placed in the level scheme. Shell model calculations with the GXPF1A interaction in the fp model space suggest that this new γ ray comes from a previously unobserved excited $\frac{1}{2}^-$ state. Lifetimes of excited states in ^{72}Kr , ^{66}Ge , ^{69}Se and ^{65}Ga have also been extracted and, where possible, compared to previous work.

Contents

Abstract	2
List of Figures	6
List of Tables	9
Acknowledgements	10
Declaration	11
1 Introduction	12
2 Theoretical Considerations	19
2.1 Nuclear Models	19
2.1.1 The Shell Model	19
2.1.2 Models Used In This Work	22
2.2 Isospin Formalism	24
2.3 Reaction Mechanisms	27
2.3.1 Nucleon Knockout	27
2.3.2 Coulomb Excitation	28
2.4 Electromagnetic Transition Theory	28
2.5 Quasideuteron Configurations	30
3 Experimental Details	32
3.1 Beam Production	32
3.1.1 The Ion Source	32
3.1.2 Primary Beam Acceleration	33
3.1.3 The A1900: Secondary Beam Separation	34
3.2 Experimental Devices	36

3.2.1	The S800 Spectrograph	36
3.2.2	The Segmented Germanium Array	40
3.2.3	Data Acquisition System	44
3.3	Experimental Techniques	45
3.3.1	The Recoil Distance Doppler Shift Method	45
3.3.2	The γ -ray Lineshape Method	51
3.3.3	The TRIPLEX Plunger	52
4	Data Analysis	56
4.1	Offline Analysis With ROOT	56
4.2	Focal Plane Corrections And Calibrations	57
4.2.1	Recoil Trajectory Reconstruction	58
4.2.2	Scintillator And CRDC Corrections And Calibrations	59
4.2.3	Ion Chamber Corrections And Calibrations	61
4.2.4	SeGA Corrections And Calibrations	63
4.3	Obtaining Recoil-gated γ -ray Spectra	65
4.3.1	Identifying Recoils	65
4.3.2	β And Position Corrections	65
4.3.3	SeGA Timing Gates	68
4.4	Simulation Software	69
4.5	Histogram Manipulation With ROOT	73
4.5.1	Background Approximations	73
4.5.2	The Lifetime Suite	74
4.6	Determination Of Degraded Excitation Contributions	76
4.7	Absolute Foil Distance Determination	78
4.8	Origin Of Systematic Errors	81
5	Results	83
5.1	Gamma Spectroscopy Results	83
5.1.1	^{62}Zn	84
5.1.2	^{70}Br	86
5.1.3	^{68}Se	88
5.1.4	^{72}Kr	91
5.1.5	^{70}Se	92
5.1.6	^{66}Ge	94
5.1.7	^{69}Se	97

5.1.8	^{65}Ga	102
5.2	Lifetime Results	104
5.2.1	^{62}Zn	104
5.2.2	^{70}Br	107
5.2.3	^{68}Se	110
5.2.4	^{72}Kr	113
5.2.5	^{70}Se	114
5.2.6	^{66}Ge	118
5.2.7	^{69}Se	122
5.2.8	^{65}Ga	125
5.2.9	Summary Of Lifetime Results	127
6	Discussion	129
6.1	Collectivity In $N = Z$, $A \sim 70$ Nuclei	129
6.2	Collectivity In $A = 70$ Isobaric Nuclei	133
6.3	Further ^{70}Br Discussion	136
6.3.1	B(M1) Measurement: The Quasideuteron Picture	136
6.3.2	Theoretical Spectroscopic Factors For ^{70}Br	138
6.4	^{69}Se : Comparison To Shell Model Calculations	141
6.5	Evidence Of Radiative Electron Capture	143
7	Summary And Future Work	148
7.1	Summary	148
7.2	Future Work	150
A	The Lifetime Suite: An Example Code	152
	Bibliography	158

List of Figures

1.1	Nilsson plot for the N,Z = 35 region	14
1.2	Previously published B(E2;2 ₁ ⁺ →0 _{gs} ⁺) systematics in A = 70 region	15
1.3	Coulomb energy differences in the <i>sd</i> -, <i>f_{7/2}</i> - and <i>fp_g</i> -shell regions	17
2.1	The splitting of <i>j</i> orbitals in deformed nuclei	21
2.2	Schematic describing isospin in the two-nucleon system	25
2.3	Bentley's Isospin Triangle	26
3.1	Schematic of the NSCL beamline	33
3.2	Photograph of the S800 spectrograph	37
3.3	Photograph of the SeGA array	41
3.4	Schematic of the SeGA segment labelling scheme	42
3.5	Schematic of the RDDS technique	47
3.6	Photograph of the TRIPLEX plunger	52
3.7	Plunger electronics diagram	53
3.8	Schematic of the PZT plunger motor	55
3.9	Foil distance fluctuation measurement	55
4.1	Flow chart of analysis programs	57
4.2	CRDC angle and x position correction spectra	60
4.3	Object scintillator correction spectrum	61
4.4	CRDC pad calibration spectrum	62
4.5	CRDC mask calibration spectrum	62
4.6	Relative γ -ray efficiency spectrum	65
4.7	Time-of-flight separation of secondary beam components	66
4.8	S800 particle identification plot	66
4.9	Comparison of γ spectra with and without Doppler correction	67
4.10	SeGA timing spectrum	68

4.11	Comparison of experimental and simulated particle spectra	69
4.12	a_{ta} experimental particle distributions	71
4.13	β distribution of ^{70}Se recoils	72
4.14	Altering the simulated recoil distribution width parameter	73
4.15	Experimental and simulated γ spectra with background addition . . .	74
4.16	χ^2 fit example	75
4.17	Degrader excitation contribution for ^{70}Se	76
4.18	^{70}Br degrader excitation contribution from fit to 2D χ^2 surface	77
4.19	Photograph showing foil distortion	80
4.20	Plunger foil capacitance measurement	81
5.1	Target-only γ spectrum of ^{62}Zn	84
5.2	Partial level scheme of ^{62}Zn	85
5.3	Target-only γ spectrum of ^{70}Br	86
5.4	Identifying the 321 keV transition in ^{70}Br	87
5.5	Target-only γ spectrum of ^{68}Se	88
5.6	Partial level scheme of ^{68}Se	89
5.7	The previously unobserved 752 keV transition in ^{68}Se	90
5.8	Target-only γ spectrum of ^{72}Kr	92
5.9	Target-only γ spectrum of ^{70}Se	93
5.10	Partial level scheme of ^{70}Se	93
5.11	Target-only γ spectrum of ^{66}Ge	95
5.12	Partial level scheme of ^{66}Ge	96
5.13	Target-only γ spectrum of ^{69}Se	97
5.14	Partial level scheme of ^{69}Se	98
5.15	γ coincidence measurements in ^{69}Se	100
5.16	Presence of ^{27}Al peak in lab frame target-only γ spectrum of ^{69}Se . .	101
5.17	Target-only γ spectrum of ^{65}Ga	103
5.18	Partial level scheme of ^{65}Ga	103
5.19	Lifetime fit of 4_1^+ state in ^{62}Zn	105
5.20	Lifetime fit of 2_1^+ state in ^{62}Zn	107
5.21	Lifetime fit of 5_1^+ state in ^{70}Br	108
5.22	The long-lived nature of the 3_1^+ state in ^{70}Br	109
5.23	Lifetime fit of 3_1^+ state in ^{70}Br	110
5.24	Lifetime fit of 2_1^+ state in ^{70}Br	111
5.25	Lifetime fit of 2_1^+ state in ^{68}Se	113

5.26	Lifetime fit of 2_1^+ state in ^{72}Kr	114
5.27	Lifetime fit of 4_1^+ state in ^{70}Se	115
5.28	Lifetime fit of 2_2^+ state in ^{70}Se	116
5.29	Lifetime fit of $3_1^{(-)}$ state in ^{70}Se	116
5.30	Lifetime fit of 2_1^+ state in ^{70}Se	118
5.31	Lifetime fit of 7_1^- state in ^{66}Ge	119
5.32	Lifetime fit of 4_1^+ state in ^{66}Ge	120
5.33	Lifetime fit of 2_2^+ state in ^{66}Ge	121
5.34	Lifetime fit of 2_1^+ state in ^{66}Ge	121
5.35	Lifetime fits in ^{69}Se	124
5.36	Lifetime fit of $\frac{3}{2}_1^-$ state in ^{69}Se (90 keV γ ray)	125
5.37	Lifetime fits in ^{65}Ga	126
6.1	Collectivity systematics of $N = Z$ nuclei in the $A \sim 70$ region	130
6.2	Shell model monopole matrix elements for the <i>fp shell</i>	132
6.3	Shell model single-particle energies for the $A = 40\text{-}80$ region	132
6.4	Shell model occupation numbers for $N = Z$, $A \sim 70$ nuclei	133
6.5	Momentum distribution of ^{70}Br recoils	138
6.6	Theoretical/experimental level schemes of ^{69}Se	144
6.7	Radiative electron capture distributions in the secondary beam plot .	146
6.8	Radiative electron capture distribution in a recoil plot	146
6.9	γ spectrum after gating on radiative electron capture distribution . .	147

List of Tables

4.1	S800 magnet settings	59
4.2	Degrader excitation contributions	78
4.3	Data run lengths	78
4.4	^{62}Zn 2_1^+ lifetime using different plunger foil zero-offset distances	80
5.1	Transitions identified in ^{62}Zn	85
5.2	Transitions identified in ^{70}Br	88
5.3	Transitions identified in ^{68}Se	90
5.4	Transitions identified in ^{72}Kr	92
5.5	Transitions identified in ^{70}Se	94
5.6	Transitions identified in ^{66}Ge	95
5.7	Transitions identified in ^{69}Se	99
5.8	Transitions identified in ^{65}Ga	102
5.9	Effective lifetimes of feeding states to the 2_1^+ state in ^{70}Se	117
5.10	Summary of all lifetime results	128
6.1	Experimental/theoretical $B(E2; 2_1^+ \rightarrow 0_{gs}^+)$ results for ^{70}Br and ^{70}Se	134
6.2	Experimental/theoretical $B(\sigma L\downarrow)$ results for ^{70}Br $3_1^+ \rightarrow 2_1^+$ and $5_1^+ \rightarrow 3_1^+$ transitions	136
6.3	Calculated orbital occupancies for ^{71}Br ground state	139
6.4	Theoretical spectroscopic factors for neutron knockout to ^{70}Br	140
6.5	Theoretical spectroscopic factors for neutron knockout to ^{69}Se	142

Acknowledgements

I would like to thank all who have supported me during my undergraduate and postgraduate studies at York. Firstly, I would like to thank my supervisor Prof. Bob Wadsworth for guiding me through my Ph.D. and for making sure I saw the world whilst studying. I would like to thank the other members of the Nuclear Physics Group at York for their tireless assistance. Thanks to coding wizard Dr. Paul Davies for making a mildly competent coder out of me, and thanks also to Prof. Mike Bentley, Prof. David Jenkins and every other academic for their words of advice on the nitty-gritty physics stuff. Thanks also to my overseas collaborators such as Prof. Hiro Iwasaki at NSCL, Dr. Antoine Lemasson at GANIL and Prof. Alfred Dewald at Universität zu Köln.

Special thanks go to the colleagues and friends I have made over the years at York. There are far too many people to name, and I am worried I may miss someone, so I won't even try. You know who you are.

People outside physics deserve a big thank you, too. Thanks to Bex for sticking by me through all the ups and downs of a research degree. A large thank you must be given to the kind ladies at the Roger Kirk Centre canteen, whose chicken and bacon sandwiches fuelled four years of research. Thanks also to my family for supporting me no matter where I decided life was taking me. I would like to dedicate this thesis to them.

Declaration

I declare that the work presented in this thesis, except where otherwise stated, is based on my own research and has not been submitted previously for a degree at this or any other university.

Signed,



Adam Jacob Nichols.

Publications

J. Henderson *et al.* Spectroscopy on the proton dripline: First observation of excited states in ^{74}Sr . *Submitted to Phys. Rev. Lett.*

C. Morse *et al.* Lifetime measurements of the yrast 8^+ and 9^+ states in ^{70}As . *Submitted to Phys. Rev. C.*

A. J. Nichols *et al.* *Phys. Lett. B* **733**, 52-57, (2014).

G. Ghazi Moradi *et al.* *Phys. Rev. C* **89**, 041310 (2014).

G. Ghazi Moradi *et al.* *Phys. Rev. C* **89**, 041301 (2014).

J. Henderson *et al.* *JINST* **8**, P04025 (2013).

P. Ruotsalainen *et al.* *Phys. Rev. C* **88**, 041308(R) (2013).

A. Lemasson *et al.* *Phys. Rev. C* **85**, 041303(R), (2012).

Chapter 1

Introduction

The advent of radioactive ion beams has opened up a new chapter in experimental physics. Radioactive beam facilities, such as the National Superconducting Cyclotron Laboratory (NSCL) at Michigan State University, allow physicists to access regions of the nuclide chart at the driplines and extremes of isospin. Their inception allows access to some nuclei for the first time, meaning that information on binding energies, excited state structures and decay half-lives can be discerned for isotopes that until recently were completely inaccessible. The use of fast radioactive ion beams allows experimenters to access exotic nuclei near the proton dripline via reaction processes such as nucleon knockout or Coulomb excitation. Progress in radioactive heavy-ion beam technology has therefore made nuclear physics research a fast-evolving field.

Nucleon knockout reactions are particularly interesting mechanisms for studying excited state structures in exotic isotopes. Unlike fusion-evaporation reactions - which tend to populate states of high angular momentum and energy near the continuum that then decay down the yrast line to the ground state - direct nuclear reactions, such as nucleon knockout, populate low-lying excited states. Information on the low-lying structure of exotic nuclei, such as the single-particle orbitals occupied by the knocked-out nucleon, can be extracted from these and other reactions, providing a useful test of shell model interactions in the region studied. More information on the reaction mechanisms discussed in this work can be found in Section 2.3.

Interest in medium-mass self-conjugate nuclei has increased with the advent of fast radioactive beams. In $N = Z$ nuclei, neutron and proton shell effects can act coher-

ently due to both nucleons occupying the same orbitals. This in turn promotes a greater sensitivity of nuclear properties, such as deformation-driving effects resulting from proton-neutron correlations [1], to small changes in nucleon number. Due to the increased binding energy experienced by nuclei with similar numbers of protons and neutrons, the line of stability tends to follow the $N = Z$ line for low-mass nuclei. Nuclear matter prefers to be symmetric in protons and neutrons because, at a constant A , this arrangement maximises the availability of the lowest quantum single-particle states. However, at higher mass the line of stability veers towards the neutron-rich side of the $N = Z$ line due to the Coulomb repulsion of the protons. The $N = Z$ line therefore begins to separate from the line of stability just after ^{40}Ca and approaches the proton dripline, beyond which nuclei become proton unbound. The $N = Z$ line continues to approach the proton dripline for some way up the nuclide chart, with the heaviest experimentally observed proton-bound $N = Z$ nucleus being ^{100}Sn .

Collective excitations are interesting because they give an indication of the level at which the individual nucleons are acting together. Away from spherical shell closures deformed shapes are common in the ground states of nuclei, meaning collective effects are seen more commonly in mid-shell regions. Different sub-shell gaps open up at different levels of deformation (see Fig. 1.1), making such deformed shapes energetically favourable. The $A \sim 70$, $N = Z$ region of the nuclide chart, where valence nucleons may occupy the fp shell, is of interest due to the deformation-driving effects of the $g_{\frac{9}{2}}$ intruder orbital [2, 3]. The steepness of the $g_{\frac{9}{2}}$ level projections in the Nilsson plot (see Fig. 1.1) allows for rapid intrusion of the $g_{\frac{9}{2}}$ orbital into lower energies, giving more stability to deformed shapes. The $g_{\frac{9}{2}}$ orbital therefore has a role in increasing collectivity as the mid-shell point, located between the nucleon numbers of 28 and 50, is approached. This mid-shell region is of added interest because it is also the location where nuclear shapes vary rapidly with both nucleon number and angular momentum (e.g., see [4]). These effects arise due to the presence of large sub-shell gaps at nucleon numbers of 34 and 36 (oblate), 34 and 38 (prolate) and 40 (spherical) [3, 5] (see Fig. 1.1). In addition, nuclei in this region have competing, low-lying configurations resulting from more than one shape, which results in the rapid shape changes with angular momentum. These features make this region very challenging from a theoretical perspective.

One of the goals of nuclear structure physics is the complete mapping of deformation

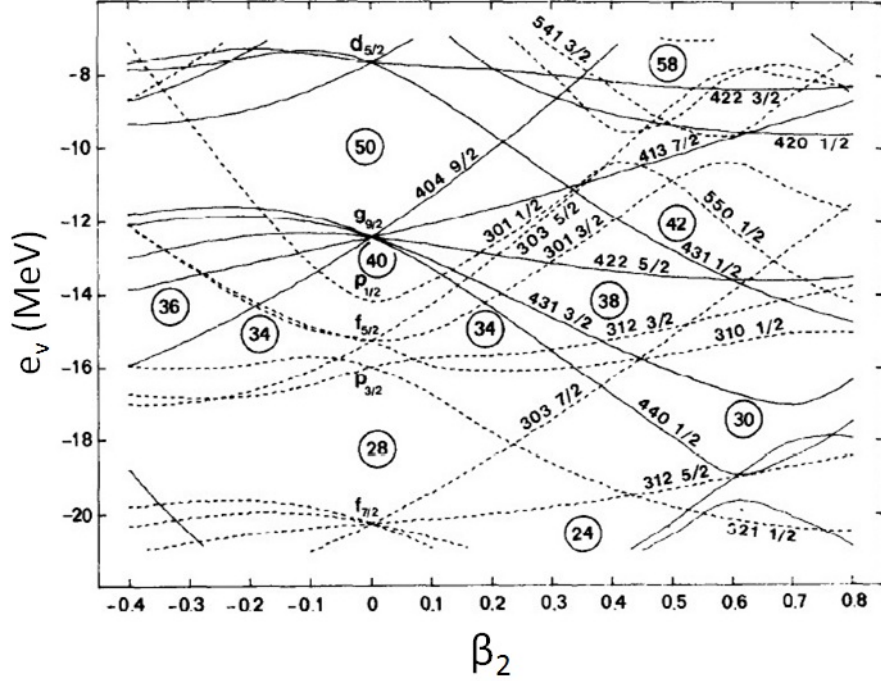


Figure 1.1: Nilsson diagram of single-particle energy levels as a function of deformation parameter β_2 in the $N, Z = 35$ region. Sub-shell gaps at both oblate ($\beta_2 < 0$) and prolate ($\beta_2 > 0$) deformations lead to drastic changes in nuclear shape with the addition or subtraction of only a few nucleons. Taken from Ref. [3].

and collectivity changes along the $N = Z$ line. Of particular interest is the region of the fp shell and beyond ($56 < A < 100$), where the evolution of collectivity is expected to be complicated, especially around the mid-shell region. Reduced transition strengths can yield information on quadrupole collectivity and nuclear deformation as well as providing a sensitive test of nuclear models. Reduced transition strengths can be inferred for transitions from excited states in nuclei by measuring the lifetime of the state (see Section 2.4 for more details). Of particular interest when studying collectivity is a measurement of the $B(E2)$ reduced transition strength. More information on electromagnetic transition theory can be found in Section 2.4. $B(E2)$ values between the first excited 2^+ state and the ground state have been measured previously for several even-even $N = Z$ nuclei in the $A = 70$ region: ^{64}Ge [6], ^{68}Se [7], ^{72}Kr [8,9] and ^{76}Sr [10]. These results suggest a rapid increase in $B(E2)$ values, and hence deformation, between ^{68}Se ($B(E2\downarrow) = 432(58) \text{ e}^2\text{fm}^4$) [7] and ^{72}Kr ($B(E2\downarrow) = 919(98) \text{ e}^2\text{fm}^4$) [8,9] (see Fig. 1.2). Before this work, no transition strength data for any of the odd-odd $N = Z$ nuclei in this region were available, preventing comparison with calculations that include such nuclei (e.g., [2,11]). A measurement of the

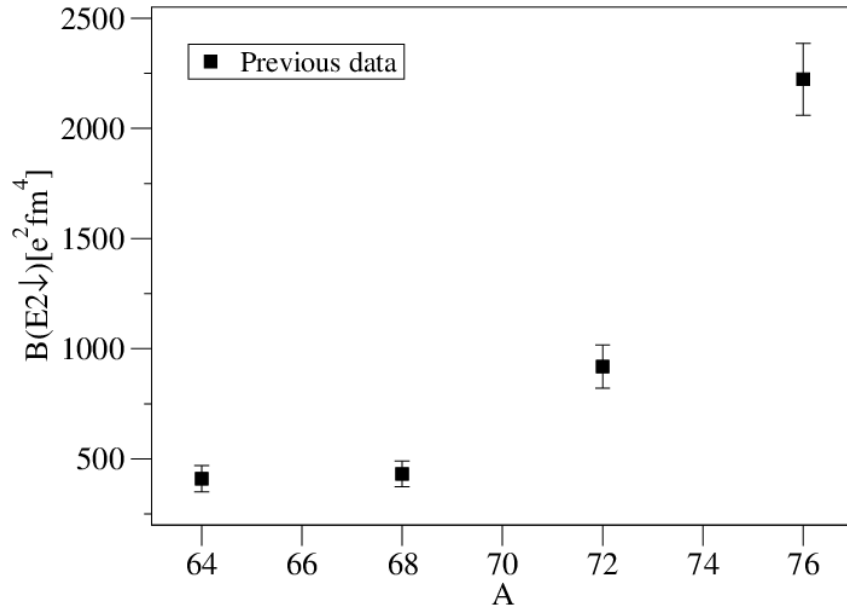


Figure 1.2: $B(E2; 2_1^+ \rightarrow 0_{gs}^+)$ values for $N = Z$ nuclei in the $A = 70$ region from previous experimental work [6–10]. The jump in collectivity begins between $A = 68$ (^{68}Se) and $A = 72$ (^{72}Kr), however without information on the odd-odd $N = Z$ nucleus ^{70}Br it is not possible to say how abrupt this jump is or where exactly it begins.

$B(E2; 2_1^+ \rightarrow 0_{gs}^+)$ value for ^{70}Br is essential for beginning to complete the picture of collectivity in this mid-shell region, and identifying where the low-spin collectivity jump occurs.

Studying low-lying excited states in $N = Z$ nuclei is interesting as it can give an indication of the relative strengths of the isospin $\mathbf{T} = 0$ (isoscalar) and $\mathbf{T} = 1$ (isovector) np interactions (see Section 2.2 for details on isospin). In some $N = Z$ nuclei the $\mathbf{T} = 0$ states tend to be pushed down in energy to form the ground states, with a distinct pairing gap existing between these and higher-lying $\mathbf{T} = 1$ states. However, in medium-mass odd-odd $N = Z$ nuclei there is an effect of isospin inversion, where the ground state is the $\mathbf{T} = 1$ 0^+ state. Studying the excitation energy of the $\mathbf{T} = 0$ 1^+ state in these nuclei is therefore essential in understanding the relative strengths of the two types on np interaction. This highlights another interest in studying the low-lying excitation structure of odd-odd ^{70}Br . ^{70}Br has a $\mathbf{T} = 1$ 0^+ ground state, and is the first odd-odd *fp**g*-shell nucleus beyond ^{58}Cu where the $\mathbf{T} = 0$ 1_1^+ state has not been observed. There have been detailed studies of the low-lying excited states in ^{70}Br using fusion-evaporation reactions [12, 13] but these failed to locate the state. The identification of the $\mathbf{T} = 0$ 1_1^+ excited state

is of importance for testing various nuclear models, such as large-scale shell model calculations [2], that predict the state to lie just below the $\mathbf{T} = 1$ 2_1^+ state in energy. The energy difference between the $\mathbf{T} = 0$ 1_1^+ state and the $\mathbf{T} = 1$ 0^+ ground state would provide key information on the relative strengths of the isoscalar and isovector np interactions.

A further interest in the $A \sim 70$, $N \sim Z$ nuclei results from indications [14, 15] that small energy shifts of single-proton levels can yield different shape-driving effects, potentially resulting in different shapes in nuclei across an isobaric multiplet, which in turn would result in a significant breakdown of isospin symmetry. It has been suggested that this may be the origin of the observed negative Coulomb energy difference between ^{70}Se and ^{70}Br [14] (see Fig. 1.3 and text below). It is of interest therefore to compare transition strengths from decays of isobaric analogue states in these two nuclei, i.e., states with the same spin-parity and isospin quantum number.

Coulomb energy differences (CEDs) are calculated by setting the ground state energies of two isobaric nuclei to zero, and then measuring the difference in energies of analogue excited states of the same isospin. This measurement is usually performed between $\mathbf{T} = 1$ excited states in odd-odd $N = Z$ nuclei and their even-even isobaric ($T_z = +1$) neighbours. In some cases, the proton-rich isobaric ($T_z = -1$) nucleus has a known level scheme and so mirror energy differences (MEDs) between the $N = Z \pm 2$ nuclei either side of the $N = Z$ line can be extracted. These give useful information on the charge-symmetric nature of the nuclear force [16]. One can also calculate triplet energy differences (TEDs) between excited states in the $N = Z$ nucleus and its $N = Z \pm 2$ isobars, which give information on the charge-independent nature of the nuclear force [16]. The excitation energy of the 2_1^+ state in the $A = 70$, $N = Z - 2$ isobaric nucleus ^{70}Kr is not experimentally known and so MED and TED studies cannot currently be performed for the $A = 70$ isobaric triplet. However, it is possible to measure CEDs between ($N = Z$) ^{70}Br and ($N = Z + 2$) ^{70}Se .

Lifetime studies in the $N = Z$, $A \sim 70$ region are of interest from an astrophysical perspective. Both ^{68}Se and ^{72}Kr , which are studied in this work, are potential waiting-point nuclei in the rp-process [18, 19], which is a process of rapid proton capture believed to occur on accreting neutron stars in binary star systems. Knowledge of the low-lying excited state structures of these nuclei, and nuclei in their vicinity on the nuclide chart, is of importance in refining models of this important

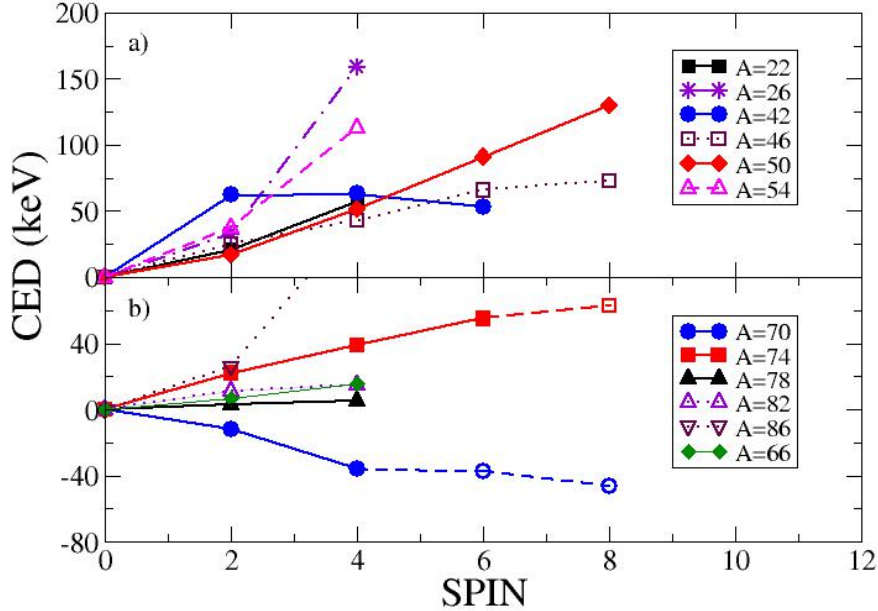


Figure 1.3: Coulomb energy differences for isobaric pairs of nuclei in the *sd*-shell/ $f_{7/2}$ -shell (a) and *fpq*-shell (b) regions. The $A = 70$ CED shows a negative trend unlike the others, which may be due to the presence of different ground state shapes in the $A = 70$ pair. Plot taken from Ref. [17].

astrophysical process.

Thesis Overview

An outline of the theoretical models of direct relevance to this work is given in Chapter 2, along with specifics of reaction mechanisms, isospin formalism and electromagnetic transition theory. Details of the set-up of the thesis experiment performed at NSCL in November/December 2011 is the subject of Chapter 3. In Chapter 4, details of the data analysis programs are given along with discussions on calibrations, corrections and software gating. The simulation program used to extract final lifetime results from the experimental γ spectra is also discussed in Chapter 4. The results obtained in the present work are presented in Chapter 5, followed by a discussion of the results in Chapter 6. Chapter 7 summarises the presented work,

draws conclusions from the analysis and discusses the potential for future work in the region.

Chapter 2

Theoretical Considerations

2.1 Nuclear Models

Understanding the behaviour of nucleons in a nucleus is not an altogether simple task. The mathematical firepower necessary to solve the many-body problems in heavy nuclei is particularly taxing unless one chooses a simple, mathematically tractable theory to describe the nucleus, and develop from that a nuclear model. There are many nuclear models in existence that describe a range of nuclear properties, with no single theory that can accurately explain all of nuclear physics. That is the price of oversimplification, which can bring with it rich insight into the behaviour of nucleons and nuclei. A good theory needs to describe previously measured nuclear properties to a satisfactory level and also predict with some accuracy new properties that can be confirmed by future experiments.

2.1.1 The Shell Model

One of the earliest models used in nuclear physics was the liquid drop model (LDM), which describes the nucleus as being like a liquid drop, a bulk object with a low compressibility and a well-defined surface. Obviously this treatment is a large oversimplification. For a start, we know that the nucleus is not a single entity but is made of many interacting nucleons. The surface is also diffuse, not well defined as

is the case for a liquid drop. The LDM also fails to explain the existence of the so-called ‘magic numbers’ (at nucleon numbers 2, 8, 20, 28, 50, 82 and 126 for spherical nuclei) where nuclei are more tightly bound.

The solution to some of these issues came in the form of the spherical nuclear shell model. Atomic shell models enjoy great success with regards to explaining the behaviour of electrons in the atom, and so nuclear physicists attempted to apply these concepts to explain nuclear structure. There are obvious differences between the two approaches. For example, in atoms, the electrons are orbiting in a Coulomb field provided by the nucleus, i.e., an external agent, whereas nucleons are orbiting in a nuclear potential they themselves create. The shell model, when applied to the nuclear environment, has enjoyed high levels of success nevertheless. Just like its atomic variant, the nuclear shell model treats the nucleons as occupying various single-particle orbitals whose occupations are restricted by the Pauli exclusion principle. These single-particle orbitals are successively filled as nucleons are added to the nucleus. Magic numbers are explained as the location of shell closures, which result in more stable nuclei. With the shell model, one can describe the nucleus as an inert core (the nearest closed shell to the Fermi surface) with the nuclear characteristics dictated by interactions and excitations of just the valence nucleons. The area of interest in this work is the *fp*g model space, as it is here that valence nucleons may interact for nuclei in the $N = Z$, $A = 70$ region. It is believed that the occupancy of the $g_{7/2}$ orbital drives the rapid increase in collectivity in the mid-*fp*g shell region (see Fig. 1.2).

Whilst the assumption of sphericity is valid at or close to spherical closed shells, most nuclei far from shell closures exhibit some form of deformation. Nuclei can exhibit a range of shapes, the majority of them being prolate (rugby-ball shaped) [20] but some exhibiting oblate (Smartie shaped) or even triaxial deformations. Higher-order deformations are also possible, such as octupole (pear shaped) deformations, but these are beyond the scope of this discussion.

The deformed nuclear shell model can be used with nuclei far from closed shells. This approach, which can employ a number of different deformed potentials, is useful for explaining some single-particle excitations that cannot be understood using a spherical shell model. When nuclei undergo deformation, the angular momentum of an orbital, j , is no longer a good quantum number. Deformation causes an orbital

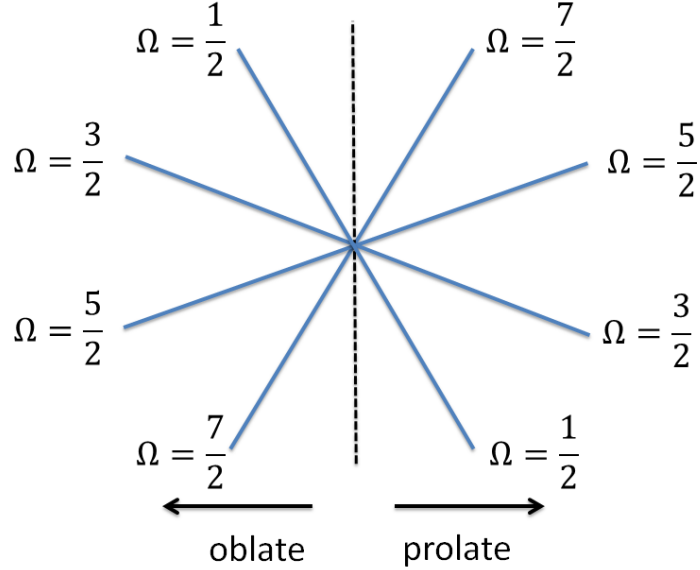


Figure 2.1: Schematic illustration of the splitting of j orbitals during deformation into projections onto the symmetry axis, Ω . The example shows the splitting of a $j = \frac{7}{2}$ orbital.

with angular momentum j to split into its possible projections, Ω , which are defined as projections onto the nuclear symmetry axis (see Fig. 2.1).

When an appropriate deformed shell model potential is chosen, such as the deformed Woods-Saxon or anisotropic harmonic oscillator potential, it is possible to calculate orbital energies as a function of nuclear deformation. One such example is the Nilsson diagram, which uses a deformed 3D simple harmonic oscillator potential. An example Nilsson diagram for protons and neutrons in the vicinity of $N, Z = 35$ is shown in Fig. 1.1. In this figure, positive β_2 corresponds to prolate deformation and negative β_2 corresponds to oblate deformation.

Some interesting points can be made when looking at the Nilsson diagram in Fig. 1.1. The deformation, which causes low- Ω orbitals to be pushed down in energy for prolate nuclei and up for oblate nuclei, allows the intrusion of higher-shell orbitals into lower shells. An example of these so-called ‘intruder’ states is the $g_{7/2}$ orbital, which intrudes into the fp shell and is believed to drive collectivity in the $N, Z = 35$ region. Deformation causes the shell gaps at spherical magic numbers to disappear with new, smaller sub-shell gaps opening up at different deformation values. This leads to added stability for some deformed nuclei. For example, at both prolate

and oblate shapes there is a deformed sub-shell gap at $N = Z = 34$. Thus both prolate and oblate shapes exhibit a larger level of stability here, and this can lead to competition between the two shape minima. This so-called ‘shape coexistence’ is a feature of nuclei in the $A = 70$, $N = Z$ region. The structure of the Nilsson orbitals leads to quite complicated shape evolution in the $A = 70$, $N = Z$ region despite changes of only a few nucleons.

2.1.2 Models Used In This Work

In this work experimental results are compared to theoretical predictions from a number of different models. These models will be described briefly below.

Large-scale Shell Model

Many theoretical predictions in this work (see Chapter 6) come from large-scale shell model calculations performed by Kaneko *et al.* [21–24]. These employ the filter-diagonalisation method based on the recently proposed Sakurai-Sagiura method [25, 26]. Current shell model calculations with the m-scheme using the Lanczos diagonalisation method [27] struggle to obtain solutions for $T \sim 1$ states in odd-odd self-conjugate nuclei when including the Coulomb interaction [22], whilst the filter-diagonalisation method is able to overcome this problem [26].

Model spaces are essential for shell model calculations as there is not sufficient computing power to perform calculations with the entire shell model space involved. The model space is chosen based on the expected valence space of the excitations or reactions taking place. In the case of this work the fpg shell was chosen as the model space, with the nucleons below this shell assumed to form an inert core that does not contribute to excitations. In reality, however, ignoring a large amount of the shell model orbitals means that essential physics is missed out, as more often than not the supposedly inert core does contribute. In order to ‘re-add’ the physics that is left out when a restricted model space is chosen, an effective interaction is used. The shell model results quoted in this work were calculated using two different sets of effective interactions and model spaces. One effective interaction was the modern JUN45 interaction [28]. This interaction was used in the $f_{\frac{7}{2}}pg_{\frac{7}{2}}$ model space. Another

effective interaction, the GXPF1A interaction [29], was used within the full fp model space.

Excited VAMPIR Model

The Excited VAMPIR model is a beyond-mean-field theory that utilises symmetry projection before variation [30]. Its use in the region of $A = 70$ nuclei has been discussed extensively in the literature, e.g., [15, 31–33]. The Excited VAMPIR approach is particularly useful as it allows for a relatively large model space. It also allows for different levels of shape mixing components in isobaric nuclei and so, unlike the shell model approaches already mentioned, it can predict different ground state shapes for nuclei of the same isobar. The Excited VAMPIR approach takes into account the possibility of polarisation of the valence particles by the Coulomb interaction, which can act to ‘tip’ competing shape minima in different directions for two isobaric nuclei.

The central limit of this model is the sheer number of different configurations necessary to correctly replicate even the simplest nuclei. For more complicated nuclei, the calculations with all significant configurations included are too computationally expensive and take a large amount of time to complete. This means that simplifications have to be made with not all configurations included.

Finite-range Droplet Macroscopic Model / Folded Yukawa Single-particle Microscopic Model

The finite-range droplet macroscopic model and folded Yukawa single-particle microscopic model [11] is a macroscopic-microscopic global nuclear calculation. The calculations are based on the finite-range droplet model [34, 35] for the macroscopic energy, with the folded Yukawa single-particle potential [36, 37] being used for microscopic corrections. It has been used to predict the ground state masses and deformations of a wide range of nuclei across the nuclide chart. The model includes pairing and shell corrections. Reduced transition strengths derived from these calculations have been compared to experimental equivalents in this work (see Sections 6.1 and 6.2).

The central limit of this model is that it employs a global approach to describing nuclear properties and is adjusted to the ground state masses and properties of nuclei already measured. It is not always completely successful at predicting characteristics of very exotic nuclei.

2.2 Isospin Formalism

Investigations of the nuclear force have come across two central observations. The force between two nucleons is largely charge symmetric (the strong force between two protons is the same as between two neutrons) and charge independent (the strong force between two like nucleons is the same as between a proton and a neutron). Whilst these two assumptions are simplifications, it nevertheless allows one to develop a formalism describing the symmetry. This idea was developed by Wigner and Heisenberg [38], and has been more recently discussed in detailed reviews by Warner [39] and by Bentley and Lenzi [16]. Isospin formalism revolves around the concept of an isospin quantum number (*isospin* coming from ‘*isotopic spin*’). This standpoint allows one to treat the neutron and proton as manifestations of the same particle, the nucleon, with different isospin projections representing protons and neutrons. This is of course neglecting Coulomb effects, which affect protons and not neutrons. Both protons and neutrons, as nucleons, have an isospin \mathbf{T} of $\frac{1}{2}$. Disagreement on the sign convention of the isospin projections persists to this day, with nuclear physicists preferring to assign a projection of $-\frac{1}{2}$ for protons and $+\frac{1}{2}$ for neutrons. The total isospin projection of a nuclear state, therefore, is the algebraic sum of the individual nucleon projections.

$$T_z = \frac{N - Z}{2} \quad (2.1)$$

Similarly, the total isospin of the nuclear state \mathbf{T} is given by the vector addition of the isospins of the individual nucleons.

Isospin can be most easily explained by looking at the two-nucleon system as shown schematically in Fig. 2.2. The proton-proton (pp) and neutron-neutron (nn) systems have $T_z = -1$ and $T_z = +1$, respectively, with total isospin $\mathbf{T} = 1$. The Pauli

2.2. ISOSPIN FORMALISM

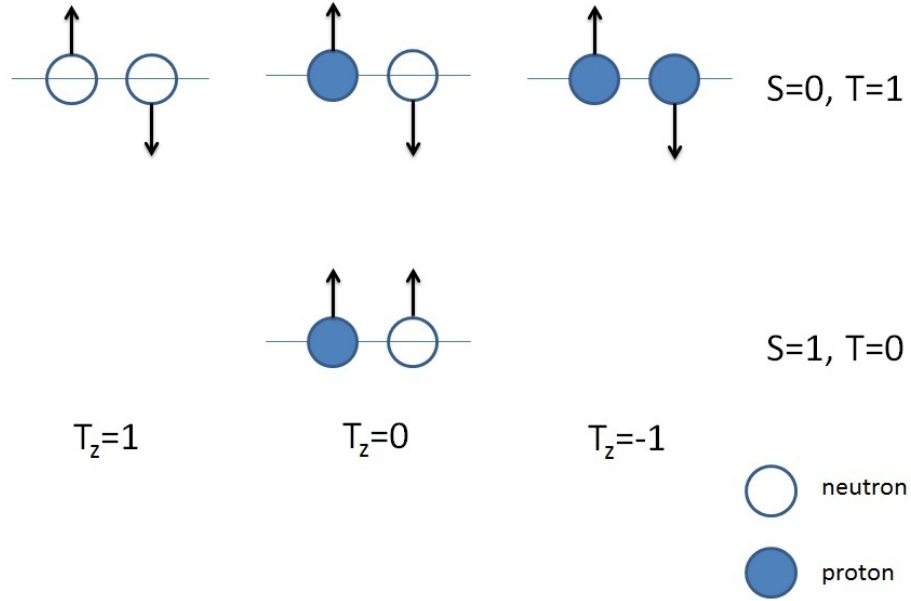


Figure 2.2: Schematic of the two-nucleon system in terms of isospin. The black arrows represent the intrinsic spin orientations of the nucleons.

exclusion principle dictates that, since these nucleons are fermions, they must couple with their intrinsic spins anti-parallel. Since the concept of isospin symmetry applies, and protons and neutrons are being treated as manifestations of the same particle, it follows that a similar configuration must exist in the neutron-proton (np) system ($\mathbf{T} = 1, T_z = 0$). Protons and neutrons, however, are not identical fermions and thus their coupling is not restricted by the Pauli exclusion principle. They can align anti-parallel (the isospin *triplet* case, since there is a triplet of states) or parallel (the isospin *singlet* case). The singlet state, with the proton and neutron aligned with their intrinsic spins parallel, has an isospin projection $T_z = 0$. The Pauli exclusion principle forbids similar configurations in the pp and nn cases therefore, since $T_z = 0$ is the only substate, it follows that \mathbf{T} must also be zero. The isospin singlet state, in the case of the two-nucleon system, sits at a lower energy than the $\mathbf{T} = 1$ triplet states, i.e., it is more bound.

Just as $\mathbf{T} = 0$ states can only exist in $N = Z$ nuclei, it follows that $\mathbf{T} = 1$ states can only exist in $N = Z$ and $N = Z \pm 2$ nuclei. There exists, at a higher energy, $\mathbf{T} = 2$ states that can exist in $N = Z, N = Z \pm 2$ and $N = Z \pm 4$ nuclei, but not in $N = Z \pm 6$ nuclei. Similar restrictions exist for odd-mass nuclei. An illustration of the allowed isospin states for nuclei is given by a schematic developed by M. A. Bentley (known as Bentley's Isospin Triangle) shown in Fig. 2.3. It is worth noting an important

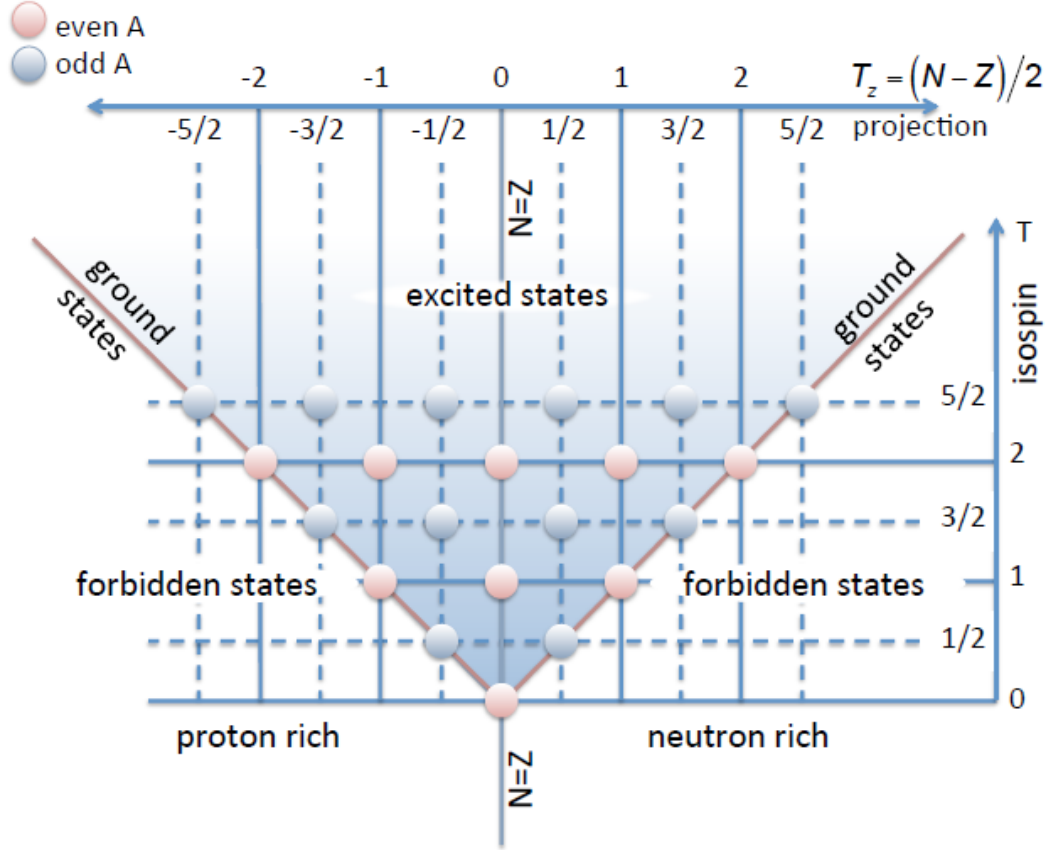


Figure 2.3: Bentley's Isospin Triangle, identifying the isospin-allowed and isospin-disallowed couplings of protons and neutrons. Image courtesy of M. A. Bentley.

limitation of this figure; this representation does not describe odd-odd $N = Z$ nuclei in the fpg shell, which have $\mathbf{T} = 1 0^+$ ground states and not $\mathbf{T} = 0 1^+$ ground states as the figure would suggest (see below).

Arranging proton-neutron pairs into the isospin singlet ($\mathbf{T} = 0, T_z = 0$) configuration is found on the whole to increase the binding energy of the system. For the case of the deuteron, for example, one finds that the ground state is a $\mathbf{T} = 0 1^+$ state, with the proton and neutron intrinsic spins aligned. The di-proton and di-neutron systems are energetically unbound, therefore isospin symmetry arguments suggest that the $\mathbf{T} = 1, T_z = 0, J^\pi = 0^+$ state in the deuteron is also unbound, which is experimentally the case. It therefore should follow that all $N = Z$ odd-odd nuclei show a preference for $\mathbf{T} = 0$ (*isoscalar*) couplings over $\mathbf{T} = 1$ (*isovector*) couplings, and thus the ground states of all $N = Z$ odd-odd nuclei should be $\mathbf{T} = 0$ states. However, in the mid- fpg shell region, $N = Z$ odd-odd nuclei have $\mathbf{T} = 1 0^+$ ground states, with the $\mathbf{T} = 0$ states lying at higher energies. This phenomenon, discussed in depth by

Macchiavelli *et al.* [1], is attributed to an increased $\mathbf{T} = 1$ pairing energy between the valence protons and neutrons that outweighs the symmetry energy, which increases for $\mathbf{T} = 0$ pairings. The strengths of the $\mathbf{T} = 1$ and $\mathbf{T} = 0$ interactions are therefore different. It suggests that in the *fp*g shell there is a dominance of isovector neutron-proton pairings over isoscalar pairings. The strength of the $\mathbf{T} = 0$ interaction is not well known [40].

2.3 Reaction Mechanisms

2.3.1 Nucleon Knockout

Direct reactions differ from compound nuclear reactions in that there is no intermediate/compound state between the initial and final states. Nucleon knockout reactions, which are a specific type of direct reaction, typically occur at energies of around 100 MeV/u. This is a higher energy than reactions that sample the entire nucleus such as fusion-evaporation (~ 5 MeV/u). This is because nucleon knockout reactions require a smaller de Broglie wavelength, and hence higher energy, for the beam (around the size of a nucleon) whereas fusion-evaporation reactions require beams with de Broglie wavelengths similar in size to the whole nucleus. Since nucleon knockout reactions need such high energies, the radioactive ion beams need to be accelerated to significant fractions of the speed of light. The excited states populated in the final nucleus are restricted according to the available angular momenta of the knocked-out nucleons. Nucleon knockout reactions, therefore, tend to populate low-lying excited states in the final nucleus directly [41, 42].

Single-nucleon knockout reactions in this work are occasionally discussed in theoretical terms using the eikonal reaction theory [43] (see Subsection 6.3.1). This reaction theory, coupled with spectroscopic factors from shell model calculations (see previous section) was used in this work to obtain theoretical parallel momentum distributions, which are then compared to experimental equivalents to extract information on orbital occupations. The eikonal reaction theory calculates the radial extent of the wavefunctions of the target and projectile nuclei and then calculates the level of overlap between the initial and final states, thus enabling reaction cross-sections to be extracted. The wavefunction amplitude normalisation comes from the

shell model spectroscopic factors. The eikonal reaction theory applies the spectator core approximation, where the nuclear core is assumed not to be excited in the reaction.

2.3.2 Coulomb Excitation

Coulomb excitation (sometimes abbreviated as *Coulex*) is a form of excitation that does not involve the exchange of nucleons between target and projectile nuclei [44]. Coulex is an inelastic excitation process and can be performed in inverse kinematics in order to probe excited states in the projectile nucleus. The excitation occurs through the exchange of virtual photons between the target and projectile nuclei. Coulomb excitation naturally populates states connected to the ground state by strong electromagnetic matrix elements, such as E2 excitations. This method is therefore well suited to investigating collective quadrupole degrees of freedom in nuclei.

Low-energy Coulex, where the kinetic energies of interacting nuclei are safely below the Coulomb barrier, is a useful reaction process as it tends to be multi-step and can be used to measure the sign of the nuclear quadrupole moment [45], thus extracting the nuclear shape in a model-independent manner. Low-energy Coulex experiments typically run beams in the 1-3 MeV/u range. Relativistic Coulex, by contrast, is a largely one-step process [46, 47]. If one wants to consider reactions in relativistic Coulex that only probe the Coulomb force and not the strong nuclear force, nuclei with very small deflection angles (large impact parameters) are selected. If no such selection is made, or other efforts are not made to remove the contributions from inelastic nuclear scattering, then the excitation mechanism of the recoils will contain contributions from both Coulomb excitation and nuclear scattering. In this experiment some nuclei were excited via this combination of mechanisms.

2.4 Electromagnetic Transition Theory

Nuclear structure is often studied using the long-range electromagnetic interaction as opposed to the short-range nuclear force. γ radiation is emitted from an excited

nucleus when it decays from one excited state to another (or to the ground state). The initial and final states of the nucleus have different charge and current distributions, so when a γ decay occurs there is a change of these distributions, or a change in the multipole moments. The de-exciting transition can be thought of as the operation of a quantum mechanical multipole operator, which acts to change the nucleus from its initial state ψ_i to its final state ψ_f and at the same time create a photon with a certain energy and multipolarity. The multipole transition matrix elements, $m_{fi}(\sigma L)$, for an electric (E) or magnetic (M) transition of multipolarity L , are given by

$$m_{fi} = \int \psi_f^* \hat{m}(\sigma L) \psi_i d\tau \quad (2.2)$$

where $\hat{m}(\sigma L)$ is the multipole transition operator. We can now use this to obtain a transition probability, which is proportional to the square of the matrix element, $m_{fi}(\sigma L)$, according to Fermi's Golden Rule. The *reduced* transition strength is given by

$$B(\sigma L) = | m_{fi}(\sigma L) |^2 . \quad (2.3)$$

We can express the transition probability (essentially the probability of the γ decay from state i to state f occurring) in terms of these reduced transition strengths. These are useful as the reduced transition probability is inversely proportional to the lifetime of the initial state. The relationship therefore can be exploited to extract the reduced transition strengths from measurable values, i.e., the initial state lifetime τ and the energy of the de-exciting transition E_γ . Reduced transition strengths are given below for the four lowest multipolarity transitions:

$$B(E1 \downarrow) = \frac{1}{\tau \cdot 1.587 \cdot 10^{15} \cdot E_\gamma^3} \quad (2.4)$$

$$B(E2 \downarrow) = \frac{1}{\tau \cdot 1.223 \cdot 10^9 \cdot E_\gamma^5} \quad (2.5)$$

$$B(M1 \downarrow) = \frac{1}{\tau \cdot 1.779 \cdot 10^{13} \cdot E_\gamma^3} \quad (2.6)$$

$$B(M2 \downarrow) = \frac{1}{\tau \cdot 1.371 \cdot 10^7 \cdot E_\gamma^5} \quad (2.7)$$

where E_γ is in MeV, $B(EL)$ values are in units of $e^2\text{fm}^{2L}$ and $B(ML)$ values are in units of $\mu_N^2\text{fm}^{2L-2}$. The down arrows in the above equations indicate that the reduced transition strengths are for the decay from the higher-lying state to the lower state, not the excitation from the lower state to the higher one. In this work both $B(E2\downarrow)$ and $B(E2\uparrow)$ values will be quoted. It will be noted on a case-by-case basis in the text which value is being used. The values are related by the general term $B(E2\uparrow) = (2J + 1) \times B(E2\downarrow)$. For $J = 0 \rightarrow 2$ and $J = 2 \rightarrow 0$ transitions, $J = 2$, therefore $(2J + 1) = 5$.

2.5 Quasideuteron Configurations

This section builds on Sections 2.2 and 2.4 to discuss isovector ($\Delta\mathbf{T} = 1$) M1 transitions. Isovector transitions in odd-odd $N = Z$ nuclei have been explained in terms of quasideuteron configurations [48]. It is noted in Ref. [48] that, in the case of isovector M1 transitions in odd-odd $N = Z$ nuclei, such transitions are enhanced in some cases and are strongly hindered in others. This is explained in terms of coupling of an inert even-even $N = Z$ core to two valence nucleons, a proton and a neutron, which are assumed to occupy a single shell model orbital. These two valence nucleons can recouple to any value between 0 and $2j$, where j is given by the shell model orbital, and positive parity.

The free one-proton one-neutron system is the deuteron, which has a $T = 0$ 1^+ ground state and an unbound $T = 1$ 0^+ resonance. Both nucleons in this system occupy the $1s_{\frac{1}{2}}$ orbital, which is a $j = \ell + \frac{1}{2}$ orbital. In the core + two-particle

2.5. QUASIDEUTERON CONFIGURATIONS

single- j model, we generalise from this to denote wavefunctions as *quasideuteron* if the two valence nucleons occupy a $j = \ell + \frac{1}{2}$ orbital. When they are formed from $j = \ell - \frac{1}{2}$ orbitals they are generalised as non-quasideuteron. The enhanced and hindered isovector M1 transitions are therefore explained as constructive and destructive interference, respectively, of the spin and orbit terms of the valence proton and neutron in this single- j approximation.

Chapter 3

Experimental Details

The National Superconducting Cyclotron Laboratory (NSCL) at Michigan State University, USA, is one of the forerunning scientific establishments for the study of rare isotope beams through fragmentation reactions. Understanding the properties of rare, radioactive nuclei involves the coupling of many cutting-edge experimental devices and the use of novel techniques. This chapter discusses the various stages of the beamline that accelerate and deliver the secondary beams to the experimental station. Also, a description of the particle and γ -ray detectors used in this work is given, as well as a discussion of the methods, devices and techniques used.

3.1 Beam Production

3.1.1 The Ion Source

The ion source used in this work was the Superconducting Source for Ions (SuSI) [49,50]. The ion source uses electron cyclotron resonance [51] to accelerate electrons in a microwave field, using these to bombard a neutral element held as a gas in a magnetic trap. The primary beam in this work was ^{78}Kr , which already exists in gaseous form and does not have to be evaporated. The positive krypton ions created in SuSI were accelerated towards the cyclotron through a potential on the order of 10 kV.

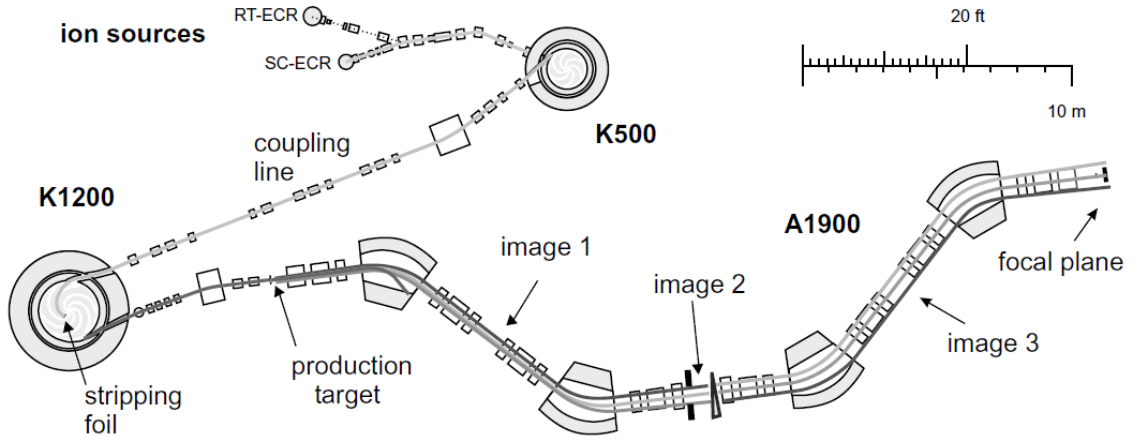


Figure 3.1: Schematic of the NSCL Coupled Cyclotron Facility and the A1900 fragment separator. Note the ion source labelled is not the current SuSI, but previous ion sources RT-ECR and SC-ECR [53]. Diagram taken from [54].

3.1.2 Primary Beam Acceleration

NSCL is capable of impressive feats of beam acceleration due to the design of its Coupled Cyclotron Facility (CCF) [52] (see Fig. 3.1). The facility combines two cyclotron devices in a coupled format: the K500 (the world’s first superconducting cyclotron) and the K1200. The names of the cyclotrons derive from their K number, the highest energy (in MeV) sustainable by a proton accelerated in the machine. Stripping an intense beam of low charge state after exiting the K500, followed by further acceleration in the K1200, provides experimenters with a higher ion current and beam energy than single-stage acceleration in a stand-alone cyclotron.

Positive ^{78}Kr ions that enter the cyclotrons from the ion source are accelerated in an electric field provided by three charged ‘dees’. Acceleration voltages are typically on the order of 140 kV. As the ions increase their velocity their radius of curvature increases. Magnetic fields help to confine the ion paths as they radiate outward. When the orbital radius becomes too large to remain inside the cyclotron, the particles are extracted.

The ions entering the K500 are partially stripped of their atomic electrons; it is only when the ions are injected from the K500 into the K1200 that full stripping takes place. At this stage the ^{78}Kr nuclei, now travelling at around $0.15c$, pass through a carbon stripper foil before entering the K1200. This foil acts to remove the remaining

atomic electrons so that the ^{78}Kr primary beam is in the 36+ charge state. When the ^{78}Kr primary beam leaves the K1200 cyclotron it has been accelerated to 150 MeV/u, corresponding to a velocity of $\sim 0.5c$.

3.1.3 The A1900: Secondary Beam Separation

In this work the primary ion beam (150 MeV/u ^{78}Kr at an intensity of 25 pA) bombarded a ^9Be production target shortly after the K1200 cyclotron. Radioactive secondary beams were created at this primary target via projectile fragmentation [55]. The secondary radioactive beams were then selected and steered through a carefully adapted series of magnets and apertures down to the experimental hall. Only the beam of interest (^{71}Br) and a set of isotones (^{70}Se , ^{69}As and ^{68}Ge) were transported to the experimental station.

A series of magnets and apertures designed for the purpose of beam selection and focusing is called a fragment separator; NSCL’s fragment separator is called the A1900 (see [54, 56] and Fig. 3.1). The number in the name is again a reflection of the K-value of the magnets. Since it has been shown that “over-matching” a projectile separator to its cyclotron by 60% allows the separation of neutron-rich nuclei at optimal production energies [52], a K-value of $1200 \times 1.6 \simeq 1900$ was chosen. It is designed to accept over 90% of a range of secondary beams created at the fragmentation target. It comprises a series of four 45° steering dipole magnets and twenty-four focusing quadrupole magnets, as well as sextupole and octupole magnets for the correction of higher-order aberrations. Each beam of mass number A in charge state Q travelling at a velocity v is deflected at the dipoles according to a property known as its magnetic rigidity, $B\rho$, given as

$$B\rho = \gamma \frac{A u}{Q e} v \quad (3.1)$$

where ρ is the radius of curvature of the magnet, γ is the relativistic γ factor, e is the electron charge and u is the mass in atomic mass units.

The large momentum acceptance of the A1900 (5.5%) means secondary beams of a similar charge-to-mass ratio will also make it through to the experimental hall,

3.1. BEAM PRODUCTION

since they have a similar $B\rho$. In order to reduce this effect as much as possible, a set of three adjustable apertures exists in the A1900 (see Fig. 3.1) to cut out some of the other secondary beams. At the second image location in the A1900 (see Fig. 3.1) there exists an achromatic aluminium wedge that is used for isotopic beam separation. The wedge is in fact of uniform thickness but curved so that the various secondary beams incident at dispersed points on the wedge experience different effective thicknesses. Each beam experiences different energy losses through the wedge, and beam components with the same $B\rho$ but different atomic numbers will emerge with different momenta. Further separation and identification of the beam constituents are carried out by measuring the time-of-flight of particles between two scintillators after the A1900. One of these scintillators, the Extended Focal Plane (XFP) scintillator, is located near the end of the A1900 (far right of Fig. 3.1), whereas the second, object (OBJ) scintillator is located further down the beamline, a few metres upstream of the experimental station.

The secondary beams utilised in this work (^{71}Br , ^{70}Se and ^{69}As) left the A1900 with intensities (purities) of 1.5×10^5 pps (8%), 7.1×10^5 pps (38%) and 7.4×10^5 pps (39%), respectively. A small amount of ^{68}Ge secondary beam also made it through the A1900 (6% beam purity), however the corresponding reaction products were not sufficiently populated to be of use in the analysis.

Additional radioactive recoils were created at the secondary target position in the S800 vault (discussed in the next section). The secondary beams (^{71}Br , ^{70}Se and ^{69}As), reaching the reaction target with energies of approximately 90 MeV/u, impinged on a 96 mg/cm^2 Be target and generated excited recoils via different reaction mechanisms such as single-/multiple-nucleon knockout, inelastic scattering and nucleon pickup. The recoils studied in this work (^{62}Zn , ^{70}Br , ^{68}Se , ^{72}Kr , ^{70}Se , ^{66}Ge , ^{69}Se and ^{65}Ga), along with many other reaction products of lesser interest, γ decayed in flight and passed into the S800 spectrograph where they were identified.

3.2 Experimental Devices

3.2.1 The S800 Spectrograph

The secondary beams emerging from the A1900 created many excited recoils at the secondary target position, and without some form of particle identification it would be impossible to discern the γ -ray transitions of interest amongst the forest of other de-excitations. The S800 is a large-acceptance, high-resolution particle spectrograph [57] designed to identify fast recoils leaving the secondary target position. It is a three-storey structure (see Fig. 3.2) with the secondary target position on the lowest floor and the focal plane detectors on the top floor. The recoils are bent up to the focal plane by two superconducting dipole magnets. The 250 ton spectrograph is capable of being rotated about a pivot point between 0° and 60° . It covers a solid angle of 20 msr, described roughly as an ellipsoid of $\pm 3.5^\circ$ in the dispersive plane (the plane in which the beam is dispersed) and $\pm 5^\circ$ in the non-dispersive plane [57], and has a momentum acceptance of $\pm 2.5\%$.

The components of the S800 can be broken down into two areas:

1. **The analysis line:** This part of the device spans from the object (OBJ) scintillator position to the secondary target position, and consists of four 22.5° dipole magnets, five quadrupole magnets and a few correcting sextupoles. It is used for beam tuning, implementation of the optical modes (see below) and incoming particle identification via the time-of-flight technique. The maximum magnetic rigidity of this section is around 5 Tm.
2. **The spectrograph:** This is the section of the S800 that spans from the secondary target position to the focal plane, encompassing two large-bore focusing quadrupole magnets, two 75° superconducting dipole magnets and the focal plane detectors. This is the large acceptance section. Typical maximum magnetic rigidity is 4 Tm for the dipole magnets.



Figure 3.2: Photograph of the S800 spectrograph located in the S3 vault at NSCL, MSU. The target position, with the SeGA array affixed around it, is in the bottom left of the picture. Particles entering from the bottom left of the picture react at the target position and are curved up by the two dipole magnets (sections of which can be seen between the railings on the right, coloured brown). The particles then pass into the focal plane (top left) where they are identified.

Optical Modes

The S800 spectrograph is capable of being operated in three optical modes. When this experiment was performed (December 2011) only two of the three modes were available. The third mode will therefore not be discussed.

1. **Dispersion-matched mode:** This mode of operation involves the whole of the S800 being achromatic, including both the analysis line and the spectrograph itself. This mode of operation ensures the momentum spread of the beam at the object (OBJ) position is cancelled out at the focal plane. Using

this optical mode it is necessary that the beam is dispersed on the target, which restricts the maximum momentum acceptance of the analysis line to $\pm 0.5\%$. This mode is desirable if good energy and momentum resolution of the S800 is required as this mode requires no momentum tracking of the incoming particles.

2. **Focused mode:** This optical mode involves only the analysis line being achromatic. The beam therefore is focused onto the target. In this case the spectrograph is not achromatic, so the momentum spread of the beam at the object position is not cancelled out at the focal plane. This mode is chosen if a larger momentum acceptance is preferred in the analysis line. Experiments that require the use of small targets are set up in focused mode. A typical momentum acceptance in this configuration is $\pm 2\%$. The experiment discussed in this work utilised this optical mode.

S800 Focal Plane Detectors

The S800 spectrograph is primarily designed for recoil identification. Almost all the detectors for this purpose reside at the focal plane (at the very top of the photograph shown in Fig. 3.2), and have cross-sectional dimensions of around 30 cm width and 60 cm height. The focal plane detectors comprise two cathode ray drift chambers (CRDCs), an ion chamber and three plastic scintillators: E1, E2 and E3, with thicknesses of 3 mm, 5 cm and 10 cm, respectively. An electronic ‘S800 singles’ trigger is derived from the fast timing signal of the E1 scintillator, which drives the data acquisition system by beginning data electronic readout (see Subsection 3.2.3).

Time-of-flight detectors: The principal secondary beams (^{71}Br , ^{70}Se and ^{69}As) were separated via their time-of-flight between two plastic scintillators, one held at the extended focal plane position of the A1900 fragment separator (XFP) and one held at the object position upstream of the secondary target position (OBJ). A variant of this technique, performed at NSCL but using scintillators at different positions, can be found in Ref. [58]. The difference in timing between the two scintillators with respect to the common S800 trigger provided by the E1 scintillator was used as a secondary beam identification technique. This technique can accurately separate secondary beam components according to their mass-to-charge ratio, allowing software cuts to be applied which can select individual secondary beam species

3.2. EXPERIMENTAL DEVICES

and the resultant reaction products created at the target position (see Section 4.3 and Fig. 4.7).

The two scintillators were monitored during the course of the experiment for evidence of degradation due to radiation damage from the beam, which hinders the ability to separate different secondary beam components based on their time-of-flight. The beam position on the scintillators was moved a few times during the course of the experiment to minimise degradation.

Cathode ray drift chambers: Two CRDCs were used for position and angle determination. These detectors, with 0.5 mm position resolution in both dispersive and non-dispersive planes, are designed to measure the position and angles of recoils in the focal plane. The two detectors, placed one metre apart, offer an active area of ± 28 cm and ± 13 cm in the dispersive and non-dispersive planes, respectively, and have an effective depth of 1.5 cm. The CRDCs are filled with a gas mixture of 80% CF_4 , 20% Isobutane held at a pressure of 50 torr [59]. Upon interaction with the beam recoils, ion-electron pairs are created in the volume. These electrons drift through a Frisch grid and are accelerated in the increased field around the anode wire, creating Townsend avalanches and a multiplied signal. The charge on the anode wire then induces a signal on a cathode pair either side of the wire. The cathodes are separated into 224 pads in a linear chain that can be read out individually. The dispersive plane position (x) is determined by the position sensitivity of this cathode chain. The position in the non-dispersive (y) direction is determined via the electron drift time by comparison to the S800 singles trigger provided by the E1 scintillator. Since the detection process involves the use of drift electrons in a gas, the responses are rather slow ($\simeq 20 \mu\text{s}$ per event). The maximum available counting rate for acceptable functionality is around 5000 counts per second; count rates any higher than this result in efficiency losses. The CRDC detectors are therefore unable to deal with very high counting rates. This is the main limiting factor for rates in the SeGA γ detectors (see Subsection 3.2.2). The (x,y) position information for each recoil extracted from the CRDCs was used to calculate recoil trajectories; specifically, it allowed the determination of the angular distribution at the focal plane in the dispersive and non-dispersive planes (denoted a_{fp} and b_{fp} , respectively). These focal plane angles are used in combination with the inverse map (see Section 4.2) to reconstruct the recoil angles at the target position, a_{ta} and b_{ta} . Since the second CRDC is placed at the optical focus of the spectrograph, the

(x,y) information extracted gives the position of the recoil at the focal plane in the dispersive and non-dispersive planes (x_{fp} and y_{fp} , respectively).

Ionisation chamber: Downstream of the two CRDCs there exists a Frisch-gridded ion chamber for energy loss measurements. The chamber consists of sixteen one-inch anodes made of aluminium-evaporated mylar foil. The ion chamber is conventionally filled with P10 gas (90% argon, 10% methane) at a maximum pressure of 600 torr. The recoils travel perpendicular to the anodes and between the cathode and Frisch grid. Electron-ion pairs are created and the electrons are collected on the anode pads. The energy loss measurements provide a charge separation, which can be used along with timing information (a mass/charge separation) from the scintillators to create recoil identification plots (see Fig. 4.8). The pads were calibrated against each other in order to extract the average energy deposited by the recoils. This was done by measuring the energy loss in each of the pads individually and using the Gaussian distribution of energies to extract an average. All sixteen pads were used for this, unless one of the pad energy measurements fell outside a standard deviation of the mean. If this occurred the pad was neglected and the energy was averaged from the remaining pads.

3.2.2 The Segmented Germanium Array

The Segmented Germanium Array (SeGA), developed for use with intermediate-energy radioactive ion beams, consists of a set of segmented germanium γ -ray detectors placed around the secondary target position. The fifteen detector crystals used in this experiment were held in two separate rings, one at 30° and one at 140° (relative to the beam axis). Seven of the detectors were placed in the forward ring and eight in the backward ring. The lack of an eighth detector in the forward ring was due to space limitations; the large-bore quadrupole magnet of the S800 spectrograph is too large to accommodate a SeGA detector at this position. Each detector was plugged into an individual DAQ card in the electronics (discussed in Subsection 3.2.3). The array is shown in Fig. 3.3.

The SeGA detectors are n-type coaxial HPGe crystals with an external diameter of 70 mm and length of 80 mm. The outer contact of each crystal is electronically segmented into eight 1 cm-thick slices axially and further split into four radially,

3.2. EXPERIMENTAL DEVICES

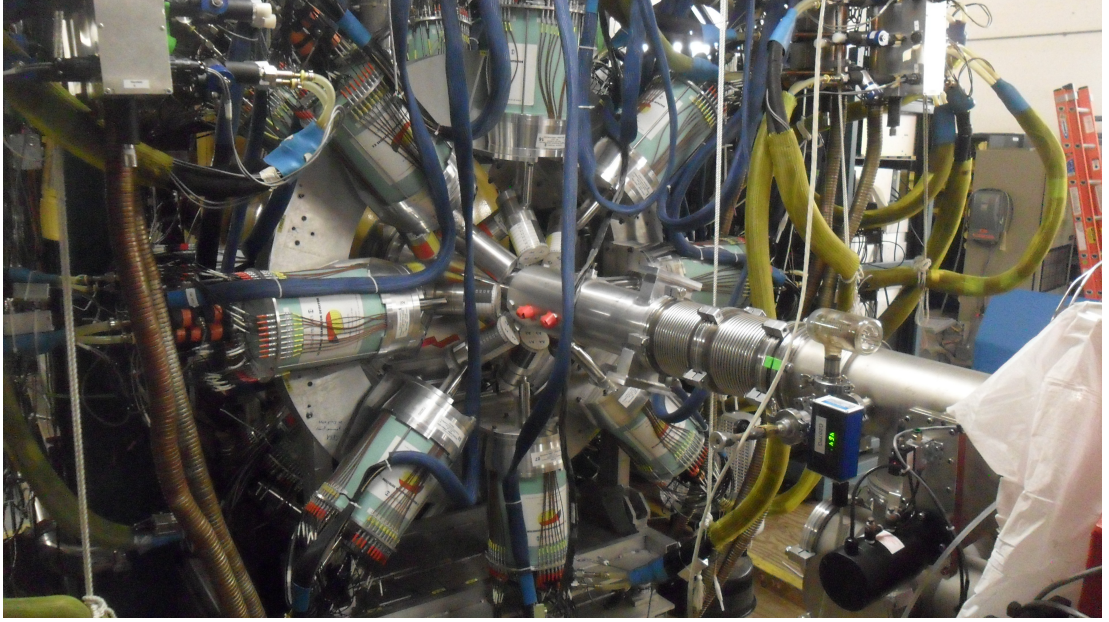


Figure 3.3: Photograph of the SeGA array surrounding the secondary target position after the detectors had been mounted on the frame. The photograph was taken from upstream of the array relative to the beam direction, so the ring visible at the front of the picture is the backward (140°) ring.

thus totalling thirty-two segments. The crystal is segmented this way because of its the orientation with respect to the target position. Each cylindrical crystal is orientated with its axis of symmetry running perpendicular to the target-to-detector radius. A diagram illustrating the labelling scheme of the detector segments is given in Fig. 3.4.

Each detector crystal is operated by a room temperature field effect transistor (FET) accessible from outside the cryostat. Whilst having cold FETs would increase the resolution, having them inside the cryostats would make them less easily accessible for repairs. The FETs are connected to 33 independent charge-sensitive preamplifiers, each with a 30 ns rise time at 0 pF. A time constant of 50 μ s and gains of 300 mV/MeV are typical of these preamplifiers, which are attached to the base of the liquid nitrogen dewars. For normal operation, a bias of between +4 kV and +5 kV is applied to the central contact of each crystal.

HPGe detectors are chosen over scintillator detectors like NaI(Tl) due to their superior resolution. Intrinsic resolution for Ge detectors is on the order of 0.1% at 1.33 MeV, compared to the $\sim 7\%$ typical of a NaI scintillator detector at the same

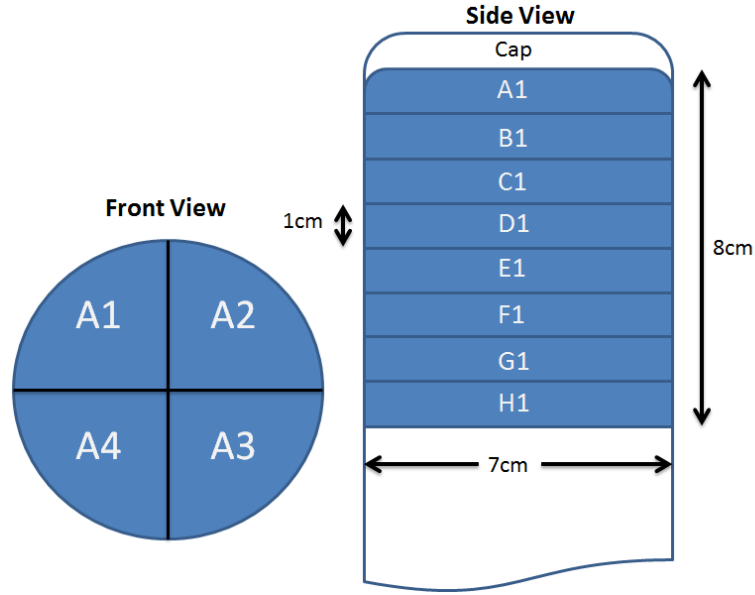


Figure 3.4: Schematic showing how the individual 32 segments of a SeGA crystal are labelled. Measurements shown are not to scale.

energy. Semiconductor detectors are however hampered by lower efficiency, and so they generally need to be moved closer to the source. This adds to the resolution as it increases the opening angle of the detector crystal. Electronic segmentation offers a partial solution to this problem; by segmenting the crystal it is possible to get a measure of where the γ ray interacted, and thus improve the position reconstruction and energy resolution. Reviews of other segmented Ge arrays can be found in Refs. [60–62].

The finite width (resolution) of γ rays recorded in SeGA is caused by three main effects:

1. Uncertainty in the source velocity. This is primarily due to ions gradually slowing down as they pass through the target foil, experiencing a range of velocities within the foil and constant velocities in the vacuum between the foils.
2. There is uncertainty in the emission angle of the γ ray due to the finite opening angle of the detectors. Uncertainty in the angle of the recoil relative to the beam axis also adds to the overall resolution.
3. The detector has an intrinsic resolution as a result of effects such as fluctuation

of the number of electron-hole pairs created at a given γ -ray energy. This represents the limit of the possible peak widths in the absence of any other effects.

These three effects, discussed for SeGA in Ref. [63], contribute to the total energy resolution according to the following relation:

$$\left(\frac{\Delta E_\gamma}{E_\gamma}\right)^2 = \left(\frac{\beta \sin\theta}{1 - \beta \cos\theta}\right)^2 (\Delta\theta)^2 + \left(\frac{\beta - \cos\theta}{(1 - \beta^2)(1 - \beta \cos\theta)}\right)^2 (\Delta\beta)^2 + \left(\frac{\Delta E_{intr}^{lab}}{E_\gamma}\right)^2 \quad (3.2)$$

where β is the velocity of the de-exciting recoil, θ is the observation angle of the γ radiation and ΔE_{intr}^{lab} is the energy-dependent intrinsic detector energy resolution as measured in the lab frame. The three quantities on the right of Equation 3.2 refer to the three respective contributions listed above.

Detector Challenges

A number of experimental challenges present themselves when dealing with Ge detector arrays. One such issue is resolution degradation due to ambient noise in the experimental hall. Ambient noise can come from a number of places, such as from the surrounding electronics or microphonic vibrations from mechanical equipment in the hall. When the liquid nitrogen dewars are filled - a process that occurs once every six hours - vibrations in the filling lines could also have a detrimental effect on the resolution of the detectors. Studies during the commissioning of SeGA [63] showed there were no adverse effects on the energy resolution of the detectors when exposed to up to 85 dB (decibels relative to signal carrier) of noise near the crystal. Even though activities such as liquid nitrogen filling were unlikely to have degrading effects on the resolution, data taken during liquid nitrogen fills were restricted to separate runs in case they had to be removed from the sorts. It was found that liquid nitrogen filling had no detrimental effects on the SeGA detector resolutions during this experiment and so the filling runs were included in the sorts.

A concern when operating segmented germanium detectors is the possibility of elec-

tronic pick-up between neighbouring segments. Interactions in one segment may induce spurious charges in the nearby segments, leading to a false signal. A study was performed during the commissioning of SeGA [63] using a collimated ^{60}Co source shone on individual segments. The effects of pick-up were deemed negligible.

Due to the small segment sizes and the energy of the incident γ radiation, it is unlikely that the incoming photons will only interact in one segment. It is likely they will Compton scatter through a few segments during the interaction. It is important that one identifies the position that the photon first interacted with the detector in order to achieve reliable Doppler correction. This is done by assuming that the segment recording the highest energy in a given γ event is the position of first interaction.

Radiation damage is an effect present in γ detectors that have been exposed to charged particle or neutron radiation. The presence of charge trapping centres created by radiation damage results in only some of the electrons from an interaction in the detector volume being collected at the electrode. This gives a low-energy tail to γ -ray distributions. If detected before the experiment the damage can be almost entirely removed by annealing at a heightened temperature [64]. The SeGA detectors in this work showed no evidence of radiation damage at the beginning of the experiment.

3.2.3 Data Acquisition System

An analogue data acquisition (DAQ) system was used in the experiment. The basics of the trigger logic are discussed below. See Ref. [57] for more details.

A γ -ray energy threshold in the SeGA detectors is set by the user, and the data capturing process will only be initiated if an energy pulse above this threshold is detected in one of the SeGA central contacts. A coincidence window of a user-defined length is then opened by the DAQ. During the time this window is open, the system computes the event multiplicity based on the number of events detected in the SeGA detectors. The DAQ will only continue if the multiplicity satisfies a user-defined condition. A validation window of a user-defined length is opened, with the condition that an external validation from the S800 must be received within the

window. The validation window signal is transferred to the analogue electronics of the S800. If the time difference between the validation signal and the recoil signal from the E1 scintillator falls within the coincidence window controlled by the S800, the S800 electronics issues a master coincidence trigger. This master coincidence trigger serves a dual purpose; it initiates the writing of the S800 residue data to disc, and also acts as an external validation window for the DAQ. In the experiment analysed in this work, the master coincidence trigger was sent out only when a reaction residue *and* at least one γ ray were detected within the coincidence window. The arrival of the external validation pulse from the S800 electronics prompts a ‘record’ trigger signal to be sent out. The modules that were flagged by the hit pattern information then assemble data files with timing and energy information. An event number is stored in the header of each recorded module data file, and these are used to assemble the files together with a condition placed on matched timestamps. This action is performed on a dedicated event-building Linux PC after the run ends.

3.3 Experimental Techniques

3.3.1 The Recoil Distance Doppler Shift Method

The recoil distance Doppler shift (RDDS) method is a dedicated experimental technique for the measurement of excited state lifetimes in the 10^{-12} - 10^{-9} s region. The basic technique has been around for a number of decades, having been first developed between 1949 and 1965. A number of early reviews, such as Ref. [65], detail the development of the method at these early stages in its evolution. The central attraction of this technique was its relative simplicity; excited state lifetimes can be determined entirely from quantities directly measured in an in-beam experiment, and the method is model independent.

Despite the success of the RDDS technique in the decades that followed its inception, early experimental results turned out to contain systematic errors. The errors were put down to the influence of level feeding from higher-lying excited states and de-orientation effects [66]. These problems were known at the development stages of the approach, but it was nevertheless the case that incorrect estimates were applied or

the full picture of the decay structure was not sufficiently understood. An extensive review of the RDDS technique and related physics, concentrating on developments and refinements achieved in the past two decades, can be found in Ref. [67].

Target and stopper foils used for RDDS lifetime measurements (see below) are typically housed in a device called a plunger. Plungers are hollow metal tubes (to allow for the passage of the beam) with reaction foils placed at the downstream end.

RDDS Studies With Standard Plungers

The original plunger devices used for RDDS lifetime measurements consisted of two foils: a target foil where the beam-induced reaction takes place and a thick stopper foil designed to bring the recoiling residues to rest. At time $t = 0$ excited states are populated in a recoil nucleus in a reaction between an incoming beam nucleus and the target. Thanks to the large momenta involved in the reaction, the excited nucleus leaves the target and travels for a well-defined flight time $t_f = x/v$, where v is the velocity of the recoil and x is the separation distance between the target and the stopper. The recoiling nucleus, which is in an excited state, can de-excite to the ground state via the emission of electromagnetic radiation. If the γ ray is emitted in flight, a detector positioned at an angle θ with respect to the beam axis will measure a Doppler-shifted energy, E_{lab} , given by:

$$E_{lab} = E_{rest} \frac{\sqrt{1 - \beta^2}}{1 - \beta \cos \theta} \quad (3.3)$$

where $\beta = v/c$ and E_{rest} is the energy of the transition in the recoil's rest frame.

What one observes in the resulting Doppler-corrected γ -ray spectrum, presuming the recoil has been cleanly selected, is the presence of two peaks. These peaks, usually referred to as the *shifted* and *unshifted* components, have intensities that represent decay probability in flight and after being slowed to rest in the stopper, respectively. If the distance between the target and stopper is altered over the course of the experiment, the corresponding intensity changes in the two peaks give an indication of the lifetime of the decaying state.

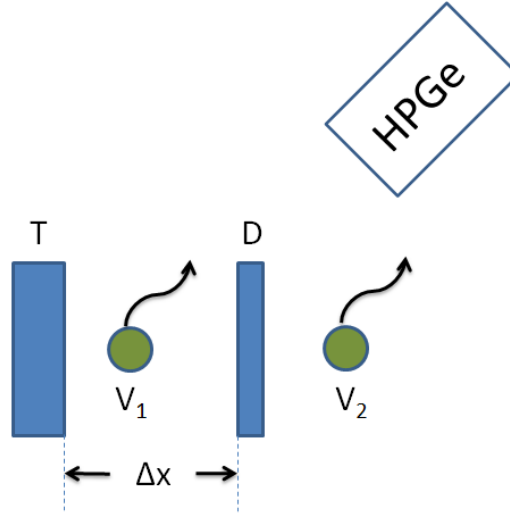


Figure 3.5: Schematic of the RDDS technique for a fixed target-degrader separation Δx . Recoils (travelling from left to right) are created in an excited state in the target foil (T) and γ decay in flight further downstream. Nuclei de-exciting before and after passing through the degrader foil (D) will have velocities v_1 and v_2 , respectively (where $v_1 > v_2$). The presence of the degrader foil creates two resolvable peaks in the γ -ray spectrum.

RDDS Studies With Differential Plungers

A modification to the standard plunger is necessary if the recoils are to be identified by a mass spectrograph after the target, which is the case with the S800. This would be impossible if the recoils were fully stopped in the second foil. In such cases the stopper is replaced with a thinner degrader or retardation foil, originally proposed by Ward *et al.* [68] as a solution to avoid long slowing times in the stopper. It is important that the degrader foil is sufficiently thin that the recoils pass through in a negligible time compared to their lifetime. However, it is also important that the material is sufficiently thick to slow down the recoils and create two resolvable γ -ray peaks. The process is shown schematically in Fig. 3.5. The components corresponding to decays before and after the degrader foil are usually called the *undegraded/fast* and *degraded/slow* components, respectively. In this thesis the components will be referred to as fast/slow throughout.

Challenges For RDDS Analysis

In a lifetime experiment using a plunger device, there are a number of effects that must be taken into consideration when analysing the resulting γ -ray spectra. Such physical processes can affect γ -ray peak widths, the relative intensities of the RDDS peaks and the angular distribution of photon emission. Performing RDDS with fast radioactive beams creates further experimental challenges that may be negligible with slower beams (see Ref. [69]). The central considerations are given below.

Observed feeding: Excited states are fed by transitions from higher-lying excited states (referred to in this text as *feeding states*). If this feeding is ignored then one would overestimate the lifetime of the state of interest, as the higher-lying states themselves have finite lifetimes and so delay the decay of the depopulating state. The effect of feeding states can be included by measuring the intensities of the feeding transitions and the effective lifetimes of the corresponding feeding states. Effective lifetimes are not true lifetimes, as they include the delaying effect of all higher-lying states that depopulate through the feeding state. In this work, it was possible to extract the effective lifetimes of almost all feeding states. When it was not possible to measure the effective lifetime of a feeding state, either the literature lifetime was assumed or a justifiable assumption was made. Where this is done in the analysis (see Chapter 5) it is explicitly stated.

Side-feeding: Side-feeding is an issue with γ -ray singles data, in that the depopulating state can potentially be fed by states that exhibit no observable γ -ray transition peaks. The intensity of these feeding states can be determined by balancing the populating and depopulating transition intensities. An empirically justified assumption about the average lifetime of the side-feeding states can be made (for example, that the average lifetime of all side-feeding states is negligibly short in comparison to the lifetime under investigation). A nucleon knockout RDDS study of the 2_1^+ lifetime in ^{64}Ge [6] showed that unobserved side-feeding had a negligible effect on the extracted 2_1^+ state lifetime despite it accounting for 40% of the feeding intensity. Most of the nuclei in this work were populated via nucleon knockout reactions, which tend to populate low-lying excited states directly. Therefore it is assumed throughout this analysis that the delaying effects of unobserved side-feeding are negligible.

Nuclear alignment: It was assumed that the γ -ray angular distributions of all depopulating transitions were isotropic. However, in the case of single/two-nucleon knockout it is possible that some alignment of the outgoing recoils occurs in space. This leads to different angular γ -ray distributions for dipole and quadrupole transitions [70] compared to the non-aligned case, i.e., where these distributions are completely washed out. If there is a significant nuclear alignment, and this is ignored in the analysis (by assuming isotropic γ distributions), the intensities of dipole and quadrupole transitions relative to each other will be incorrectly deduced. Multiple-nucleon knockout and inelastic scattering reactions are expected to produce isotropic distributions [71]. Nuclear alignment is not believed to be significant with fast radioactive beams, even for nucleon knockout reactions, as the de-orientation effect acts to rapidly destroy any spatial alignment of recoils upon leaving the target foil [66].

Absolute foil separation: Measuring the absolute separation distance between the target and degrader foils in an RDDS experiment is essential to extract accurate state lifetimes. The techniques used to obtain this separation distance are discussed in Subsection 3.3.3. There is a range of target-degrader distances that is very sensitive to the lifetime of the state. It lies around the approximate ‘mean distance’ of the state, $x = v\tau_{lab}$, where τ_{lab} is the mean lifetime in the lab frame. Around this region the relative intensities of the ‘fast’ and ‘slow’ RDDS peaks change dramatically. For the most part, lifetimes measured in this work were on the order of picoseconds. The recoils left the target foil in TRIPLEX at an approximate speed of $0.4c$, therefore the mean distance for a state of lifetime $\tau = 3$ ps ($\tau_{lab} = 3.3$ ps) is ~ 360 μm . This distance includes the finite thickness of the target, which in the case of this experiment was 500 μm . Assuming the recoils were created in the centre of the target and live for $\tau = 3$ ps, on average they travel ~ 110 μm from the surface of the target before decaying. The ideal location of the degrader foil for this experiment would therefore be ~ 110 μm from the back face of the target foil.

Finite foil thickness: In this experiment thick target foils were used (96 mg/cm^2 Be target, 403 mg/cm^2 Ta degrader). The finite thickness of the foils gives a broadened velocity distribution to the recoils due to continuous slowing in the foils. Faster recoils emerging from the target reach the degrader before the slower recoils and hence contribute less to the ‘fast’ component in the γ -ray spectra. A thick target foil also produces an uncertainty in the location of recoil excitation (for purposes of

Doppler correction, excitation is usually assumed to occur in the centre of the foil). These effects, collectively known as Doppler shift attenuation, place a limitation on the lifetimes measurable using the RDDS technique, since if the depopulating state lifetime is less than the flight time through the foils only one γ -ray peak will be observed. The various challenges of lineshape fitting are discussed in Ref. [72] with some proposed solutions. The effects of recoil energy loss in various materials can be replicated in programs such as LISE++ [73], which can be set up to accurately reflect the NSCL beamline parameters and other experimental conditions. All lifetimes in this work were sufficiently long that the recoils travelled downstream of the target foil before decaying, nevertheless the finite thickness of both the target and degrader foils created lineshape effects. The analysis of lifetimes in this work took these effects into account (see Section 4.4).

Degrader excitation: Reactions in the degrader foil can cause recoil nuclei to be excited. These decay in flight after the degrader even if their lifetime is very short. This adds counts to the ‘slow’ RDDS γ -ray peak of a transition and leads to an erroneously long lifetime being extracted if not taken into account. To measure the level of degrader excitation, data from a large target-degrader separation are taken. At very large distances, the flight time between the foils is much larger than the lifetime of the state being measured. Therefore, in principle, all recoils created in the target would have de-excited by the time they reached the degrader. Any counts in the ‘slow’ RDDS peak at this separation will be entirely down to degrader excitation, which is a constant that can be applied to all distances. See Section 4.6 for more details.

Relativistic effects: Time dilation occurs at relativistic speeds and affects the measured lifetime of a depopulating state in the lab frame τ_{lab} , which is related to proper lifetime τ according to the following relation:

$$\tau_{lab} = \frac{\tau}{\sqrt{1 - \beta^2}}. \quad (3.4)$$

In addition to this, aberration effects result in a change of emission angle in the laboratory system relative to the moving system, as described by

$$\cos(\theta_{lab}) = \frac{\cos(\theta) + \beta}{1 + \beta\cos(\theta)}. \quad (3.5)$$

Recoils also receive a Lorentz boost, which is a change in the solid angle of emission due to the relativistic transformation, given by

$$\frac{d\Omega}{d\Omega_{lab}} = \frac{1 - \beta^2}{(1 - \beta\cos(\theta_{lab}))^2}. \quad (3.6)$$

3.3.2 The γ -ray Lineshape Method

The RDDS technique fails when the lifetime of the decaying state is much shorter or longer than a picosecond. For long-lived states on the order of hundreds of picoseconds, a different technique can be used to measure the lifetime. In experiments similar to this work, a recoil excited in the target foil at the centre of the SeGA array travels downstream at a speed of approximately $0.3c$ after being slowed in the degrader foil. If the nucleus is in an excited state with a long lifetime, e.g., on the order of hundreds of picoseconds, its position relative to the SeGA array will have changed significantly by the time the γ ray is emitted (e.g., for a 300 ps lifetime ($\tau_{lab} = 330$ ps), a recoil would have travelled ~ 3 cm from the centre of the array). The Doppler correction applied to γ spectra to change from the lab frame to the recoil rest frame assumes that the decay occurred at the target position, which is incorrect. The Doppler correction, therefore, gives a tail to the γ -ray transition peaks from these long-lived states. Examples can be seen in a number of figures in this work (e.g., see Fig. 5.21). The long lifetime of the decaying state also acts to shift the measured γ -ray centroid down in energy relative to the true value, again due to the incorrect assumption of position in the Doppler correction. The resulting lineshape and centroid shift of the γ -ray peak is strongly dependent on the lifetime of the decaying state, therefore analysis of this lineshape can be used to extract lifetimes on the order of hundreds of picoseconds. The extraction of long lifetimes, using fits to simulated γ spectra, is discussed in Ref. [10].

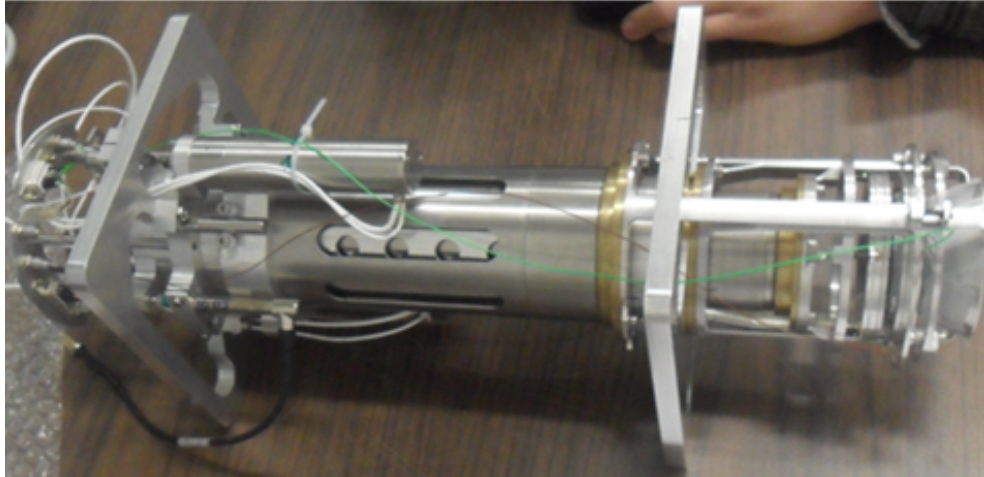


Figure 3.6: Photograph of the TRIPLEX plunger shortly after the foils were mounted. The foils reside at the downstream end on the right-hand side. TRIPLEX contained a 96 mg/cm^2 ^9Be target foil, a Ta degrader foil of 403 mg/cm^2 and a thin polypropylene charge stripping foil. The motors for controlling the target-degrader separation are housed towards the left of the device.

3.3.3 The TRIPLEX Plunger

To facilitate the reactions required for the experiment analysed in this work, the secondary beams leaving the A1900 separator impinged on a 96 mg/cm^2 ^9Be target foil housed in a plunger device at the target position of the S800 spectrograph. The TRIPLE PLunger for EXotic beams (TRIPLEX), developed by the Köln-NSCL collaboration [74], was utilised in this work. The present experiment was the commissioning run of TRIPLEX. This plunger is designed to house up to three target or degrader foils, but in this experiment only a single target and one Ta degrader foil of 403 mg/cm^2 were used. The third position housed a thin polypropylene charge-reset foil, used for removing electrons picked up by the recoil nuclei in the earlier foils and making sure there are not multiple charge states of individual recoils passing into the S800 focal plane. TRIPLEX is designed to hold foils of a maximum size of $50\text{mm} \times 50\text{mm}$. These foils are typically attached to the frames of the plunger housing using glue. A photograph taken of TRIPLEX shortly before the experimental run is shown in Fig. 3.6.

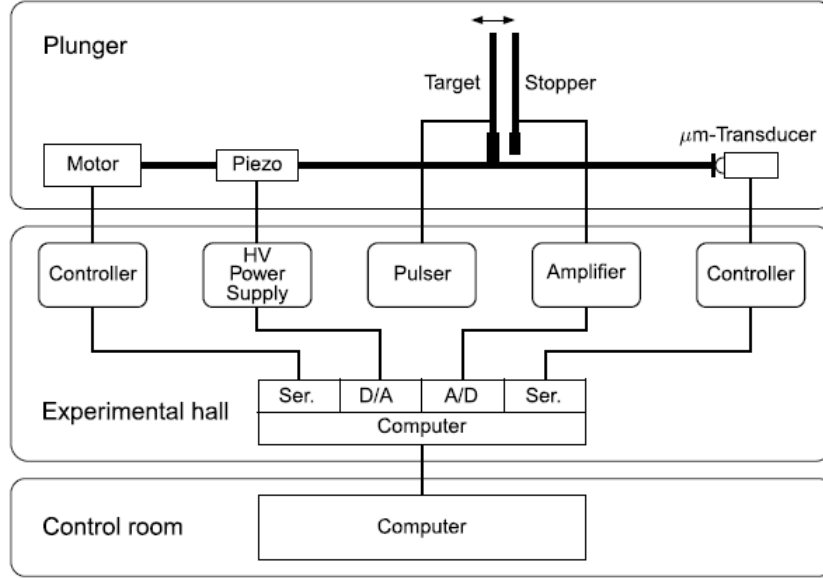


Figure 3.7: Diagram showing the electronics of the plunger control feedback system. Motors and an HV supply are connected to a computer in the experimental user area via vacuum feedthroughs. A stopper foil is mentioned instead of a degrader foil in this figure, but the electronics layout is identical. Diagram taken from [67].

Plunger Alignment

Aligning the plunger correctly inside the beam pipe at the target position is highly important as it is necessary for the beam to pass unhindered through the bulk of the plunger structure before hitting the foils at the downstream end. The plunger is placed in such a position that the fixed degrader is held close to the S800 pivot point [75, 76].

The alignment procedure was performed by professionals from Köln. A surveyor's telescope was erected between the last two S800 quadrupoles and aligned to the beamline by the use of a crosshair placed over the entrance to the final S800 quadrupole. Once the alignment was completed, a mock plunger housing (measuring the same dimensions as TRIPLEX) was inserted with a crosshair cap over its downstream edge. The plunger was aligned and held in place by a set of screws tightened from the outside of the beam pipe. Once the alignment was finished, the screws on the top of the pipe were loosened and the mock plunger was removed. TRIPLEX was then inserted and tightened into place.

Vacuum feedthroughs were used to connect the plunger motors to the outside world, and a computer in the experimental vault was used to control the set-up. The basic electronics layout is shown in Fig. 3.7.

Target-Degrader Distance Controls

A set of plunger-mounted Exfo Burleigh Inchworm Motors was used to control the target-degrader distance with micrometer precision. In this set-up, the degrader was at a fixed position and the target-degrader separation was changed by altering the position of the target. The motion set-up consisted of three piezoelectric transducers (PZT), a type of actuator made from ceramic. These devices are particularly useful as their expansion along one dimension can be accurately controlled by an applied electric field. The conventional PZT system, shown schematically in Fig. 3.8, consists of three physically connected but independently biased crystals. Two of these crystals act as clamps on the axis shaft and the third acts as an expander that moves the frame along the axis. PZT systems are beneficial because of the lack of mechanical vibration, allowing a precise foil separation to be maintained.

The Inchworm Motor system was used to monitor the distance between the two foils in the plunger repeatedly during the course of the experiment. Heating effects due to the beam current and other forms of noise cause a fluctuation in the absolute distance between the foils, which is corrected by the feedback system. Distance monitoring data were taken continuously during each distance run. Fluctuations were small ($\pm \ll 1 \mu\text{m}$) but still present, creating a Gaussian distribution around a mean target-degrader separation value (the centroid in Fig. 3.9).

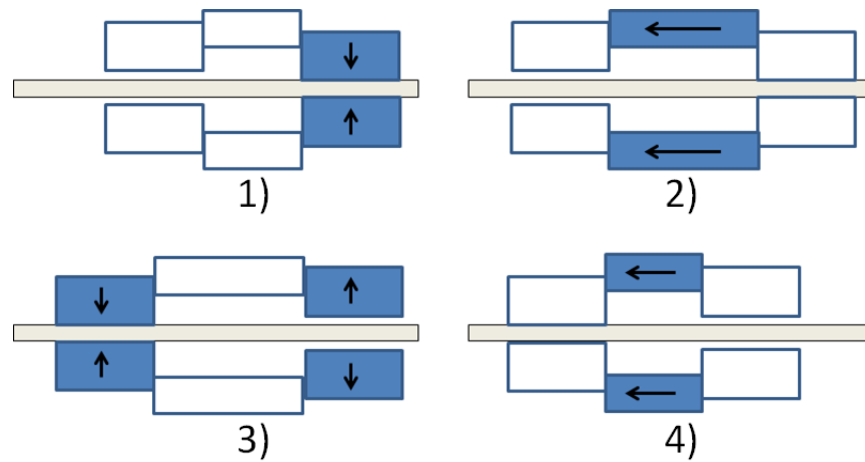


Figure 3.8: Cross-section schematic of the piezoelectric transducer (PZT) system used in the TRIPLEX plunger, showing as an example how the target frame is moved one arbitrary increment to the left. The axis shaft is shown in beige and the PZT components are shown as blue-lined boxes. The active component at each stage is filled in blue and the direction of expansion/contraction is shown. 1) Right-hand clamps attach to the axis shaft. 2) Central PZT crystal expands. 3) Left-hand clamps shut and right-hand clamps open. 4) Central PZT crystal shrinks. These four steps when repeated move the frame along the axis shaft.

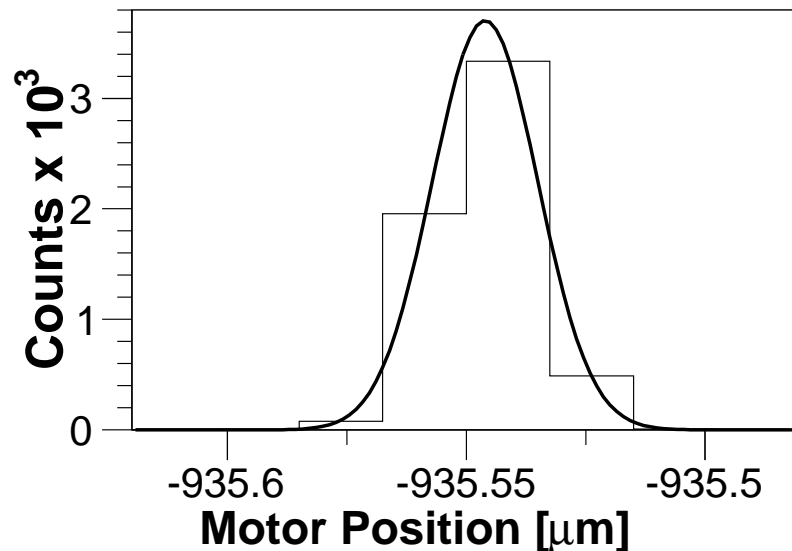


Figure 3.9: Plot demonstrating the level of fluctuation in foil separation for one of the target-degrader distances ($323 \mu\text{m}$). Data were taken over a few runs. The level of fluctuation is given by the FWHM of this distribution, which was determined to be $0.03 \mu\text{m}$.

Chapter 4

Data Analysis

4.1 Offline Analysis With ROOT

Offline analysis of S800 spectrograph data was performed using a dedicated analysis package developed at NSCL. There are two main programs used for the unpacking, calibration and reconstruction of physical events, as well as a histogram viewer and several calibration programs. The codes are written for the use of the ROOT program [77] in the object-oriented C++ language.

Fig. 4.1 schematically shows the processes that turn an uncalibrated .evt file into a calibrated .root file. All data files begin life as a binary .evt file written out by the NSCL DAQ system. These are extracted and converted to .root files using the first of the main programs, *Unpack*. The data are sorted into objects of type ‘S800’ and ‘SeGA’. No corrections or calibrations are performed at this stage, so this step only needs to be performed once. However, with the next stage, calibrations and corrections require the data to be sorted multiple times.

The second stage of the process makes use of the calibration program *Calculate*. Here all detector systems are calibrated, physical events are created using the inverse map (see Section 4.2) and SeGA position measurements are applied. Doppler corrections for the γ rays emitted from the relativistic recoils are performed at this stage also. The data are written to calibrated ROOT trees in .root files.

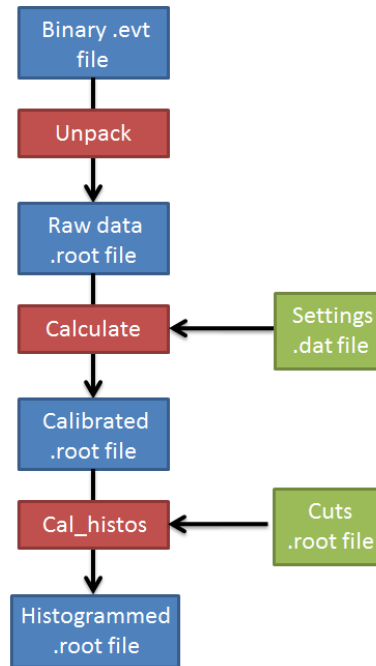


Figure 4.1: Flow chart representing the process of data analysis using the suite of programs developed for S800 data. Input/output files are represented with blue boxes, programs are marked in red and additional files needed by the programs are marked green.

Once calibrated .root files have been created the data can be analysed using the histogramming code *Cal_histos*. Here gates and windows can be applied to the data.

4.2 Focal Plane Corrections And Calibrations

The *Calculate* program, as mentioned previously, applies a series of corrections to the raw uncalibrated .root files created using the *Unpack* code. These calibrations and corrections are applied to the data from a settings text file. The settings file contains all information on S800 and SeGA detector configurations and needs to be optimised before meaningful results can be extracted.

4.2.1 Recoil Trajectory Reconstruction

Analysis of recoil data recorded in the S800 requires the correction of aberrations introduced into the particle tracks by the complex magnetic fields of the apparatus. Whilst the S800 contains a few magnets for basic low-order aberration correction, such as a sextupole embedded in the second focusing quadrupole and edge-flattening trim coils on the dipoles, the majority of higher-order corrections are performed analytically. This analytical reconstruction, known as an inverse map [57], is applied event-by-event to the recoils in the analysis code. Inverse maps are generated post-experiment using a trajectory reconstruction code called COSY Infinity [78], which calculates the aberrations and inverts the polynomial matrix. The code effectively reconstructs the whole trajectory of each recoil retroactively on an event-by-event basis. The method is particularly good as individual particle tracking is not necessary, leading to faster data processing. The technique is not only limited by the accuracy of the inverse map created but also to the accuracy of the recoil position measurements and the incoherent spot size, which is the size of the beam spot at the reaction target position for a given energy component of the secondary beam.

The inverse map relates the position and angle information of the recoils measured at the focal plane (in both the dispersive and non-dispersive directions) to the energy of the recoil, two projections of the scattering angle and the non-dispersive position at the target. The position in the dispersive direction is assumed to be zero as it cannot be reconstructed without introducing too many variables. The inverse map relates the final variables at the focal plane to the initial variables at the target position via the relation:

$$\begin{pmatrix} a_{ta} \\ y_{ta} \\ b_{ta} \\ d_{ta} \end{pmatrix} = S_n^{-1} \begin{pmatrix} x_{fp} \\ a_{fp} \\ y_{fp} \\ b_{fp} \end{pmatrix}. \quad (4.1)$$

Here the terms in the left-hand matrix refer to the two target angles a_{ta} and b_{ta} , the non-dispersive target position y_{ta} and the energy spread at the target position d_{ta} . The terms in the right-hand matrix are the information measured at the focal plane, including the angles of the recoils (a_{fp} and b_{fp}) and the recoil positions in the

4.2. FOCAL PLANE CORRECTIONS AND CALIBRATIONS

Table 4.1: S800 magnet settings during the experiment. Different settings are needed for target-only and ‘distance’ runs since recoils are traversing the S800 at different velocities.

Run type	Variable	Value	Unit
Target-only	Current in magnet I256QA	-44.367	[A]
	Current in magnet I258QB	42.255	[A]
	Current in magnet I265DS	181.195	[A]
	Current in magnet I269DS	181.698	[A]
	$B\rho$	2.66660	[Tm]
Distance runs	Current in magnet I256QA	-33.202	[A]
	Current in magnet I258QB	29.387	[A]
	Current in magnet I265DS	133.861	[A]
	Current in magnet I269DS	134.228	[A]
	$B\rho$	2.01237	[Tm]

second CRDC (x_{fp} and y_{fp}). The inverse map is an inverted nonlinear polynomial matrix S^{-1} of order n .

The generation of inverse maps for experiments performed at NSCL is now easily requested by the user. A URL link [79] allows remote users to retrieve maps by inputting some experimental parameters. For this map generation the magnet currents, the $B\rho$ value and the recoil mass/charge numbers are necessary inputs. Since the fringe fields on the magnets vary substantially with magnet strength, it is important that separate inverse maps are generated for each $B\rho$ setting. These magnet currents, and the corresponding $B\rho$ values of the recoils, are given in Table 4.1 for the present experiment.

4.2.2 Scintillator And CRDC Corrections And Calibrations

The two scintillator detectors placed before the S800 target position record time-of-flight information essential for particle identification. The *Calculate* program, when applied to the raw .root data files, subtracts the master trigger time from the raw time-of-flight values. Corrections applied to the object (OBJ) and extended focal plane (XFP) scintillators depend on the focal plane angles and CRDC positions of

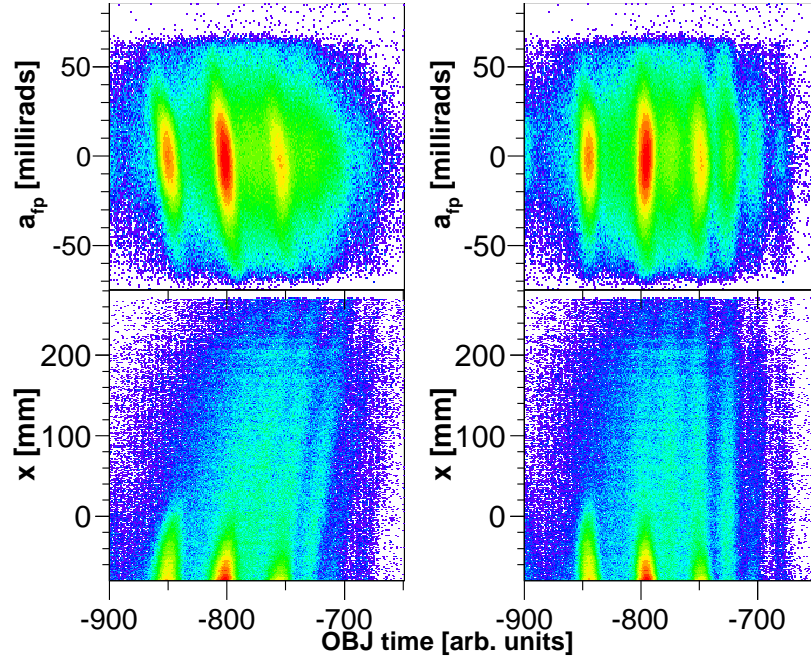


Figure 4.2: Spectra of recoil CRDC angular distribution a_{fp} (top) and CRDC x_{fp} position (bottom) against OBJ scintillator time. The spectra are shown before correction (left) and after (right).

the recoils, since the flight time recorded depends on the recoil trajectory through the S800. These corrections act to align the S800 angle (a_{fp}) and position (x_{fp}) of specific recoils to a common scintillator time. The result of these corrections is shown in Fig. 4.2.

The correction parameters are obtained using a pre-written .C program file that plots a_{fp}/x_{fp} vs. scintillator time and then projects this plot onto the time axis. Parameters are then iteratively adjusted until the distribution widths are minimised. The values obtained are output to the settings file.

Scintillator times tend to drift over the course of many runs. This problem can be overcome by adding an OBJ/XFP time correction to each individual run, lining all runs up to an arbitrary time. Fig. 4.3 shows the effect of this correction. Time corrections were applied to both scintillators.

The individual CRDC pads are calibrated relative to each other using an iterative procedure. Software cuts are made on outgoing recoils and histograms are filled with the value of the CRDC pad with the maximum amplitude. All pads are then

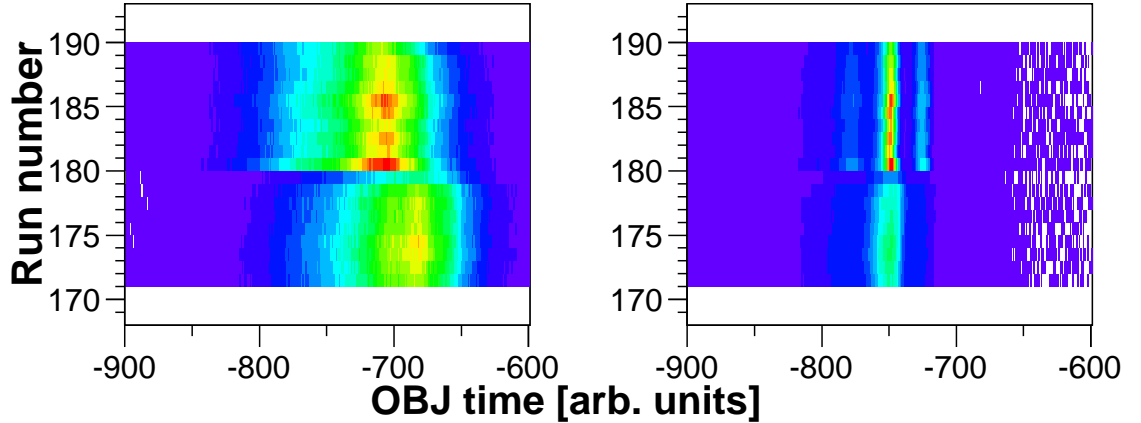


Figure 4.3: Spectra showing OBJ scintillator time gated on incoming ^{70}Se recoils for a range of runs. Shown are the uncorrected OBJ times (left) and the OBJ times after a_{fp}/x_{fp} corrections and a run-by-run OBJ correction to an arbitrary time value (right). The sharpness of the distribution after these corrections is quite apparent.

calibrated relative to some arbitrary channel since no absolute calibration is possible. Fig. 4.4 shows the readouts of individual CRDC pads before and after this calibration is performed.

In order to calibrate the position of the recoils in the CRDCs so they are expressed in millimetres, runs are performed during the experiment with specially made tungsten masks fitted in the beamline. These masks are scored with holes of a known position. Since recoil nuclei can only hit the CRDCs by passing through the holes, the resulting CRDC position spectrum gives an accurate means of calibration. This procedure is done manually, by working out gain and offset values that line up the holes to their correct positions (see Fig. 4.5).

4.2.3 Ion Chamber Corrections And Calibrations

The measured recoil energy losses detected in the 16-channel ionisation chamber depend on the x position of the recoil particle detected in the CRDCs. The energy correction can be calculated using

$$E_{corr} = E \exp(p(x - x_0)) \quad (4.2)$$

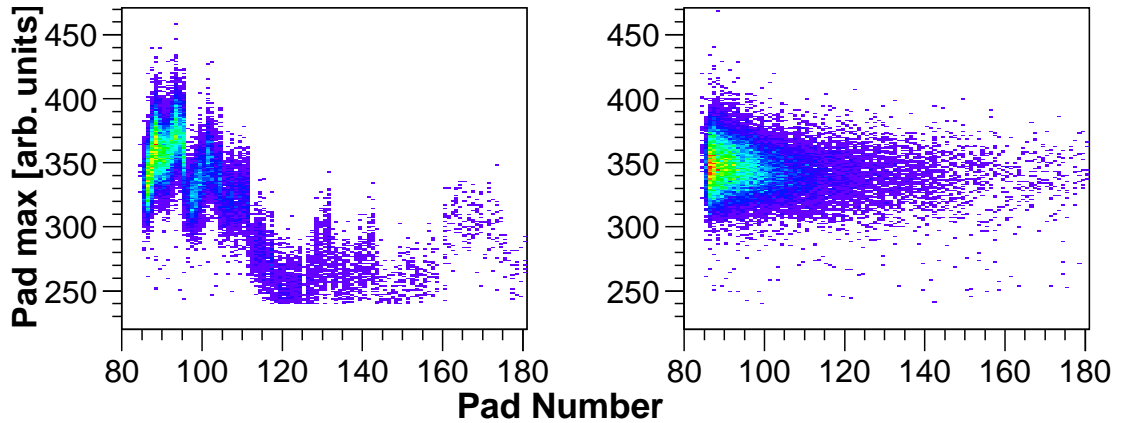


Figure 4.4: CRDC pad spectrum gated on outgoing ^{70}Se recoils, showing the signal amplitude (pad max) of each of the CRDC pads that fired. Shown are the pad amplitudes before calibration (left) and after calibration to an arbitrary pad max value (right).

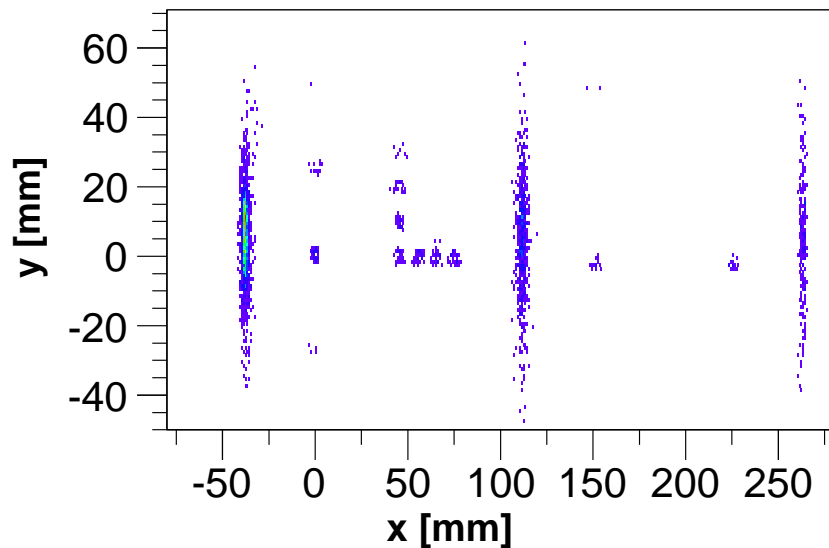


Figure 4.5: Calibrated CRDC mask spectrum. Recoils passing through a mask perforated with holes create a CRDC position map. This spectrum is compared to a map of known hole positions, and the CRDC gains/offsets are adjusted until agreement is seen.

for all values of $x < x_0$, where p is a correction parameter. The correction is performed via an iterative procedure. A software cut is made on an incoming secondary beam and on all resulting $N = Z$ recoils. The distributions are aligned so they appear at a constant arbitrary ion chamber energy for all x .

The ionisation chamber's sixteen sections also need to be calibrated relative to each other. A pre-written program was used to do this by making software cuts placed on two outgoing recoils provided by the user. Each channel and distribution histogram was then fitted with a Gaussian function, and the calibration parameters that align the individual chambers to each other in energy were output to a text file. No absolute calibration of the channels is possible, so all channels are calibrated relative to some arbitrary channel in much the same way as the time-of-flight drifts.

4.2.4 SeGA Corrections And Calibrations

Timing, Energy And Position Corrections

The times measured by the individual SeGA cores are not aligned with respect to each other or to the time measured by the OBJ scintillator. The raw SeGA time histograms are calibrated to a common arbitrary set point using a pre-written program.

In order for the γ spectra to display meaningful energies the core energies need to be calibrated. This is typically done using ^{152}Eu and ^{226}Ra source runs. Photopeaks recorded in individual cores are calibrated to correct energies using known literature values [80]. A simple first-order correction is sufficient to calibrate the core energies.

Segment energies contain information that is essential for accurate reconstruction of the point of γ -ray interaction, so it is crucial that the measured energies of the crystal segments are calibrated to that of the central contact (core). The calibration is performed on multiplicity = 1 events only, i.e., events where the full energy of the incoming γ ray is deposited in a single segment.

Information on the positions of the SeGA detectors was obtained using a laser position measurement system [75], which had co-ordinates transferred from the standard

NSCL co-ordinate system [76]. The S800 pivot-point position was chosen as the origin of this co-ordinate system. Given the measured vector positions of the front faces of each of the fifteen SeGA detectors, and given the known dimensions of the individual crystals (see Fig. 3.4), the vector positions of each of the SeGA detector segments relative to the origin at the target position were deduced.

Efficiency Measurements

The experiment in this work relied on analysing photopeaks at different energies. When analysing RDDS data, the relative detector efficiencies at the laboratory energies of the two RDDS transition components ('fast' and 'slow') need to be considered. The photopeak efficiency depends on a number of factors, such as the solid angle coverage of the detectors, the photon energy, the presence of absorbing materials in the beam pipe and the plunger itself, and the intrinsic detection efficiency of the crystals. Performing an efficiency measurement with standard sources such as ^{152}Eu or ^{226}Ra provides a stringent test of a simulation software's ability to replicate the experimental efficiencies (see Section 4.4).

One of the sources used for efficiency measurements in this work was ^{152}Eu , which had a measured activity of 0.313 MBq on May 1st 1978. ^{152}Eu sources exhibit a range of γ rays from 122 keV to 1408 keV. The ^{152}Eu source was placed between the target and degrader foils in the TRIPLEX plunger in order to give indications of the effects of shadowing of the SeGA detectors by the foil, plunger housing and beam pipe materials. A ^{226}Ra source was also used.

It was only necessary to obtain a relative efficiency curve, not an absolute one (i.e., one that expresses efficiency in % as a function of γ -ray energy). A relative efficiency curve (shown in Fig. 4.6) was obtained by measuring the intensities of the photopeaks in the ^{152}Eu source run and dividing them by the probability of γ -ray emission per decay (information obtained from [80]).

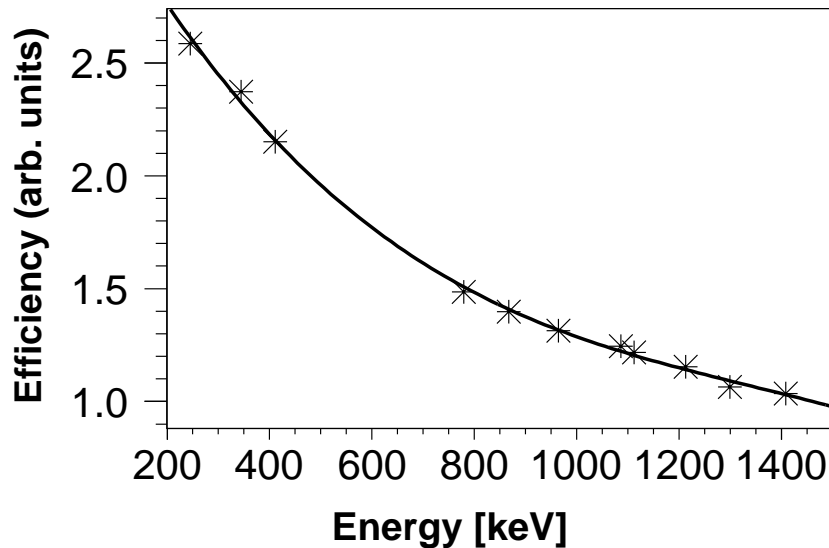


Figure 4.6: Experimental relative efficiency curve for 30° SeGA detectors recorded using a ^{152}Eu source. The relative efficiency curve can be compared to a simulated efficiency curve to check that the simulation software is accurately replicating experimental parameters (see Section 4.4 for more details).

4.3 Obtaining Recoil-gated γ -ray Spectra

4.3.1 Identifying Recoils

Secondary recoils emerging from the A1900 were identified using a time-of-flight technique between two plastic scintillators (see Fig. 4.7). Secondary beams are isolated with a software gate. Once a secondary beam is selected, individual recoils following reactions in the secondary target foil can be identified in the S800 spectrograph using an energy-loss vs. time-of-flight technique as shown in Fig. 4.8. Each recoil nucleus is selected with a software cut in the same way a secondary beam is selected, and the corresponding recoil-gated γ -ray spectrum can then be extracted.

4.3.2 β And Position Corrections

Accurate information on the position and energy of interacting photons in SeGA is essential for purposes of reconstruction. The relation between Doppler-shifted laboratory frame energy and rest energy is given by Equation 3.3. Fig. 4.9 shows

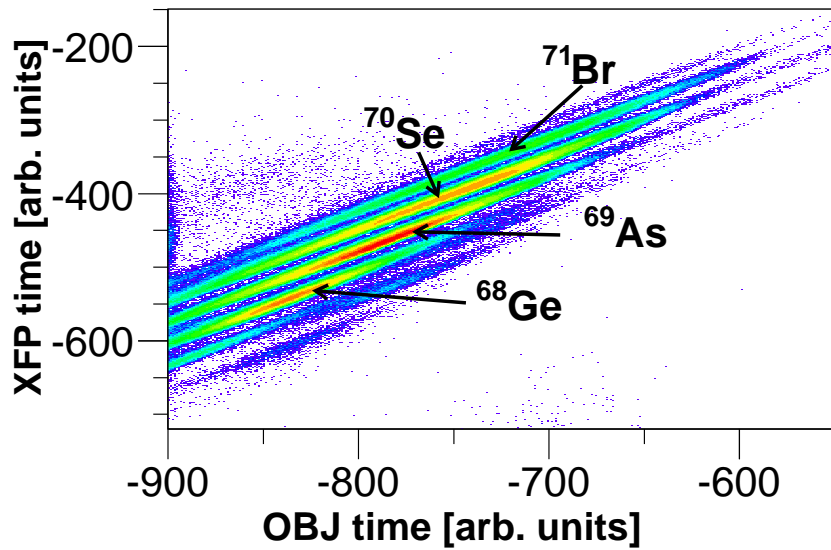


Figure 4.7: Plot showing recoil time recorded in the extended focal plane (XFP) scintillator vs. time recorded in the object (OBJ) scintillator. Both times are measured relative to the E1 scintillator at the end of the S800 focal plane. The different secondary beam components, which are clearly separated by this technique, are labelled. The z axis is logged.

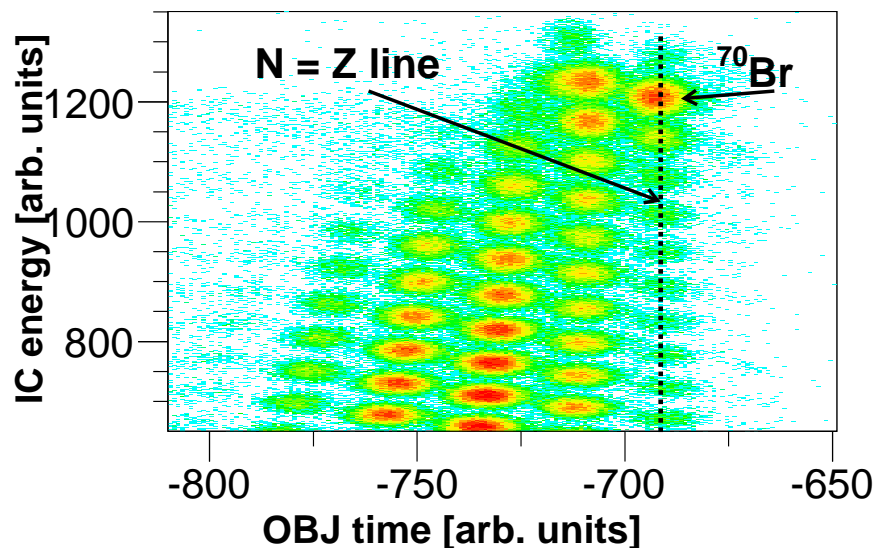


Figure 4.8: Particle identification (PID) plot gated on incoming ^{71}Br secondary beam. Recoils are separated into distributions based on their energy loss in the ion chamber (IC) and their time-of-flight from the OBJ scintillator. Shown are the $N = Z$ line (dashed line) and the ^{70}Br distribution. In these plots, a step to the right between distributions corresponds to neutron removal and a step down and to the left corresponds to proton removal. The z axis is logged.

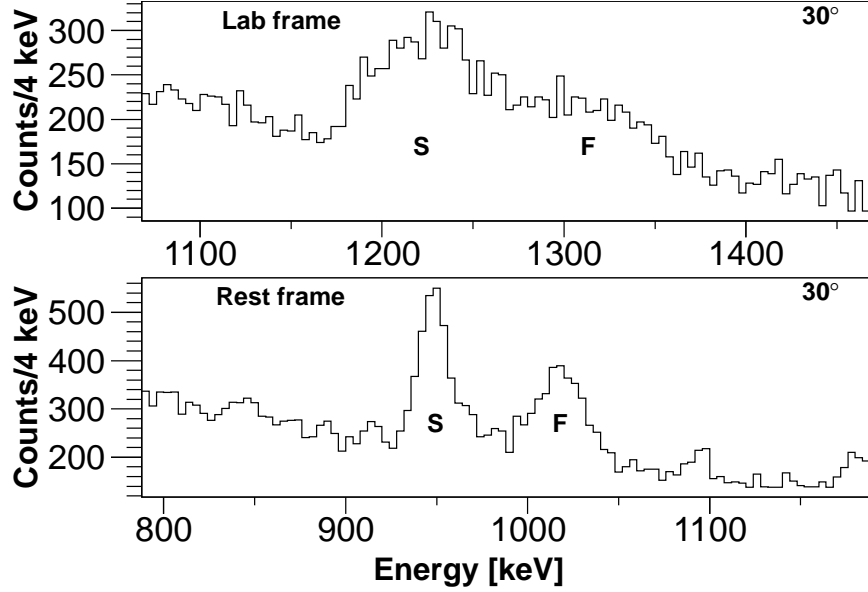


Figure 4.9: Comparison of recoil-gated γ -ray spectra recorded in the lab frame (top) and after Doppler correction to the recoil rest frame (bottom) for a detector angle of 30° . The γ spectra show the $^{70}\text{Se } 2_1^+ \rightarrow 0_{gs}^+$ transition recorded at a target-degrader separation of $275 \mu\text{m}$. The fast (F) and slow (S) peaks are labelled and correspond to decays before and after the degrader foil, respectively.

the result of the Doppler correction to the rest recoil frame.

The β (v/c) of the recoils was taken to be the velocity corresponding to the $B\rho$ setting of the S800 spectrograph dipole magnets. The z position of the target was not precisely at the origin of the SeGA position co-ordinate system. Without a correction to account for this, γ -ray energies recorded at both forward and backward angles would have a systematic error. This is corrected for in the SeGA settings file by adjusting the target z position parameter until the γ -ray centroids in the forward and backward SeGA rings line up to the correct energy.

The x and y positions of the reaction on the target foil were extracted by separating the SeGA detector rings into ‘top’ and ‘bottom’ detectors (i.e., detectors clustered at the top of the array and the bottom, respectively) or ‘left’ and ‘right’ detectors. γ spectra recorded from these two opposing halves of the SeGA ring were overlapped. The x and y values in the settings file were altered until the γ -ray peaks from the two halves of the SeGA ring overlapped at the correct energy.

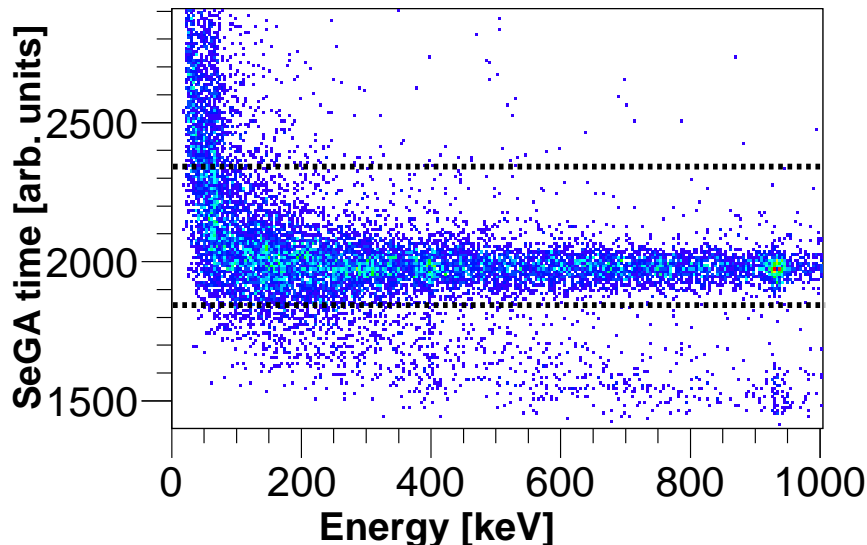


Figure 4.10: Spectrum of SeGA time vs. γ -ray energy gated on outgoing ^{70}Br recoils. Most events occur at a constant time (~ 1950 units) but low-energy (≤ 80 keV) γ rays are delayed by their longer collection time. SeGA timing gate positions used for the majority of this work are marked with dotted lines. Events with SeGA time ≤ 1800 are considered to be from a previous beam pulse.

4.3.3 SeGA Timing Gates

Each γ ray recorded in coincidence with a recoil in the S800 is given a timestamp by the electronics. This should be constant for γ rays emitted by a given nucleus regardless of the energy of the γ ray. However, in reality, low-energy γ rays (≤ 80 keV) have a tendency to interact only in the surface of the SeGA crystals and so, on average, the charge collection time for low-energy γ rays is longer than for high-energy (~ 1 MeV) γ rays. This effect is illustrated in Fig. 4.10. Timing gates are applied to SeGA events in order to remove the low-energy background and cut out γ events from the previous beam pulse that are erroneously tagged in coincidence with the current beam pulse. When analysing low-energy (≤ 100 keV) γ rays in this work the SeGA timing gates were adjusted to make sure no true events were removed.

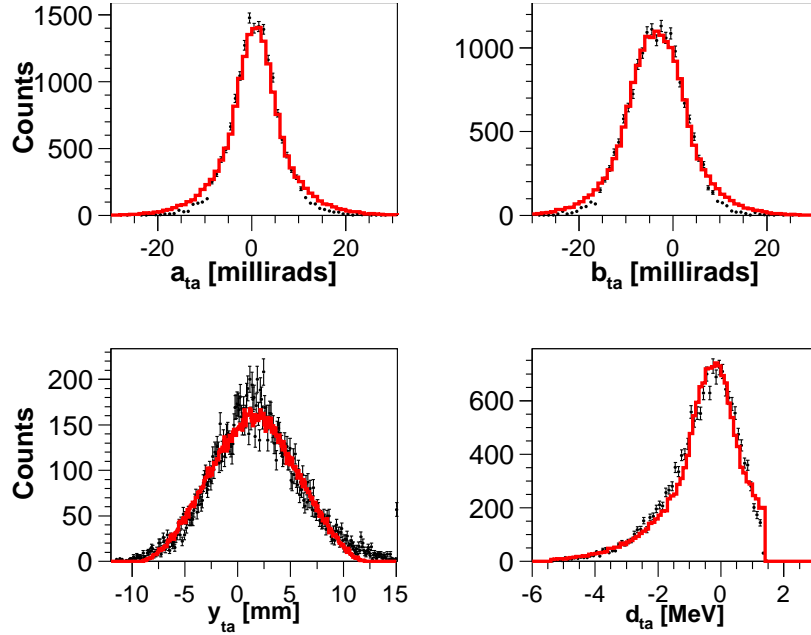


Figure 4.11: Experimental particle spectra for ^{70}Br recoils (black points) overlaid with simulated equivalents (red line) after parameter optimisation. The beam angular distribution is described by the a_{ta} and b_{ta} angles (top left and top right, respectively). The y_{ta} spectrum is shown bottom left and the energy spread relative to the centre of the S800 (d_{ta}) is shown bottom right.

4.4 Simulation Software

Lifetime results extracted in this work and presented in Chapter 5 were determined by matching a set of simulated γ spectra with various input lifetimes to experimental equivalents. The simulation package [10] is a Monte-Carlo software designed at NSCL specifically for lifetime analysis with the RDDS and γ -ray lineshape techniques, and is based on the GEANT4 framework [81]. The simulation code was developed from a previous simulation code described in Ref. [82]. The use of GEANT4 as a simulation tool for analyses of this type is discussed in Ref. [83].

The simulations are dependent on a number of parameters defined in the macro files. The simulation code is able to accurately replicate the characteristics of the incoming/outgoing beams, reaction kinematics, detector set-up and geometry, S800 acceptance and plunger foil characteristics. The parameters are acquired by fitting simulated particle spectra to their experimental equivalents (see Fig. 4.11) and varying parameters in the macro files until agreement is seen. The five main particle

spectra that are matched to extract the parameters are:

- a_{ta} and b_{ta} spectra, which give the angular beam spread in milliradians at the target position in the dispersive and non-dispersive planes, respectively.
- y_{ta} spectrum, which gives the beam position and width in mm at the target position in the non-dispersive plane.
- *betadist* spectrum, which gives the β distribution of the recoils in the focal plane.
- d_{ta} spectrum, which is related to the *betadist* spectrum and shows the energy spread of the recoils relative to the centre of the S800.

The simulation macros contain information on incoming secondary beam energy (extracted from a comparison of experimental/simulated particle spectra for runs containing no target foil in the beamline), outgoing recoil energy (taken from the S800 $B\rho$ with small adjustments made to correctly replicate the experimental β distribution) and the de-excitation γ rays emitted. Target and degrader foil thicknesses were measured by weight shortly before the experiment and incorporated into the simulations. It is necessary to correct for discrepancies in the GEANT4 stopping tables by adjusting the effective foil densities in the simulations. This is done by comparing the simulated unreacted beam *betadist* spectrum to the experimental equivalent.

Fig. 4.12 shows experimental a_{ta} spectra associated with different recoils before and after the degrader foil was installed in the plunger. As Fig. 4.12 demonstrates, there are in some cases pronounced peripheral ‘wings’ seen on either side of the Gaussian distributions. These wing distributions are seen in both a_{ta} and b_{ta} spectra. Recoils excited via inelastic excitation and single-nucleon knockout produce a_{ta} and b_{ta} spectra with wings that are relatively well pronounced, whereas multi-nucleon knockout reactions do not produce such strong wing features. It is also clear from Fig. 4.12 that these wing distributions only appear in the angle spectra for distance runs, i.e., when both a target and a degrader foil were present in the plunger. The most likely explanation for this is that particles are being strongly scattered in the degrader to relatively high angles, therefore the a_{ta} and b_{ta} spectra are in fact

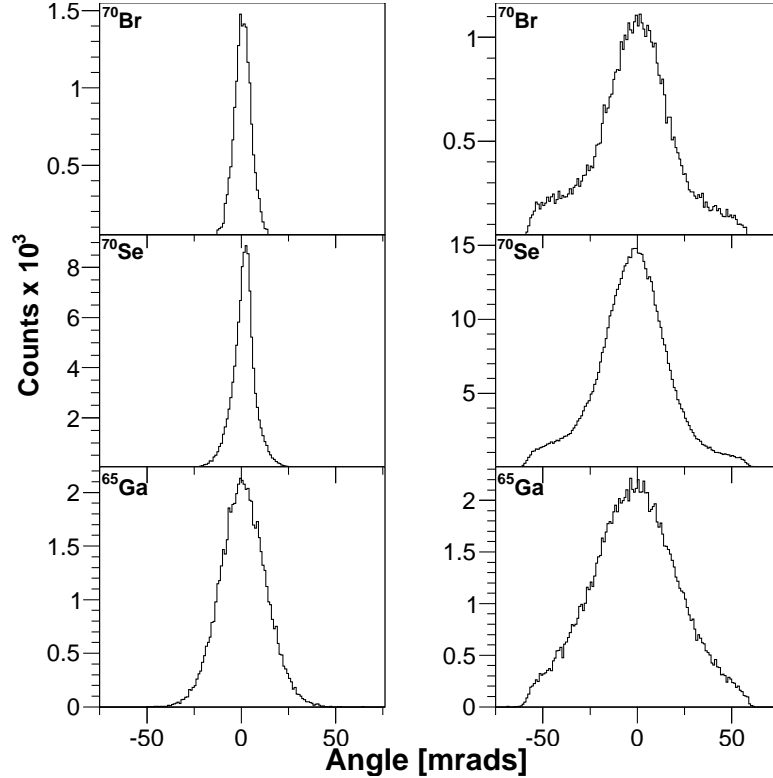


Figure 4.12: Experimental particle a_{ta} spectra showing recoil angular distributions in the dispersive plane. The left-hand column shows target-only data and the right-hand column shows data from the 275 μm distance runs. The top row shows distributions gated on ^{70}Br recoils created via one-neutron knockout of the ^{71}Br secondary beam, the second row is gated on ^{70}Se created via inelastic scattering and the bottom row is gated on ^{65}Ga created via multi-nucleon knockout of the ^{70}Se secondary beam. The presence of the degrader appears to be causing the ‘wing’ distributions to appear.

showing two convoluted Gaussians with different widths; a narrow distribution from the target foil and a wide one from the degrader foil.

The simulation package used in this work is not equipped to deal with two different Gaussian distributions, but nevertheless the effect of different angular distribution widths was investigated. It was found that large changes in the angular distribution widths had no noticeable effect on the widths, positions or intensities of the γ -ray peaks in the simulations. So, despite there not being a full explanation for the wing distributions, it was ignored in the analysis as it did not seem to affect the extracted results.

Analysis of the ^{70}Se recoil β distribution (see Fig. 4.13) showed that only the extreme

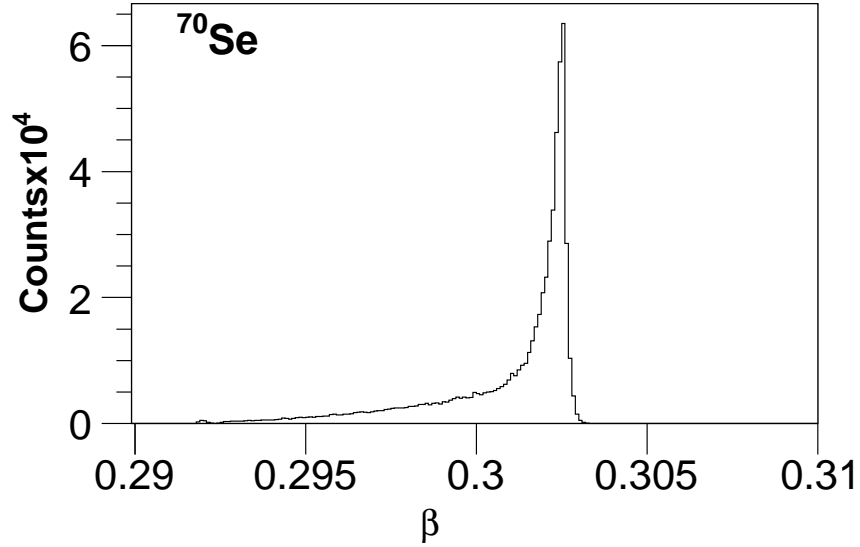


Figure 4.13: Experimental β distribution of ^{70}Se recoils for 275 μm data. The non-Gaussian nature of the distribution suggests that it is the extreme tail of a large distribution, the vast majority of which is not passing through to the focal plane of the S800.

tail of the distribution had been recorded. It was likely that a significant fraction of the ^{70}Se recoils fell outside the momentum acceptance window of the S800. The simulations can accurately replicate this experimental particle distribution, however this meant discarding the majority of the γ statistics generated by the simulation. Simulation files would need to create so many events that it would take weeks to generate a single simulated γ spectrum with appreciable statistics, which is impractical. It was found that, as long as the momentum window was accurately defined, changing the width of the recoil distribution made no appreciable difference to the γ peak widths, positions or intensities - see Fig. 4.14. Note that in Fig. 4.14 ^{70}Br simulations are used to illustrate the point, as they required running for a much shorter time than ^{70}Se simulations. Since the distribution width in the simulations made no observable difference to the γ peak lineshapes it was set to an arbitrarily large value for the case of ^{70}Se . This brought more recoil events into the momentum window without compromising the validity of the simulations. Only when simulating ^{70}Se was this alteration necessary.

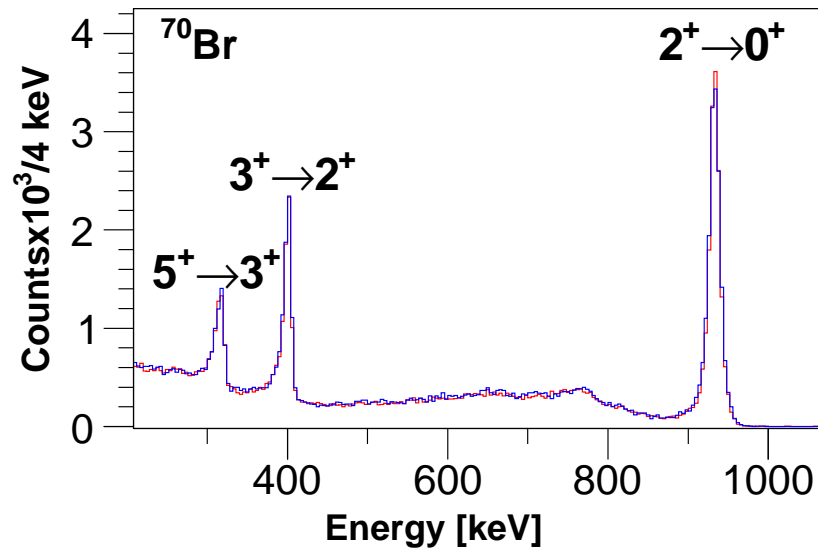


Figure 4.14: Simulated γ spectra for ^{70}Br target-only data. The blue spectrum was generated assuming a recoil particle distribution double the width of the red spectrum. The blue spectrum has been scaled to the red spectrum. The γ peak widths are insensitive to the recoil distribution width.

4.5 Histogram Manipulation With ROOT

4.5.1 Background Approximations

Bremsstrahlung, random γ -particle coincidences and Compton backgrounds all contribute to the γ background. In the simulated spectra the peak-to-background ratio is much larger than in the experimental spectra, so an additional background contribution is incorporated. It was only important to have a correct background around the area of lifetime sensitivity. This allowed a simple linear background to be used in most cases. In a select few cases a second-order polynomial or exponential was necessary to accurately replicate the experimental background. Background additions were determined for each spectrum on a case-by-case basis. An example of a linear background added to a γ spectrum is shown in Fig. 4.15.

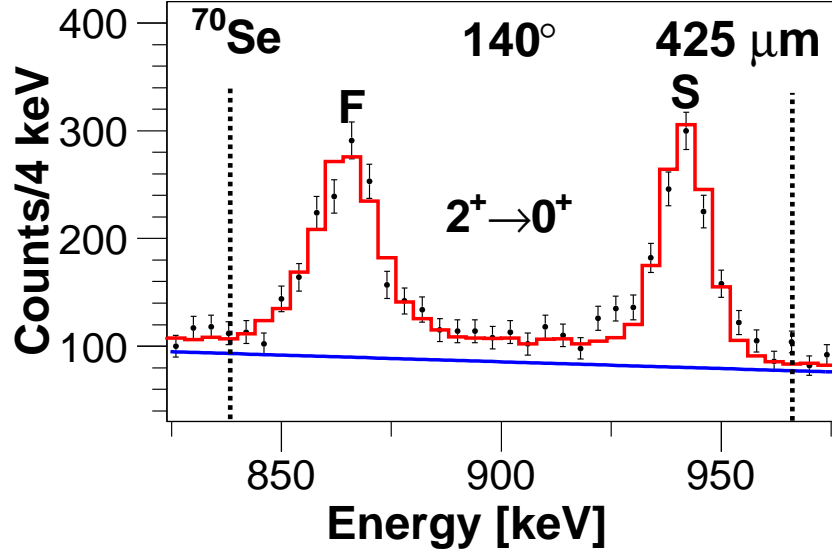


Figure 4.15: Experimental γ spectrum for the $2_1^+ \rightarrow 0_{gs}^+$ transition in ^{70}Se (black points) with simulated best-fit lineshape (red line) and linear background (blue line). Dotted lines denote the limits of lifetime sensitivity assumed in the fit. Fast (F) and slow (S) peaks are labelled and correspond to decays before and after the degrader foil, respectively. Data shown are for a target-degrader distance of $425 \mu\text{m}$ for backward SeGA detector angles only.

4.5.2 The Lifetime Suite

A dedicated suite of .C programs was created specifically for this work by the author. The *Lifetime Suite* collection of codes uses similar methods to extract not only level lifetimes but also degrader excitation values (see Section 4.6) and γ -ray feeding intensities (see Section 5.1). The basic premise of the codes is to overlay experimental and simulated γ -ray spectra (with additional linear background) and extract the χ^2 fit over a sensitive bin range. The χ^2 value was calculated over a range of bins i using the relation

$$\chi^2 = \sum_{i=\min}^{\max} \frac{(y_i - s_i)^2}{\sigma_i^2} \quad (4.3)$$

where y_i and s_i are the bin content (in counts N) for the experimental and simulated spectra, respectively, and σ_i is the statistical error given by the square root of the experimental bin counts. The simulation files were generated with a large number of counts and scaled down to the experimental spectra, and thus the statistical error

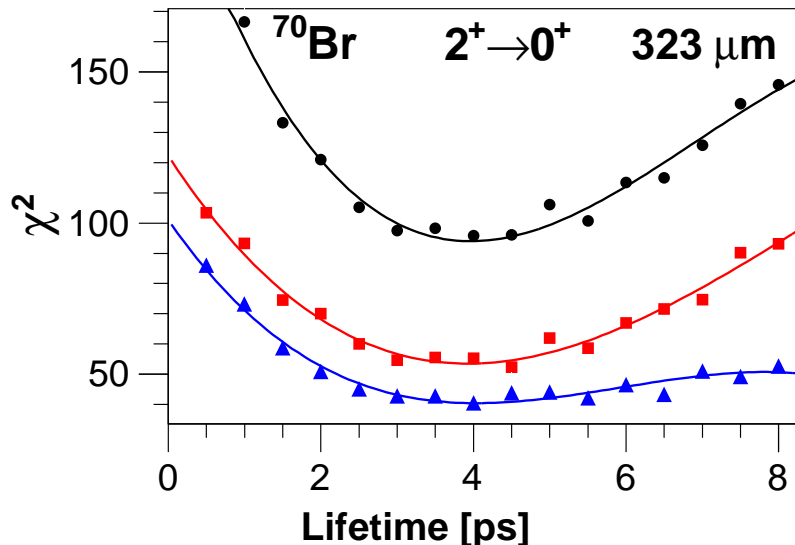


Figure 4.16: χ^2 minimisation for the 2_1^+ state lifetime in ^{70}Br using $323\ \mu\text{m}$ data. Shown are data for 30° (red squares), 140° (blue triangles) and both SeGA rings added together (black circles). The cubic polynomial fits to the 30° (red line) and 140° (blue line) data are shown. The fit to the added spectrum (black line) gives the measured lifetime of the state (in this case, 3.96 ps) and the $\chi_{min}^2 \pm 1$ value gives the error (in this case, ± 0.42 ps).

on the simulation bin contents was assumed to be negligible. The region of lifetime sensitivity is shown by the dotted lines in Fig. 4.15. Only bin contents between the two dotted lines were included in the fit.

Once a χ^2 fit for each simulation file was made, the results were plotted against lifetime value and fit with a third order polynomial as shown in Fig. 4.16. The lifetime result extracted is given by the τ value corresponding to χ_{min}^2 , and the errors are taken as the τ values at $\chi_{min}^2 \pm 1$. The χ^2 analysis is performed for the two SeGA rings separately, with the χ^2 plots then added together and the value with errors read off - see Fig. 4.16. Fig. 4.16 shows that the χ^2 fit to backward SeGA ring data (blue line) is less sensitive on the high-lifetime side compared to the forward ring data (red line). This is a common feature in the analysis that was also noticed by P. Voss during his thesis work [82]. The weaker high-lifetime sensitivity for backward SeGA ring data is possibly a geometric issue; longer-lived states will decay further away from the backward ring detectors than shorter-lived states, and so γ -ray lineshape effects recorded in these detectors will be less sensitive to changes in lifetime. Despite the weaker sensitivity in backward ring data, the lifetimes extracted from both rings agree with each other within error.

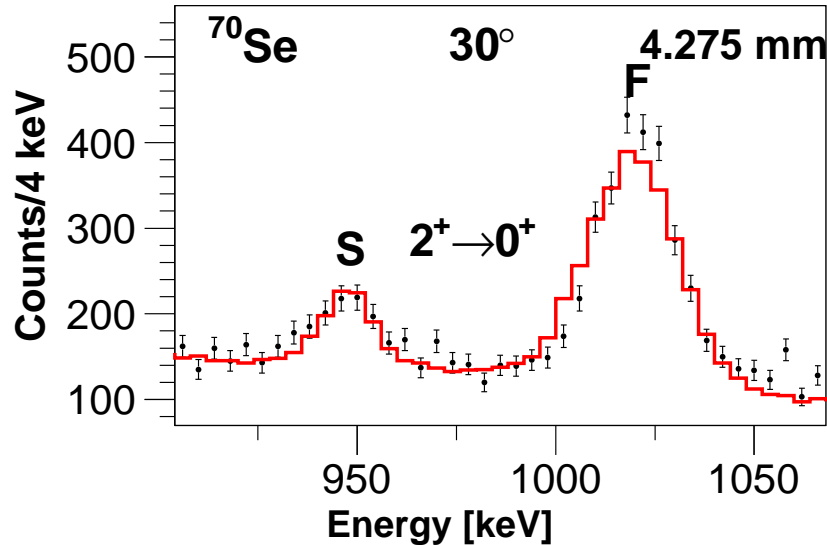


Figure 4.17: Experimental large-distance (4.275 mm) spectrum for ^{70}Se (black points) and best-fit simulated lineshape (red line). Fits like this to large-distance data allowed for the extraction of degrader excitation contributions.

A full list of the codes in the *Lifetime Suite* is given below. An example lifetime code has been added as an appendix (see Appendix A). All codes are basically identical in their function.

- *Feeding Calculator* - calculates intensities of feeding transitions.
- *Degex Calculator* - calculates degrader excitation values.
- *Lifetime Calculator* - calculates excited state lifetimes.

4.6 Determination Of Degradation Excitation Contributions

In RDDS experiments nuclei are produced and excited in a target foil and slowed in a degrader foil placed downstream. The ratio of the γ peak intensities at various target-degrader separations gives the lifetime of the state. It is important, once peak intensities have been extracted, to remove contributions from degrader excitation. This phenomenon occurs when excited nuclei are produced not in the target foil

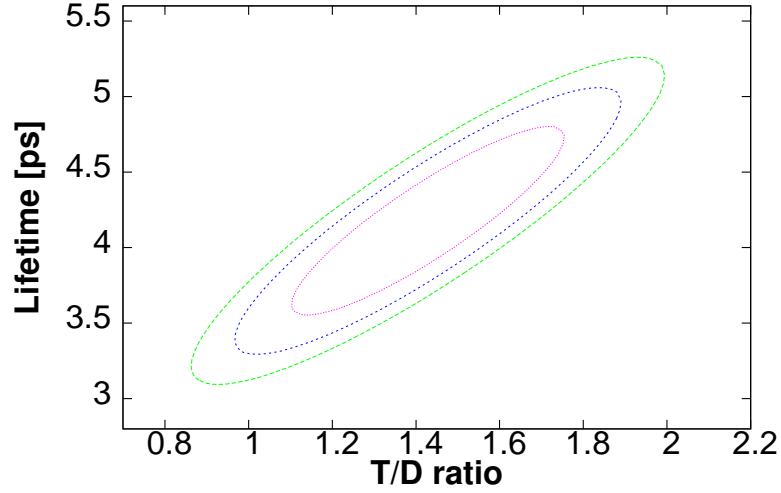


Figure 4.18: 2D χ^2 surface used to determine the degrader excitation contribution for ^{70}Br , using fits to the $2_1^+ \rightarrow 0_{gs}^+$ transition for all distances. Shown are the χ^2+1 (pink), χ^2+2 (blue) and χ^2+3 (green) ovals. The value and errors of the degrader contribution were determined by projecting the χ^2 minimum and χ^2+1 ellipse, respectively, onto the Degradation Value axis.

but in the degrader foil. The contribution from degrader excitation is measured by taking γ data at a large target-degrader separation (in this case, 4.275 mm). At this large separation all recoils created in the target would have decayed to their respective ground states and thus any intensity seen in the ‘slow’ RDDS γ peak is entirely due to excitations in the degrader foil. Since this contribution is constant irrespective of distance between the foils, this effect can be subtracted from data taken at other target-degrader distances.

The simulation package has a degrader excitation parameter that specifies the degrader excitation contribution. The ratios are extracted via a fit of simulations of varying degrader excitation value to the large-distance (4.275 mm) data (e.g., see Fig. 4.17). The values extracted in this work are given in Table 4.2.

It was not possible to extract the degrader excitation contribution for ^{70}Br from the large-distance data because of the delaying effect of the long-lived 5_1^+ and 3_1^+ feeding states. The contribution was instead extracted using a 2D χ^2 fit, similar to the technique used to extract degrader excitation values in P. Voss’ thesis [82]. Simulations with varying lifetime and degrader excitation value were fit to the experimental spectra at all distances. A bivariate quadratic was then fit to the 2D χ^2

Table 4.2: Degradation excitation contributions for recoils studied in this work.

Nucleus	Degradation Excitation Value
^{62}Zn	3.58(32)
^{70}Br	1.43(32)
^{68}Se	1.14(28)
^{72}Kr	1.38(36)
^{70}Se	3.41(19)
^{66}Ge	2.45(22)
^{69}Se	1.43(32)
^{65}Ga	1.36(9)

Table 4.3: Total run times of the target-only data and the four target-degradation distance data runs.

Run type	Total time [hours]
Target-only	8.1
275 μm	27.9
323 μm	18.2
425 μm	20.1
4.275 mm	18.7

surface and the degradation excitation value, with error, was extracted via a projection of the χ^2 minimum and the χ_{min}^2+1 ellipse onto the ‘degradation value’ axis (see Fig. 4.18).

4.7 Absolute Foil Distance Determination

Data were taken at four target-degradation separations in this experiment; these distances were 275 μm , 323 μm , 425 μm and 4.275 mm. Data were taken for each distance run over approximately a 24 hour period, whereas the target-only data (taken to analyse excited state populations - see Section 5.1) were taken over approximately 8 hours. The run lengths are given in Table 4.3.

The relative distance between the target and degradation foil faces was measured and

4.7. ABSOLUTE FOIL DISTANCE DETERMINATION

maintained using capacitance measurements [67], where a potential difference was applied to the foil faces. Since all the capacitance-dependent conditions except the distance between the foils is held constant, the capacitance measured is inversely proportional to the foil separation.

In an ideal set-up with perfectly straight parallel foils, one could decrease the foil separation down to below $1\ \mu\text{m}$ without the foils coming into contact. In this scenario, a separation of $0\ \mu\text{m}$ would be exactly the point at which the foils touched. However, due to non-ideal effects, such as material imperfections/distortions and imprecise foil alignment, the foils come into physical contact before reaching $0\ \mu\text{m}$. A zero-offset is therefore applied to the relative distances to obtain the absolute inter-foil distances mentioned above.

The foils are first aligned so their surfaces are exactly parallel to each other. This is usually done by eye; the screws that hold the target frame in place are adjusted until the foils appear parallel. Once a satisfactory alignment has been performed, the distance calibration is made. Typically a capacitance measurement is used to obtain the zero-offset value. Plotting the reciprocal capacitance against distance should show a linear relationship for most distances. However, at small distances impurities on the foil surface (such as particles of dust) and misalignments cause the measurements to depart from linear behaviour. Extrapolating from the linear part of the graph to zero gives the zero-offset distance. The true foil separation is then given as [relative distance given by control system] - [zero-offset]. Zero-offsets of a few tens of microns are common [67].

In this experiment the foils were not perfectly flat once glued onto the frame. Distortion of the foils at the corners during mounting resulted in them not coming closer than $200\text{-}300\ \mu\text{m}$ at closest separation, with a visible gap remaining between the foil faces (see Fig. 4.19). This resulted in a failure of the inverse capacitance method to obtain the absolute separation (see Fig. 4.20). It was necessary for a different method to be used to obtain the zero-offset.

In this work the zero-offset was determined by measuring the lifetime of a well-known excited state. The lifetime of the first 2^+ state in ^{62}Zn , with a literature value of $4.23(20)$ ps based on a weighted average of several studies [84], was used as this nucleus was populated strongly in the data from the ^{70}Se secondary beam. Simulations were made assuming a range of zero-offset values. In each case effective feeding

4.7. ABSOLUTE FOIL DISTANCE DETERMINATION

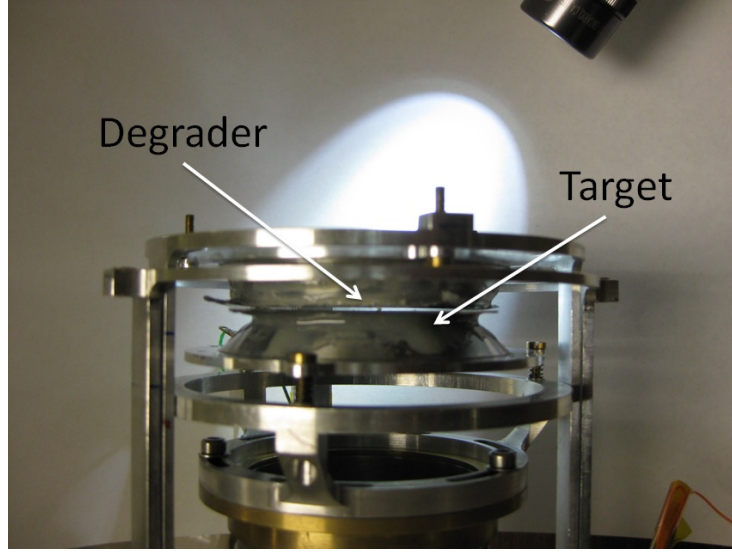


Figure 4.19: Photograph taken during tests of the foil separation. In this picture the foils have been moved together until electrical contact between the frames is achieved. The target and degrader foils are marked on the figure. A significant gap is visible between the centres of the two foil faces.

Table 4.4: ^{62}Zn 2_1^+ state lifetime assuming different zero-offset distances. Effective feeding state lifetimes are taken into account. Only statistical errors are quoted (whereas the literature (Lit.) result contains both statistical and systematic effects).

Nucleus	τ [ps]	τ [ps]	τ [ps]	τ [ps]	τ [ps]
Zero-offset	50 μm	100 μm	180 μm	275 μm	Lit.
^{62}Zn	2.85 ± 0.13	3.15 ± 0.15	3.66 ± 0.17	4.25 ± 0.20	$4.23 \pm 0.20^\dagger$

† from [84].

state lifetimes were extracted and then the lifetime of the 2_1^+ state was determined. Repeating for many assumed zero-offsets established a linear relationship between zero-offset and 2_1^+ state lifetime (see Table 4.4). The correct zero-offset is the value that returns the literature 2_1^+ lifetime value after corrections for feeding. Using this technique the zero-offset was deduced to be 275(30) μm . Therefore, the absolute foil separations in this work were determined to be 275 μm , 323 μm , 425 μm and 4.275 mm (using relative-distance capacitance measurements, which did not suffer from the problems of the zero-offset capacitance measurement). Table 4.4 shows the ^{62}Zn 2_1^+ state lifetime measured in this work assuming different foil separation zero-offset values.

Post-experiment tests were performed at Köln in an attempt to verify the 275 μm

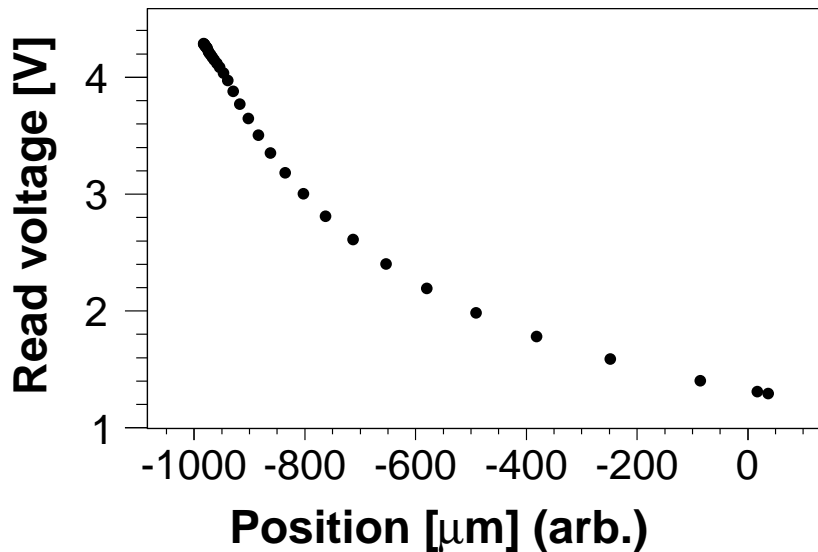


Figure 4.20: Plot showing read voltage as a function of motor position. The foils become closer as the motor position becomes more negative. When the foils get very close (motor position of about $-980 \mu\text{m}$) the readings should tend to infinity. The inverse of this graph is then extrapolated to zero to get the zero-offset distance. The zero-offset capacitance measurements in this work showed a non-conventional behaviour at close distances caused by foil distortion (the readings do not tend to infinity). The capacitance method therefore could not be used to obtain the zero-offset value.

zero-offset extracted from the lifetime measurement. The tests involved sliding papers of a known thickness between the two foils and decreasing the distance between them manually until contact was seen. Laser measurements were also used to ascertain a precise separation at closest distance. The results of these tests concluded that the *minimum* possible zero-offset was $200(20) \mu\text{m}$ [85].

4.8 Origin Of Systematic Errors

Results in this work are quoted in Chapter 5 with separate errors arising from statistical and systematic effects. Statistical errors naturally arise from the level of statistics available for the measurements. Many factors could contribute to a systematic error on a measurement, and it is therefore important that the largest contributors are identified and investigated. In the case of lifetime results in this work extracted via the RDDS technique, it was discovered that the largest contributions

4.8. ORIGIN OF SYSTEMATIC ERRORS

of systematic error were feeding state lifetime, feeding intensity, degrader excitation contribution and target-degrader separation uncertainties. For RDDS analysis the systematic uncertainties contributed between 5-10% to the total lifetime errors. For longer lifetimes (on the order of hundreds of picoseconds) the systematic effects due to degrader excitation and target-degrader separation became negligible. The most significant systematic errors for longer lifetimes came from the uncertainty on γ -ray feeding intensities and feeding state lifetimes, however these uncertainties contributed less than 2% to the total error.

Each of these systematic error contributions was investigated separately using simulations. The lifetime of the depopulating transition was measured with each contributing parameter set to one standard deviation away from its measured value in the simulation macro. The significant systematic errors were added in quadrature to obtain a final systematic error on the measurement, which was in turn added in quadrature with the statistical error to obtain a total error.

Chapter 5

Results

This chapter is split into two sections. In the first section the γ -ray spectroscopy of the recoils studied in this work will be presented with feeding histories and, where applicable, previously unobserved transitions stated. In the second section the lifetimes of excited states in several recoil ion species will be presented, along with feeding state effective lifetimes where possible.

5.1 Gamma Spectroscopy Results

Before the degrader foil was inserted into the plunger a short (~ 8 hour) run was performed with just the target foil present in TRIPLEX in order to extract excited state populations. This was necessary since extracting lifetimes of excited states in nuclei relies on an accurate knowledge of excited state population intensities. Also, since this was the first time that nuclei in this region were populated via nucleon knockout it was expected that previously unobserved excited states may be populated in some of the recoils.

All γ rays observed in the target-only spectra were also visible in the distance spectra (from the runs with both a target and a degrader in place). There was no evidence for any γ rays in the distance spectra that were not also visible in the target-only spectra. The only exception to this was the $5_1^+ \rightarrow 3_1^+$ transition in ^{70}Br , which was weak and therefore did not appear above background in the target-only spectrum.

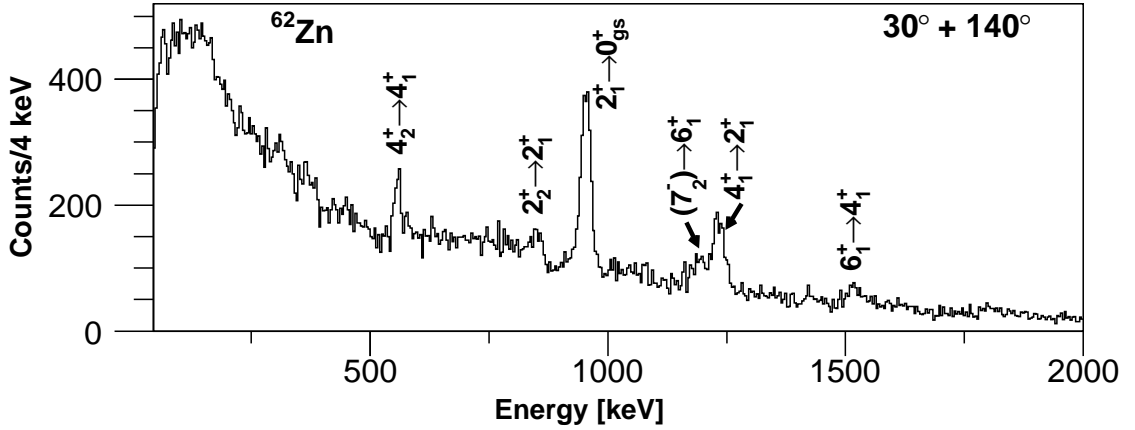


Figure 5.1: γ spectrum from gating target-only data on ^{62}Zn recoils. The observed transitions are labelled and listed in Table 5.1.

It was, however, clearly visible in the distance spectra, which had higher levels of statistics due to the longer run times (see Table 4.3).

It was assumed in the lifetime analysis section (Section 5.2) that, once all feeding contributions to a state were identified, any remaining intensity is either due to direct population of the state in question or due to unseen side-feeding from states with relatively fast lifetimes, i.e., lifetimes that are at least an order of magnitude faster than the lifetime of the state of interest.

5.1.1 ^{62}Zn

Excited states in ^{62}Zn were populated via multiple-neutron knockout of the ^{70}Se secondary beam in the target foil. The recoils passed into the S800 with an average energy of 77.1 AMeV. Gating target-only data on ^{62}Zn recoils as described in Section 4.3 produced the γ spectrum shown in Fig. 5.1. The observed transitions are listed in Table 5.1. The 2_1^+ state was observed to be fed by two γ rays. The strongest of these was the 1232 keV $4_1^+ \rightarrow 2_1^+$ transition, which feeds the 2_1^+ state with an intensity of 65(3)% relative to the $2_1^+ \rightarrow 0_{gs}^+$ transition. The 4_1^+ state is in turn fed by γ rays from the known 6_1^+ and 4_2^+ states. The second feeding γ ray to the 2_1^+ state was the 851 keV $2_2^+ \rightarrow 2_1^+$ transition, which feeds with a 14(2)% relative intensity.

There is potentially a small intensity $4_2^+ \rightarrow 2_2^+$ transition feeding the non-yrast 2_2^+

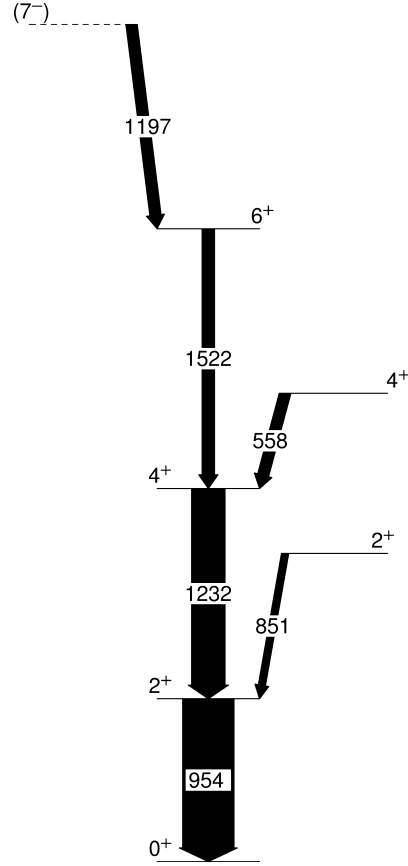


Figure 5.2: Partial level scheme for ^{62}Zn identifying the excited states populated in this work. Arrow thickness corresponds to relative intensity of transition. Tentatively assigned spin-parities in the literature are in parentheses with a dashed level. See Table 5.1 for more details.

Table 5.1: Transitions identified in ^{62}Zn from target-only data (see Fig. 5.1). Shown are present (Pres.) and literature (Lit.) transition energies E_γ , measured intensities I_γ (where the $2_1^+ \rightarrow 0_{gs}^+$ intensity is set to 100), initial/final level energies/spin-parities and literature state mean lifetimes τ_m .

E_γ Pres. [keV]	E_γ Lit. ♣ [keV]	I_γ	E_i [keV]	J_i^π	E_f [keV]	J_f^π	τ_m Lit. [ps]
558.1(8)	557.5(2)	22(3)	2744	4_2^+	2186	4_1^+	3.4(3)‡
849(2)	850.8(1)	14(2)	1805	2_2^+	954	2_1^+	3.8(6)‡
953.5(4)	953.8(1)	100	954	2_1^+	0.0	0_{gs}^+	4.23(20)†
1192(3)	1196.9(5)	27(5)	4905	(7^-)	3708	6_1^+	12(5)‡
1233(1)	1232.2(1)	65(3)	2186	4_1^+	954	2_1^+	0.76(27)‡
1520(3)	1521.5(3)	24(3)	3708	6_1^+	2186	4_1^+	0.36(5)‡

♣ from [86]; † from weighted average [84]; ‡ from [87].

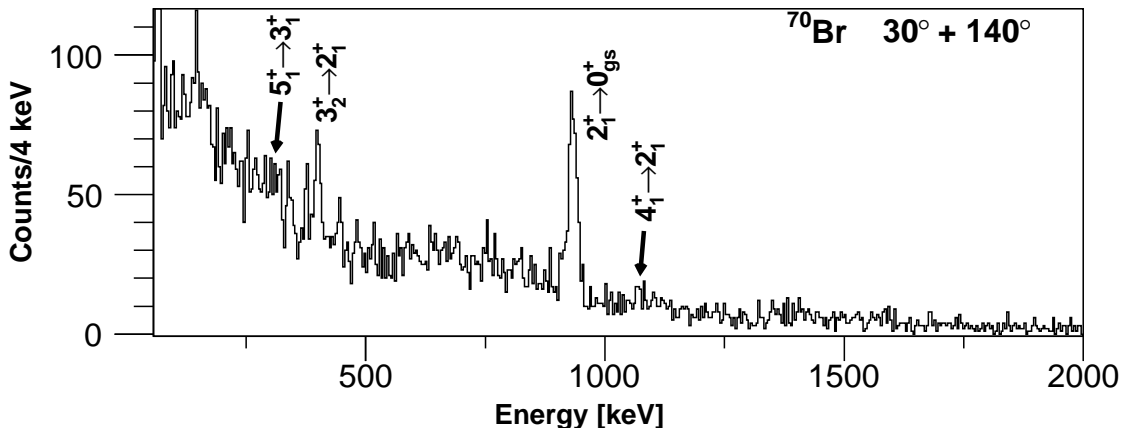


Figure 5.3: γ spectrum from gating target-only data on ^{70}Br recoils. Transitions are labelled and listed in Table 5.2. The known $4_1^+ \rightarrow 2_1^+$ transition is not observed with any significant intensity. Also shown is the position of the $5_1^+ \rightarrow 3_1^+$ transition at 321 keV, which did not appear above background in the target-only spectrum but was nevertheless present (see Fig. 5.4).

state at an energy of 939 keV, since the $4_2^+ \rightarrow 4_1^+$ transition is also seen. This would appear on the left of the 954 keV $2_1^+ \rightarrow 0_{gs}^+$ transition and would be easy to discern by an unnatural width of, or tailing to, the 954 keV γ ray. Examination of the target-only γ -ray spectrum showed no conclusive evidence of this transition, meaning that the transition is weak. By comparing the experimental γ spectrum to simulations using varying $4_2^+ \rightarrow 2_2^+$ transition intensity, it was determined that the transition had to be less than 4% of the $2_1^+ \rightarrow 0_{gs}^+$ transition intensity, else it would be clearly visible.

5.1.2 ^{70}Br

Excited states in the odd-odd $N = Z$ nucleus ^{70}Br were populated via single-neutron knockout from the ^{71}Br secondary beam. The ^{70}Br recoils, created for the first time using this reaction, entered the S800 with an energy of 82.2 AMeV. The $B\rho$ settings of the S800 were tuned to accept recoils generated via the single-neutron knockout reaction so the ^{70}Br recoils were centred in the S800. Gating target-only data on ^{70}Br recoils produced the γ spectrum shown in Fig. 5.3. The observed transitions are listed in Table 5.2. In this work, the $\mathbf{T} = 1$ 2_1^+ state in ^{70}Br is fed by the 403 keV $3_1^+ \rightarrow 2_1^+$ transition with an intensity of 23.6(26)% relative to the $2_1^+ \rightarrow 0_{gs}^+$ decay. The $\mathbf{T} = 0$ 3_1^+ state is in turn fed by the 321 keV γ ray from the known $\mathbf{T} = 0$ 5_1^+ state, with an intensity of 50.5(48)% relative to the $3_1^+ \rightarrow 2_1^+$ decay

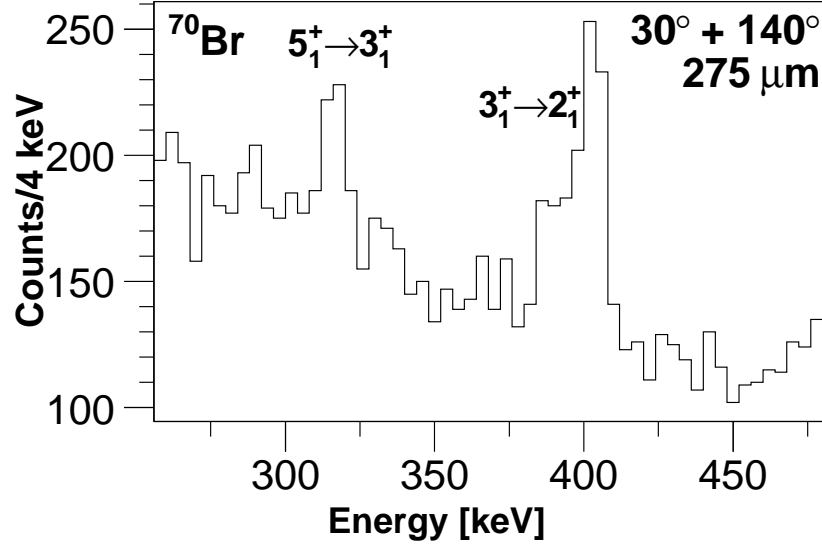


Figure 5.4: γ spectrum from gating 275 μm data on ^{70}Br recoils. Transitions are labelled and listed in Table 5.2. The 321 keV peak corresponding to the $5_1^+ \rightarrow 3_1^+$ transition in ^{70}Br was only clearly identifiable in distance spectra.

(11.9(17)% relative to the $2_1^+ \rightarrow 0_{gs}^+$ decay). The 321 keV transition could not be seen above the γ background in the target-only spectrum due to insufficient statistics. However, owing to the higher statistics in the distance spectra it was possible to measure the $5_1^+ \rightarrow 3_1^+$ transition intensity using distance data - see Fig. 5.4. The energy centroid of the $5_1^+ \rightarrow 3_1^+$ transition was observed to be ~ 5 keV lower than the literature value [12]. This can be understood if the lifetime of the 5_1^+ state is long (hundreds of picoseconds); the recoils decay a significant distance downstream of the target position and therefore the Doppler correction (which assumes decay at the target position) gives an incorrect γ energy. The $4_1^+ \rightarrow 2_1^+$ transition, at an energy of 1069 keV, is not seen with any statistical significance in either the target-only γ spectrum (8 hours data collecting) or any of the distance spectra (85 hours total data collecting). An upper limit to the intensity of the 1069 keV γ ray was obtained by comparing experimental γ spectra to simulated equivalents with a range of $4_1^+ \rightarrow 2_1^+$ transition intensities. It was determined that the $4_1^+ \rightarrow 2_1^+$ transition could be no larger than $\sim 5\%$ of the $2_1^+ \rightarrow 0_{gs}^+$ intensity.

A secondary aim of the experiment was the observation the $1_1^+ \rightarrow 0_{gs}^+$ transition in ^{70}Br , as ^{70}Br is the first odd-odd *fpg*-shell nucleus beyond ^{58}Cu where this state has not been identified. Predictions with large-scale shell model calculations [2] suggest that it should lie just below the 2_1^+ state, however the spectrum in Fig. 5.3 shows

Table 5.2: Transitions identified in ^{70}Br (see Figs. 5.3 and 5.4). Shown are present (Pres.) and literature (Lit.) transition energies E_γ , measured intensities I_γ (where the $2_1^+ \rightarrow 0_{gs}^+$ intensity is set to 100) and initial/final level energies/spin-parities.

E_γ Pres.	E_γ Lit.♣	I_γ	E_i	J_i^π	E_f	J_f^π
[keV]	[keV]		[keV]		[keV]	
316(1)	320.7(3)	11.9(17)	1657	5_1^+	1336	3_1^+
400(1)	402.6(3)	23.6(26)	1336	3_1^+	934	2_1^+
932.9(6)	933.6(3)	100	934	2_1^+	0.0	0_{gs}^+
-	1068.8(3)	≤ 5	2002	4_1^+	934	2_1^+

♣ from [12].

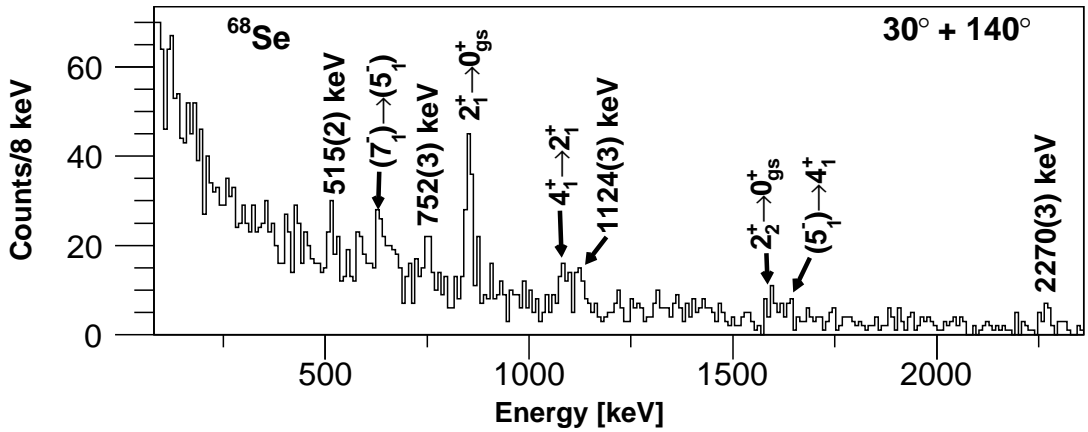


Figure 5.5: γ spectrum from gating target-only data on ^{68}Se recoils. The observed transitions are labelled. γ transitions marked with their energies are new. See Table 5.3 for details.

no evidence of its presence.

5.1.3 ^{68}Se

Excited states in ^{68}Se were populated via two-neutron knockout from the ^{70}Se secondary beam. The recoils left the target at an energy of 82.2 AMeV. Gating target-only data on the ^{68}Se recoils produced the γ spectrum shown in Fig. 5.5. A partial level scheme for ^{68}Se is shown in Fig. 5.6. The labelled transitions are listed in Table 5.3. Low statistics required the binning of the spectrum to 8 keV/bin instead of the 4 keV/bin typically used for most other γ spectra. The 854 keV peak corresponding to the $2_1^+ \rightarrow 0_{gs}^+$ transition is visible and the 1088 keV peak corresponding

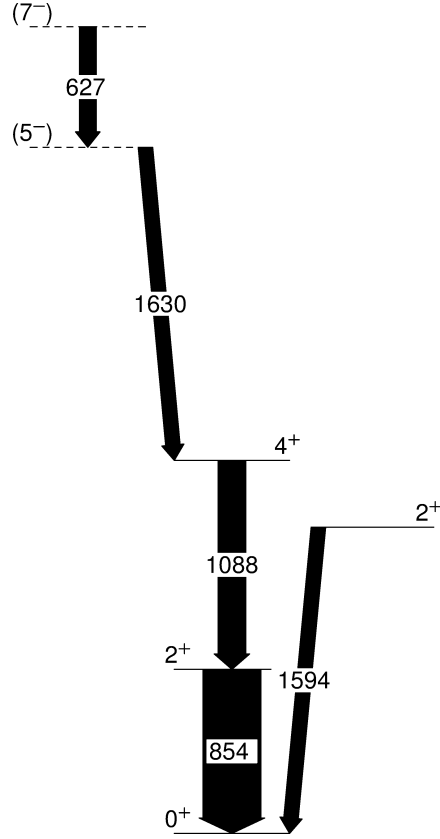


Figure 5.6: Partial level scheme for ^{68}Se identifying the excited states populated in this work. Arrow thickness corresponds to relative intensity of transition. Tentatively assigned spin-parities in the literature are in parentheses with a dashed level. See Table 5.3 for more details.

to the $4_1^+ \rightarrow 2_1^+$ transition can also be seen, feeding the 2_1^+ state with an intensity of 48(10)%. The 632(3) keV γ ray in Table 5.3 has been assigned to the $(7_1^-) \rightarrow (5_1^-)$ transition. The (5_1^-) state then depopulates to the 4_1^+ state via the 1629.1(7) keV transition, which has been attributed to the 1635(6) keV γ ray observed in this work. Both γ rays in this cascade have very low statistics, but if this assignment is correct it appears the (5_1^-) state populates the 4_1^+ state with about 50% intensity. Another transition at 1596(6) keV has been assigned to the known 1594(1) keV $2_2^+ \rightarrow 0_{gs}^+$ transition. No evidence is seen of the $2_2^+ \rightarrow 2_1^+$ transition at 740 keV. An exact branching ratio from the 2_2^+ state is not given in the literature, however previous work has shown the 1594(1) keV $2_2^+ \rightarrow 0_{gs}^+$ transition to be more intense than the 740 keV $2_2^+ \rightarrow 2_1^+$ transition [88], which is not inconsistent with the latter's absence above background in this work.

The peak observed at 752(3) keV was at first assumed to be the $2_2^+ \rightarrow 2_1^+$ transition,

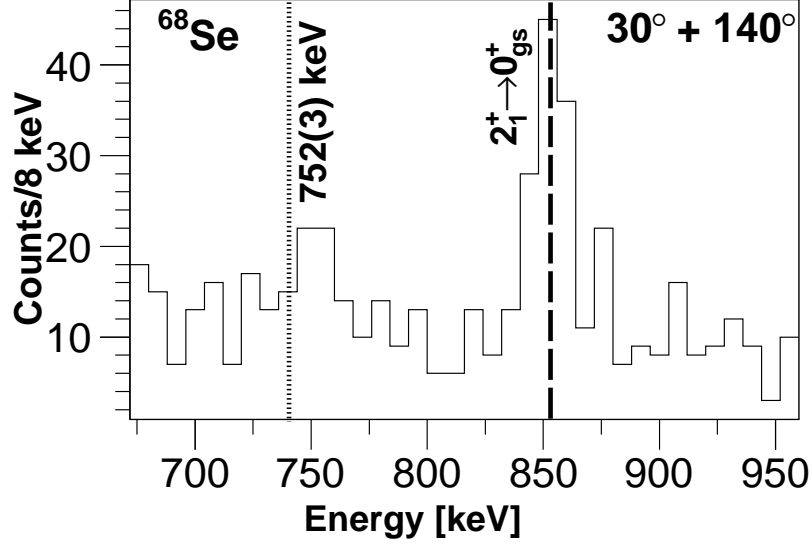


Figure 5.7: Target-only spectrum of ^{68}Se showing the area around the unidentified 752 keV peak. The literature energies of the $2_2^+ \rightarrow 2_1^+$ and $2_1^+ \rightarrow 0_{gs}^+$ transitions are given by the dotted and dashed lines, respectively. The 752 keV peak centroid does not line up to the literature value of the $2_2^+ \rightarrow 2_1^+$ transition.

Table 5.3: Transitions identified in ^{68}Se from target-only data (see Fig. 5.5). Shown are present (Pres.) and literature (Lit.) transition energies E_γ , measured intensities I_γ (where the $2_1^+ \rightarrow 0_{gs}^+$ intensity is set to 100), initial/final level energies/spin-parities and literature state mean lifetimes τ_m .

E_γ Pres. [keV]	E_γ Lit.♣ [keV]	I_γ	E_i [keV]	J_i^π	E_f [keV]	J_f^π	τ_m Lit. [ps]
515(2)	-	25(8)	-	-	-	-	-
632(3)	627.3(6)	29(10)	4199	(7_1^-)	3572	(5_1^-)	-
752(3)	-	38(11)	-	-	-	-	-
853(1)	853.8(2)	100	854	2_1^+	0.0	0_{gs}^+	4.2(6) [†]
1087(4)	1088.3(2)	48(10)	1942	4_1^+	854	2_1^+	-
1124(3)	-	36(11)	-	-	-	-	-
1596(6)	1594(1)	25(17)	1594	2_2^+	0.0	0_{gs}^+	-
1635(6)	1629.1(7)	25(17)	3572	(5_1^-)	1942	4_1^+	-
2270(3)	-	32(6)	-	-	-	-	-

♣ from [89]; † from [7].

however it lies 12 keV higher than the 740(1) keV literature value of the $2_2^+ \rightarrow 2_1^+$ peak (see Fig. 5.7 and Ref. [89]). Since the Doppler correction accurately places the $2_1^+ \rightarrow 0_{gs}^+$ transition within 1 keV of the literature energy, this implies that the transition observed at 752 keV is not from the 2_2^+ state. This discrepancy cannot be explained by a lifetime effect as this acts to lower the measured energy centroid relative to the literature value, not the other way around. It does not coincide with the decay of any known state in ^{68}Se .

Analysis of the ^{68}Se target-only spectrum revealed several other previously unobserved γ -ray transitions (see Fig. 5.5). Investigation of adjacent nuclei on the recoil ID plot determined that these peaks are not contaminants from other nuclei resulting from ineffective software cuts on recoil species, and the γ -ray widths are consistent with the widths of previously known transitions observed in ^{68}Se . The previously unobserved transitions are seen in both SeGA detector rings at similar energies. It is quite likely, therefore, that the transitions originate from ^{68}Se . Since it was not known which states the new γ rays originated from, it was assumed for the purposes of lifetime analysis that none feed the 2_1^+ state. Statistics were not sufficient to extract the effective lifetimes of these unknown states.

5.1.4 ^{72}Kr

Excited states in ^{72}Kr were populated via one-proton pickup in the target foil from the secondary ^{71}Br beam. The ^{72}Kr nuclei passed into the S800 at an energy of 82.1 AMeV. Gating target-only data on the ^{72}Kr recoils produced the γ spectrum shown in Fig. 5.8, which has been binned to 8 keV/bin due to low statistics. The transitions identified are listed in Table 5.4. Despite the relatively poor statistics the spectrum is clean enough to identify de-excitation γ rays. The only two peaks seen in ^{72}Kr correspond to the $2_1^+ \rightarrow 0_{gs}^+$ transition at 710 keV and the $4_1^+ \rightarrow 2_1^+$ transition at 610 keV. The ‘peaks’ seen at 250 keV and 380 keV in Fig. 5.8 are due to a binning effect, as they disappear when the spectrum is rebinned to 4 keV/bin from 8 keV/bin.

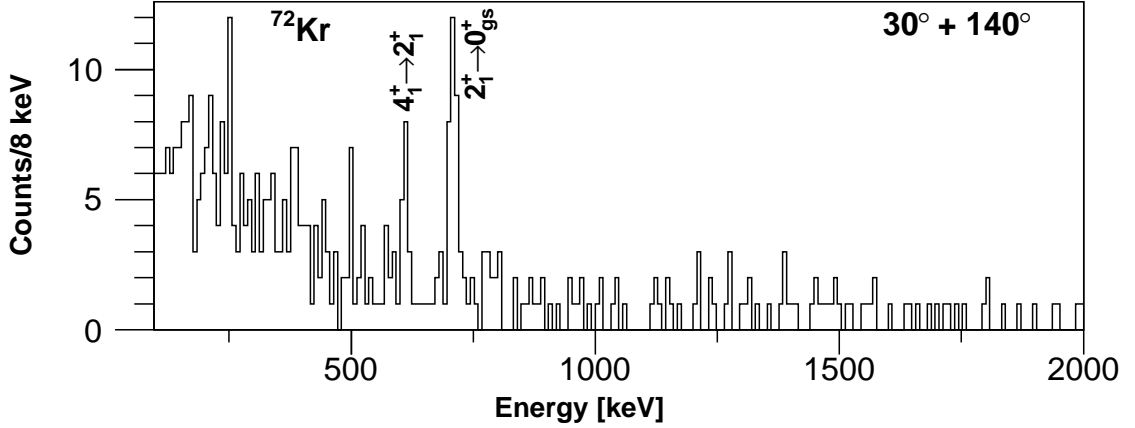


Figure 5.8: γ spectrum from gating target-only data on ^{72}Kr recoils. The observed transitions are labelled. See Table 5.4 for details.

Table 5.4: Transitions identified in ^{72}Kr from target-only data (see Fig. 5.8). Shown are present (Pres.) and literature (Lit.) transition energies E_γ , measured intensities I_γ (where the $2_1^+ \rightarrow 0_{gs}^+$ intensity is set to 100), initial/final level energies/spin-parities and literature state mean lifetimes τ_m .

E_γ Pres.	E_γ Lit.♣	I_γ	E_i	J_i^π	E_f	J_f^π	τ_m Lit.
[keV]	[keV]		[keV]		[keV]		[ps]
610(2)	611.68(14)	36(14)	1321	4_1^+	710	2_1^+	3.5(7) [‡]
712(2)	709.72(14)	100	710	2_1^+	0.0	0_{gs}^+	4.9(5) [†]

♣ from [90]; ‡ from [9]; † from weighted average of [8, 9].

5.1.5 ^{70}Se

^{70}Se entered the S800 at an energy of 77.8 AMeV. The γ spectrum resulting from gating target-only data on the ^{70}Se recoils is shown in Fig. 5.9, with the observed transitions listed in Table 5.5. A partial level scheme is given in Fig. 5.10. The ^{70}Se $2_1^+ \rightarrow 0_{gs}^+$ transition is clearly seen at 945 keV, as well as the following feeding transitions: the $3_1^{(-)} \rightarrow 2_1^+$ transition at 1574 keV, feeding with a relative intensity of 16.5(13)%; the $4_1^+ \rightarrow 2_1^+$ transition at 1093 keV, with an intensity of 30.5(16)%; and the $2_2^+ \rightarrow 2_1^+$ transition at 655 keV, with an intensity of 7.1(10)%. The non-yrast 2^+ state also decays via the $2_2^+ \rightarrow 0_{gs}^+$ transition at 1600 keV, overlapping with the $3_1^{(-)} \rightarrow 2_1^+$ peak at 1574 keV. The 2_2^+ state is fed by the $4_2^+ \rightarrow 2_2^+$ transition at 783 keV.

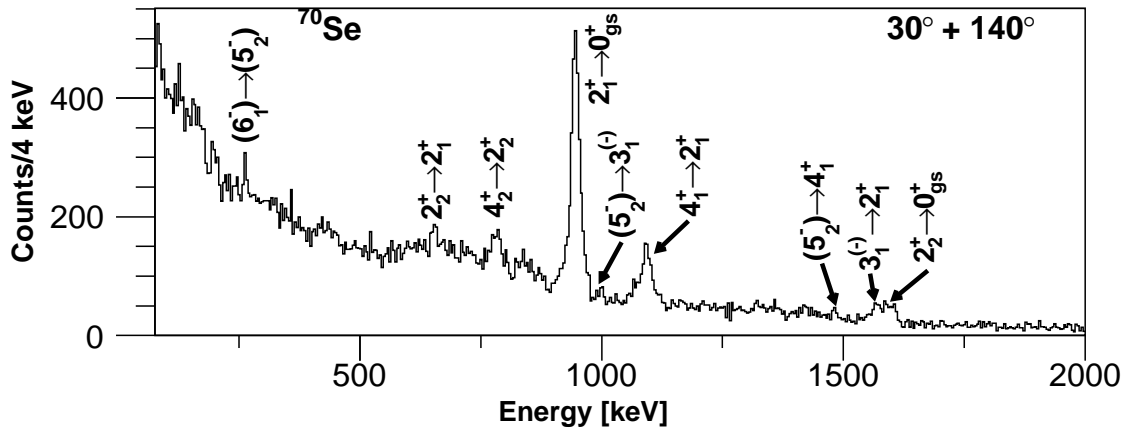


Figure 5.9: γ spectrum from gating target-only data on ^{70}Se recoils. The observed transitions are labelled. See Table 5.5 for more details.

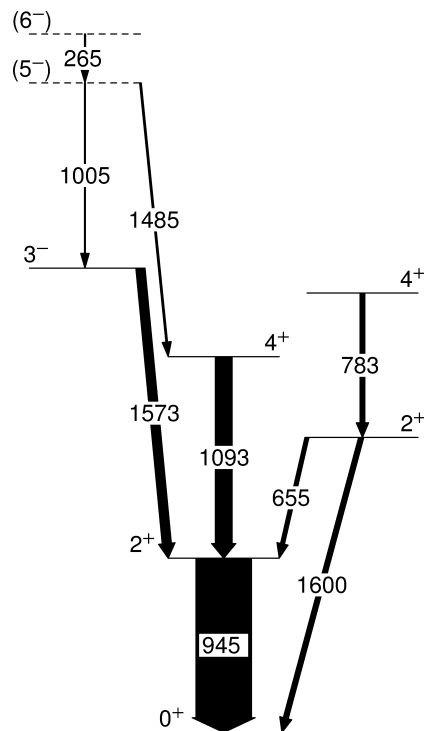


Figure 5.10: Partial level scheme for ^{70}Se identifying the excited states populated in this work. Arrow thickness corresponds to relative intensity of transition. Tentatively assigned spin-parities in the literature are in parentheses with a dashed level. See Table 5.5 for more details.

5.1. GAMMA SPECTROSCOPY RESULTS

Table 5.5: Transitions identified in ^{70}Se from target-only data (see Fig. 5.9). Shown are present (Pres.) and literature (Lit.) transition energies E_γ , measured intensities I_γ (where the $2_1^+ \rightarrow 0_{gs}^+$ intensity is set to 100), initial/final level energies/spin-parities and literature state mean lifetimes τ_m .

E_γ Pres. [keV]	E_γ Lit.♣ [keV]	I_γ	E_i [keV]	J_i^π	E_f [keV]	J_f^π	τ_m Lit. [ps]
262(1)	264.8(3)	2.0(10)	3788	(6^-)	3523	(5^-)	-
654(1)	655.1(5)	7.1(10)	1600	2_2^+	945	2_1^+	4.8(13) [†]
781(2)	782.6(3)	9.0(20)	2383	4_2^+	1600	2_2^+	$\leq 17^\ddagger$
946.1(3)	944.51(5)	100	945	2_1^+	0.0	0_{gs}^+	3.2(2) [‡]
1000(2)	1005.5(7)	2.0(10)	3523	(5^-)	2518	$3_1^{(-)}$	$\leq 12^\ddagger$
1092(1)	1093.3	30.5(16)	2038	4_1^+	945	2_1^+	1.4(1) [‡]
1482(2)	1485.2(5)	3.0(10)	3523	(5^-)	2038	4_1^+	$\leq 12^\ddagger$
1574(4)	1574.1(9)	16.5(13)	2518	$3_1^{(-)}$	945	2_1^+	6.1(9) [†]
1602(3)	1600.1(7)	9.0(7)	1600	2_2^+	0.0	0_{gs}^+	4.8(13) [†]

♣ from [91]; † from [92]; ‡ from [93].

5.1.6 ^{66}Ge

Excited states in ^{66}Ge were populated via 2p2n knockout of the secondary ^{70}Se beam at an energy of 77.4 AMeV. Gating target-only data on ^{66}Ge recoils produced the γ spectrum shown in Fig. 5.11. Each of the γ rays seen can be identified in the literature (see Table 5.6). A partial level scheme is shown in Fig. 5.12. The 2_1^+ state is fed by two transitions: the $4_1^+ \rightarrow 2_1^+$ transition with a relative intensity of 49(4)% and the $2_2^+ \rightarrow 2_1^+$ transition with an intensity of 20(2)%.

Two transitions at approximately 1490 keV in Fig. 5.11 overlapped with each other, and the statistics were insufficient for an accurate identification of their peak energies or relative intensities. The identities of these peaks have been assumed based on the level scheme available in the literature [99]. Their assignment has not been quoted as tentative as other γ rays in the same cascade as both transitions are clearly seen (see Fig. 5.11) and the large width of the peak in the target-only spectrum suggests the presence of two convoluted transitions. The intensities of these two γ peaks were extracted assuming the branching ratios from the 5_1^- state given in the literature [94] and the measured intensity of the 7_1^- state in this work. This therefore assumes 100% of the 5_1^- state is fed by the 7_1^- state, with no direct population. If

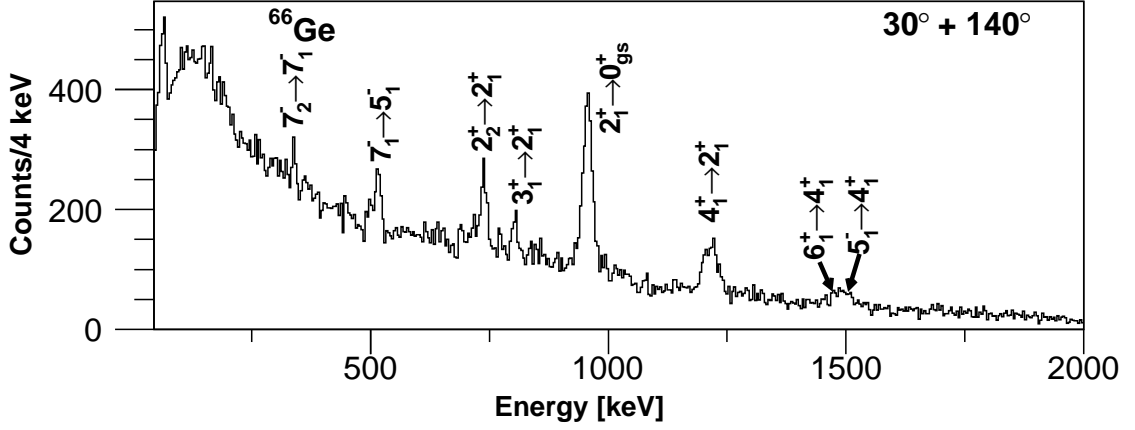


Figure 5.11: γ spectrum from gating target-only data on ^{66}Ge recoils. The observed transitions are labelled. See Table 5.6 for details.

Table 5.6: Transitions identified in ^{66}Ge from target-only data (see Fig. 5.11). Shown are present (Pres.) and literature (Lit.) transition energies E_γ , measured intensities I_γ (where the $2_1^+ \rightarrow 0_{gs}^+$ intensity is set to 100), initial/final level energies/spin-parities and literature state mean lifetimes τ_m .

E_γ Pres. [keV]	E_γ Lit. [♠] [keV]	I_γ	E_i [keV]	J_i^π	E_f [keV]	J_f^π	τ_m Lit. [ps]
338.4(9)	338.2(1)	5(1)	4543	7_2^-	4205	7_1^-	86(6) [♣]
515(1)	521.4(2)	21(2)	4205	7_1^-	3683	5_1^-	276(13) ^{♣‡}
738.4(6)	736.1(1)	20(2)	1693	2_2^+	957	2_1^+	6.5(25) [‡]
803.4(9)	802.0(1)	11(3)	2495	3_1^+	1693	2_2^+	-
956.5(4)	956.9(1)	100	957	2_1^+	0.0	0_{gs}^+	3.68(17) [†]
1215(1)	1216.4(1)	49(4)	2173	4_1^+	957	2_1^+	≤ 2.0 ^{‡,♣}
≈ 1490	1480.7(1)	19(3)	3654	6_1^+	2173	4_1^+	≤ 6.1 [♣]
≈ 1490	1510.1(1)	11(3)	3683	5_1^-	2173	4_1^+	32(3) ^{‡,♣}

♠ [94]; † [95–97] (weighted); ‡ [96]; ♣ [98].

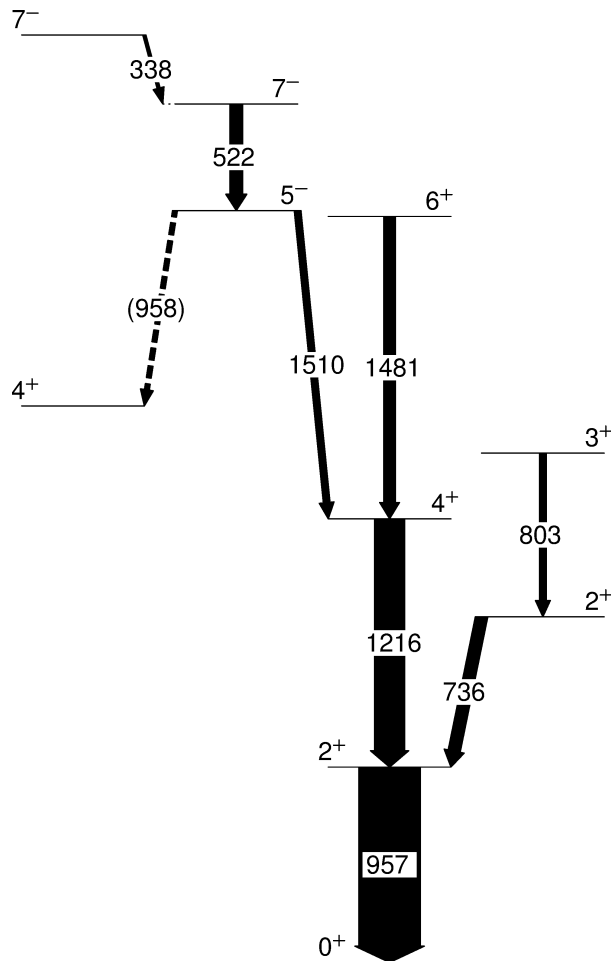


Figure 5.12: Partial level scheme for ^{66}Ge identifying the excited states populated in this work. Arrow thickness corresponds to relative intensity of transition. A tentative transition from the 5_1^- state to the 4_2^+ state is shown, although no decays from the 4_2^+ are seen. See Table 5.6 for more details.

there is also significant direct population of the 5_1^- state, the intensity of the $5_1^- \rightarrow 4_1^+$ transition will be underestimated and the intensity of the $6_1^+ \rightarrow 4_1^+$ transition will be overestimated.

The 5_1^- state is known to depopulate to states other than the 4_1^+ state. The strongest of these other transitions is the known 957.7 keV $5_1^- \rightarrow 4_2^+$ transition. This lies directly beneath the $2_1^+ \rightarrow 0_{gs}^+$ peak at 956.9 keV. Given the assumptions made in this work to extract the $5_1^- \rightarrow 4_1^+$ transition intensity, the $5_1^- \rightarrow 4_2^+$ transition intensity is expected to be 8% relative to the $2_1^+ \rightarrow 0_{gs}^+$ transition. It should be noted that decays from the 4_2^+ state (with known energies of 553 keV, 1032 keV and 1769 keV) are not seen above background in this work (see Fig. 5.11). The lifetime obtained for the 2_1^+

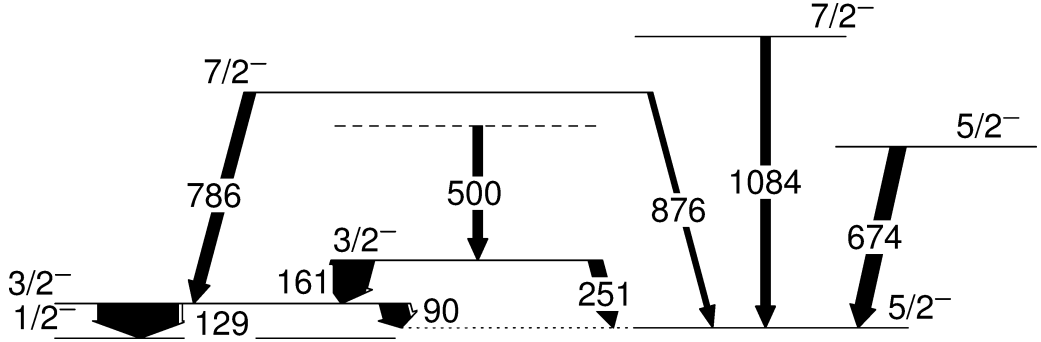


Figure 5.14: Partial level scheme for ^{69}Se identifying the excited states populated in this work. Arrow thickness corresponds to relative intensity of transition. The tentatively assigned 500 keV transition has been marked with a dashed initial level. See Table 5.7 for details.

$\frac{7}{21}^- \rightarrow \frac{3}{21}^-$ transition, with an intensity of 14(1)% relative to the 129 keV transition. The former feeding state, the $\frac{3}{22}^-$ state at an excitation energy of 290 keV, also feeds the known yrast $\frac{5}{2}^-$ state at an excitation energy of 39 keV via the known $\frac{3}{22}^- \rightarrow \frac{5}{21}^-$ 251 keV transition. It was not possible to see the subsequent depopulating 39 keV $\frac{5}{21}^- \rightarrow \frac{1}{2_{gs}}^-$ transition to the ground state as the $\frac{5}{21}^-$ state is too long-lived (lifetime on the order of microseconds [102]). The $\frac{7}{21}^-$ state, aside from feeding the yrast $\frac{3}{2}^-$ state via the 786 keV transition, also feeds the yrast $\frac{5}{2}^-$ state via the 876 keV transition.

Two weak γ rays were observed from de-exciting ^{69}Se recoils that cannot be identified from the literature. These transitions, labelled with their γ energies in Fig. 5.13, appear at measured energies of 499.8(5) keV and 524(1) keV. Thanks to the large level of statistics it was possible to perform coincidence measurements to identify the location of the 500 keV γ ray in the level scheme. Fig. 5.15 shows the results of coincidence gating on the 129 keV $\frac{3}{21}^- \rightarrow \frac{1}{2_{gs}}^-$ and 161 keV $\frac{3}{22}^- \rightarrow \frac{3}{21}^-$ transitions, with a subtraction to remove effects of random background. Background contributions were removed by subtracting a spectrum gated on a γ background close in energy to the gated transition with an identical bin width. The 500 keV transition is shown to come in coincidence with transitions from the yrast and non-yrast $\frac{3}{2}^-$ states. Since no other γ rays are seen in coincidence it is likely that the 500 keV transition feeds the $\frac{3}{22}^-$ state, which sits at an excitation energy of 290 keV (see Fig. 5.14).

It is possible that this unknown state is fed by a γ ray from the yrast $\frac{7}{21}^-$ state, which sits at an excitation energy of 915 keV. The γ -ray energy between the $\frac{7}{21}^-$ state and this new state at $E_x = 790$ keV would be $915 - 790 = 125$ keV. This would

5.1. GAMMA SPECTROSCOPY RESULTS

Table 5.7: Transitions identified in ^{69}Se from target-only data (see Fig. 5.13). Shown are present (Pres.) and literature (Lit.) transition energies E_γ , measured intensities I_γ (where the 129 keV $\frac{3}{2}_1^- \rightarrow \frac{1}{2}_{gs}^-$ intensity is set to 100) and initial/final level energies/spin-parities. The 500 keV transition observed for the first time in this work has been tentatively assigned to the level scheme based on coincidence measurements (see Fig. 5.15).

E_γ Pres. [keV]	E_γ Lit.♣ [keV]	I_γ	E_i [keV]	J_i^π	E_f [keV]	J_f^π
86.0(3)	90.3(4)	33(4)	129	$\frac{3}{2}_1^-$	39	$\frac{5}{2}_1^-$
125.70(7)	129.1(2)	100	129	$\frac{3}{2}_1^-$	0.0	$\frac{1}{2}_{gs}^-$
158.8(1)	161.3(4)	51(3)	290	$\frac{3}{2}_2^-$	129	$\frac{3}{2}_1^-$
247.6(3)	250.7(2)	17(1)	290	$\frac{3}{2}_2^-$	39	$\frac{5}{2}_1^-$
499.8(5)	-	11(1)	(790)	?	290	$\frac{3}{2}_2^-$
524(1)	-	4(1)	-	-	-	-
674.2(8)	673.7(3)	19(3)	713	$\frac{5}{2}_2^-$	39	$\frac{5}{2}_1^-$
784.4(8)	786.4(5)	14(1)	915	$\frac{7}{2}_1^-$	129	$\frac{3}{2}_1^-$
~880	876.3(1)	6(1)	915	$\frac{7}{2}_1^-$	39	$\frac{5}{2}_1^-$
1083(1)	1084.6(3)	11(1)	1123	$\frac{7}{2}_2^-$	39	$\frac{5}{2}_1^-$

♣ from [102].

sit almost directly underneath the 129 keV transition in the γ spectra. Gating on the 129 keV γ ray shows a small peak at 125 keV (see left-hand panel of Fig. 5.15), which is possibly the transition from the $\frac{7}{2}_1^-$ state to this new state. However, the peak is only one bin wide and therefore may not be real. It is expected that the intensity of this potential 125 keV γ ray is no larger than 11% the intensity of the 129 keV transition, since this is the intensity of the depopulating 500 keV γ ray (see Table 5.7).

The 524 keV transition was too weak for γ coincidence gating to be used to identify its place in the level scheme. Since the software gating on recoil species in this analysis is quite clean it is likely that this γ ray does originate from an excited state in ^{69}Se . Of the recoils that surround ^{69}Se on the recoil ID plot (^{71}Br , $^{70,68}\text{Se}$ and $^{68,67}\text{As}$) only ^{68}As and ^{71}Br have known γ rays around the same energy as the 524 keV transition. In ^{68}As there exists the known $5_1^+ \rightarrow 4_1^+$ transition at 519 keV, and in ^{71}Br there is the known $(\frac{7}{2}_3^-) \rightarrow (\frac{5}{2}_2^-)$ transition at 522 keV. Gating on ^{68}As recoils shows a peak at 519 keV with approximately the same intensity as the 524 keV peak in

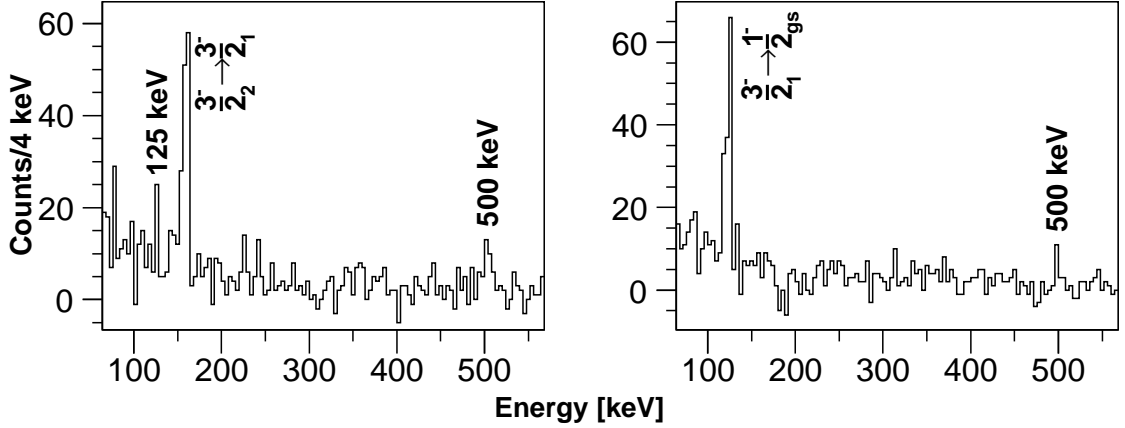


Figure 5.15: ^{69}Se γ coincidence spectra. The left-hand panel shows a spectrum coincidence gated on the 129 keV $\frac{3}{21}^- \rightarrow \frac{1}{2}_{gs}^-$ transition. The right-hand panel shows a spectrum coincidence gated on the 161 keV $\frac{3}{22}^- \rightarrow \frac{3}{21}^-$ transition. Both spectra have been background subtracted. The new 500 keV transition appears to come in coincidence with both these transitions. There is a potential 125 keV peak also seen, which is expected to feed the new state from the $\frac{7}{21}^-$ state. See Table 5.7 for more details.

the ^{69}Se spectrum, however particle software gates should cut the majority of this out and so this is unlikely to be the source of the γ ray. The 522 keV γ ray known to come from ^{71}Br is not seen at all in this work.

The transition labelled with a * in Fig. 5.13 is most likely from radiative electron capture onto the ^{70}Se secondary beam (discussed in Section 6.5). The transition labelled with a # in Fig. 5.13 is not a γ ray from ^{69}Se as it is broad and only found in the forward SeGA ring (implying a poor Doppler correction). Analysis of the equivalent lab frame γ spectrum shows the peak is sharper in the lab frame and appears in both SeGA rings at a similar energy (see Fig. 5.16). The measured energy centroid of 844.2(9) keV in this work is consistent with the 843.76(10) keV $\frac{1}{21}^+ \rightarrow \frac{5}{2}_{gs}^+$ transition in ^{27}Al . This suggests that this γ ray comes from excitations of nuclei in the plunger housing. It is not obvious why this γ ray is not also seen in the γ spectra corresponding to other recoils in this work. It does appear to be quite weak in intensity and so it may be that it only appears significantly above background in the ^{69}Se γ spectra because of the relatively high statistics.

The two observed decays from the $\frac{7}{21}^-$ state, i.e., the 786 keV $\frac{7}{21}^- \rightarrow \frac{3}{21}^-$ and the 876 keV $\frac{7}{21}^- \rightarrow \frac{5}{21}^-$ transitions, are interesting as their branching ratios can be compared to the literature. The measured branching ratios of the 786 keV and 876 keV transitions

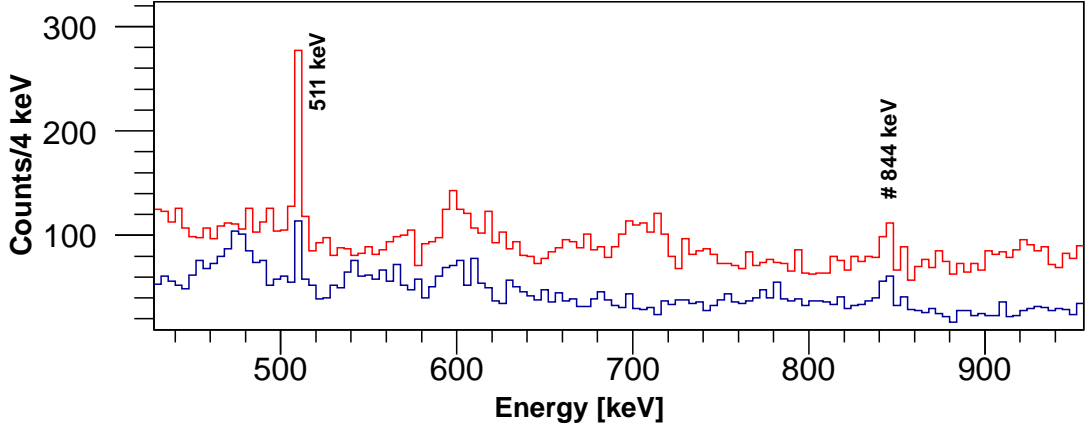


Figure 5.16: Target-only γ spectrum of ^{69}Se recoils as measured in the lab frame. Data corresponding to forward and backward SeGA detector angles are shown in red and blue, respectively. The 844 keV peak corresponding to the $\frac{1}{2}_1^+ \rightarrow \frac{5}{2}_{gs}^+$ transition in ^{27}Al is visible (labelled #). Also visible is the 511 keV annihilation peak.

in this work were 70(10)% and 30(8)%, respectively. This is in good agreement with the work of Jenkins *et al.* [100], who extract 75(11)% and 25(4)% for the 786 keV and 876 keV transitions, respectively. However, it does not agree with the results of Stefanescu *et al.* [101], who extract 35(4)% and 65(5)% for the 786 keV and 876 keV transitions, respectively. In both previous experiments fusion-evaporation reactions were used to study high- and low-spin states in ^{69}Se . Both studies used the $^{40}\text{Ca}(^{32}\text{S},2\text{pn})^{69}\text{Se}$ reaction. Stefanescu *et al.* used two different and independent gating conditions to retrieve their result for the 786 keV/876 keV branching ratio, in one case gating on a γ ray just above the $\frac{7}{2}_1^-$ state. It is not clear why the coincidence-gating work of Jenkins *et al.* led to different branching ratios being extracted.

The branching ratios of the 161 keV and 251 keV transitions from the $\frac{3}{2}_2^-$ state are not in complete agreement with the literature. The branching ratios extracted in this work for the 161 keV and 251 keV transitions are 75(6)% and 25(2)%, respectively, whereas in the literature the 161 keV and 251 keV branching ratios are quoted as 51(19)% and 49(9)%, respectively [101]. The branching ratio uncertainties in Ref. [101] are large because the $\frac{3}{2}_2^-$ state was not populated strongly in their work. The transitions were not observed at all in the work of Jenkins *et al.* [100].

The branching ratios of the 129 keV and 90 keV transitions from the $\frac{3}{2}_1^-$ state to the $\frac{1}{2}_{gs}^-$ and $\frac{3}{2}_1^-$ states, respectively, can also be compared to previous work. The

5.1. GAMMA SPECTROSCOPY RESULTS

Table 5.8: Transitions identified in ^{65}Ga from target-only data (see Fig. 5.17). Shown are present (Pres.) and literature (Lit.) transition energies E_γ , measured intensities I_γ (where the $\frac{5}{21}^- \rightarrow \frac{3}{2}^-_{gs}$ transition intensity is set to 100), initial/final level energies/spin-parities and literature state mean lifetimes τ_m .

E_γ Pres. [keV]	E_γ Lit. [♣] [keV]	I_γ	E_i [keV]	J_i^π	E_f [keV]	J_f^π	τ_m Lit. [ps]
187.5(2)	190.8(2)	100	191	$\frac{5}{21}^-$	0.0	$\frac{3}{2}^-_{gs}$	$\leq 1010^\dagger$
751.4(7)	750.9(1)	30(5)	2038	$\frac{9}{21}^+$	1287	$(\frac{9}{21})^-$	$10(6)^\dagger$
	752(2)	26(4)	815	$\frac{3}{22}^-$	62	$(\frac{1}{2})^-_1$	-
813(3)	814.9(1)	12(3)	815	$\frac{3}{22}^-$	0.0	$\frac{3}{2}^-_{gs}$	-
883(3)	884.9(3)	6(2)	1076	$\frac{7}{21}^-$	191	$\frac{5}{21}^-$	-
1032(1)	1027.1(1)	26(4)	3065	$\frac{13}{21}^+$	2038	$\frac{9}{21}^+$	-
1075(5)	1075.9(3)	15(2)	1076	$\frac{7}{21}^-$	0.0	$\frac{3}{2}^-_{gs}$	-
1095(1)	1096.3(4)	47(6)	1287	$(\frac{9}{21})^-$	191	$\frac{5}{21}^-$	$\leq 2.0^\dagger$
1509(3)	1501.5(1)	9(2)	2789	$\frac{13}{21}^-$	1287	$(\frac{9}{21})^-$	$0.9(4)^\ddagger$

♣ from [103]; ‡ from [104]; † from [105].

129 keV/90 keV branching ratios in this work were measured to be 75(9)%/25(3)%. This is in good agreement with the equivalent branching ratios of 77(2)%/23(2)% in the literature [102].

5.1.8 ^{65}Ga

Excited states in ^{65}Ga were populated in two separate reactions in this experiment; via 3p2n knockout from the ^{70}Se secondary beam and via 2p2n knockout from the ^{69}As secondary beam. Excited recoils emerged from the target at an energy of 74.9 AMeV. Gating target-only data on ^{65}Ga recoils produced the γ spectra shown in Fig. 5.17. The transitions are listed in Table 5.8. A partial level scheme is shown in Fig. 5.18. A number of γ rays are seen and all can be identified from the literature (see Table 5.8). Both ^{70}Se and ^{69}As secondary beams appear to populate identical states in ^{65}Ga with virtually the same intensities.

Two γ rays were found to overlap at ~ 750 keV in the ^{65}Ga γ spectrum. The presence of the 751 keV $\frac{9}{21}^+ \rightarrow (\frac{9}{21})^-$ transition is inferred from the presence of two other γ rays

in the same cascade: the 1027 keV $\frac{13}{2}^+ \rightarrow \frac{9}{2}^+$ transition and the 1096 keV $(\frac{9}{2}^-) \rightarrow \frac{5}{2}^-$ transition (see Fig. 5.17). Similarly, the presence of the 752 keV $\frac{3}{2}^- \rightarrow (\frac{1}{2})^-$ transition is inferred from the presence of the 815 keV γ ray, which also comes from the $\frac{3}{2}^-$ state. From the known branching ratios in the literature for the two γ rays from the $\frac{3}{2}^-$ state [105] it was possible to approximate how much of the measured ~ 751 keV peak in this work was coming from each of the $\frac{9}{2}^+$ and $\frac{3}{2}^-$ states. The results are quoted in Table 5.8.

5.2 Lifetime Results

The central physics interest in this work was the measurement of low-lying excited state lifetimes in $A \sim 70$, $N = Z$ nuclei. In this section excited state lifetimes extracted using χ^2 fits to simulated spectra (see Section 4.4) are presented. Before a state lifetime is extracted the effective lifetimes of any feeding states are deduced and taken into account. When it was not possible to extract a feeding state lifetime because of statistical constraints, the literature lifetime of the state (if known) is assumed. If no literature lifetime exists, assumptions are made that are stated on a case-by-case basis.

5.2.1 ^{62}Zn

The zero-offset foil separation of 275 μm was deduced by altering the zero-offset value in the simulations until the ^{62}Zn 2_1^+ lifetime agreed with the literature (see Section 4.7). The following subsection presents the lifetime results extracted assuming the adopted 275 μm zero-offset distance.

Feeding State Lifetimes

The 2_2^+ state, which feeds the 2_1^+ state with an intensity of 14(2)%, did not appear to have any states feeding it. It was not possible to extract the effective lifetime of the 2_2^+ state in this work due to the low level of statistics, so instead the literature lifetime of 3.8(6) ps was assumed [87].

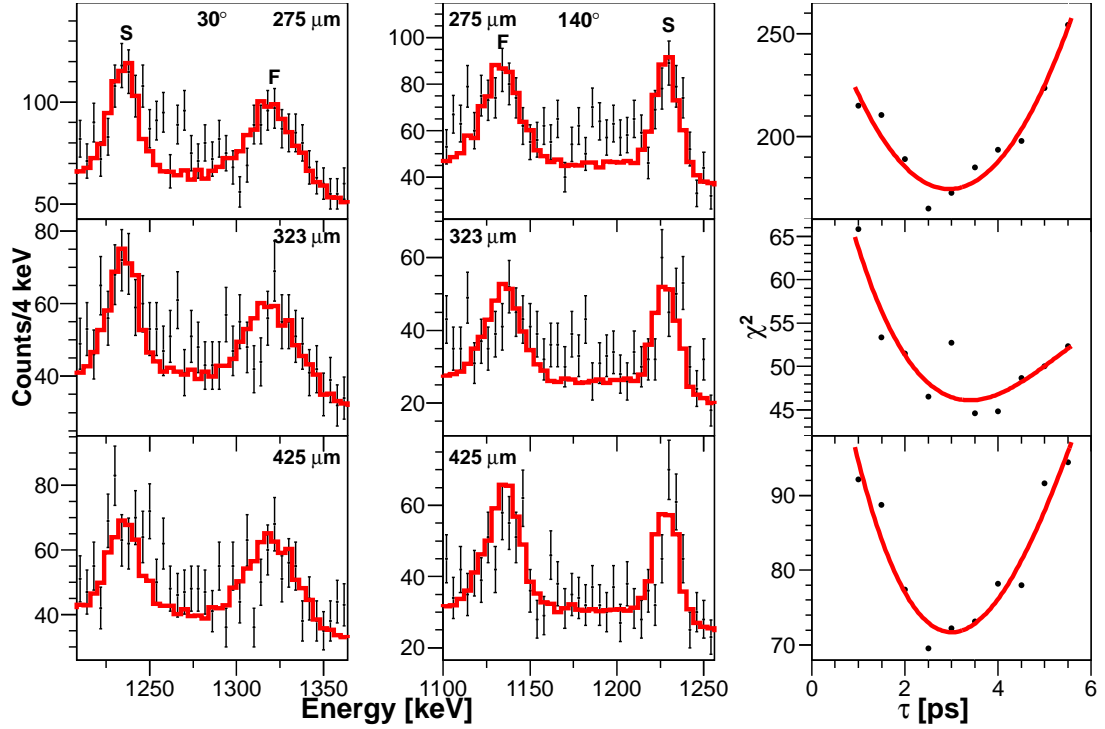


Figure 5.19: Left and centre columns: Experimental data (black points) and best-fit simulated lineshapes (red line) for the $4_1^+ \rightarrow 2_1^+$ transition in ^{62}Zn at 30° (left) and 140° (centre) detector angles. Fast (F) and slow (S) peaks are labelled and correspond to decays before and after the degrader foil, respectively. The fits to $323 \mu\text{m}$ 140° and $425 \mu\text{m}$ 30° data were excluded from the analysis (see text). Right column: total χ^2 minimisation plots for both SeGA rings (where possible) for the three distances shown.

The 4_1^+ state was observed in this work to be populated by the 6_1^+ and 4_2^+ states. The fits used to extract the effective lifetime of the 4_1^+ state are shown in Fig. 5.19. The fits to $323 \mu\text{m}$ 140° and $425 \mu\text{m}$ 30° data gave inconsistent results (lifetimes extracted from these two fits were over three standard deviations away from the average of the other four fits) and thus were excluded from the analysis. The right-hand column of Fig. 5.19 shows the χ^2 minimisation plots corresponding to the three distances. As with all plots of this kind in the following chapter, these plots are for *both SeGA rings added together*, unless data are excluded. If this is done in the analysis it will be specifically noted and reasons for excluding any data will be given.

Fig. 5.19 highlights a problem present in some of the fits in this work; in some cases there is a significant background contribution between the ‘fast’ and ‘slow’ peaks that is not replicated in the simulations. It is not clear what caused the presence of

this extra contribution, as it is not always present and so is unlikely to be a lineshape effect owing to γ de-excitations within the foils. It is unlikely that another γ -ray is present as it would be identifiable in the target-only runs (see Section 5.1). It would be useful for further work to be performed with the simulations to replicate this extra background contribution, however this could not be done in this work. It was assumed during the analysis that the extra background component was not a lifetime effect of the decaying state being analysed.

The lifetime of the ^{62}Zn 4_1^+ state extracted in this work (3.00(35) ps) disagrees with the result quoted in the literature (0.76(27) ps [87]) due to the influence of two feeding cascades. The $4_2^+ \rightarrow 4_1^+$ transition feeds the 4_1^+ state with a 34(5)% intensity relative to the $4_1^+ \rightarrow 2_1^+$ transition and the 4_2^+ state has a known absolute lifetime of 3.4(3) ps [87] (see Table 5.7). The $6_1^+ \rightarrow 4_1^+$ transition, feeding the 4_1^+ state with an intensity of 37(5)% relative to the $4_1^+ \rightarrow 2_1^+$ transition, would not itself significantly delay the 4_1^+ decay as the 6_1^+ state lifetime is only 0.36(5) ps [87]. However, in this work the 6_1^+ state is fed significantly by the (7_2^-) state, which has been shown to have a relatively long lifetime (12(5) ps [87]). Statistics were not high enough for lifetimes to be measured for these higher-lying states.

2_1^+ State Lifetime

The fits used to extract the lifetime of the 2_1^+ state in ^{62}Zn , following corrections for feeding and assuming a zero-offset of 275 μm , are shown in Fig. 5.20. The 275 μm 30° experimental spectrum gave inconsistent results compared with all other spectra (the fit gave a result over three standard deviations away from the average of the other fits) and was therefore excluded from the analysis. The 275 μm χ^2 plot in Fig. 5.20 corresponds only to backward SeGA ring data. The lifetime of the 2_1^+ state extracted in this work is 4.25(58) ps, which is in excellent agreement with the literature lifetime of 4.23(20) ps [84]. This is not surprising as the zero-offset was deliberately chosen so that the simulated fits extracted the literature lifetime for this state.

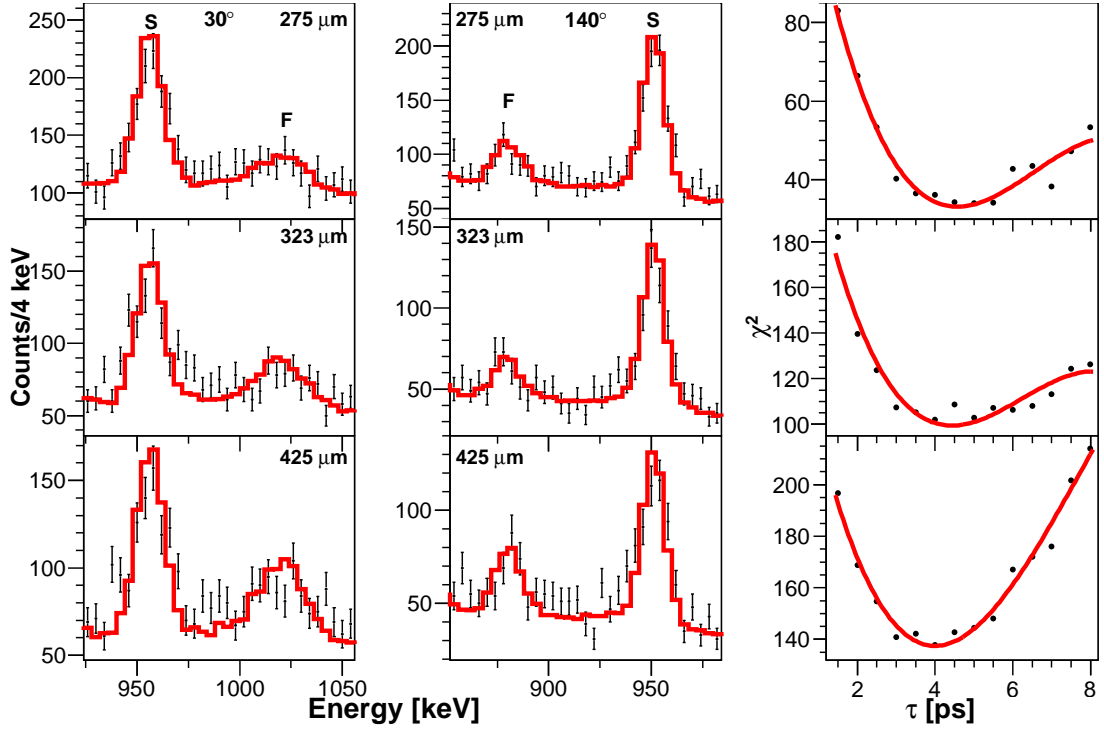


Figure 5.20: Left and centre columns: Experimental data (black points) and best-fit simulated lineshapes (red line) for the $2_1^+ \rightarrow 0_{gs}^+$ transition in ^{62}Zn at 30° (left) and 140° (centre) detector angles. Fast (F) and slow (S) peaks are labelled and correspond to decays before and after the degrader foil, respectively. Data from $275 \mu\text{m}$ 30° were excluded (see text). Right column: χ^2 minimisation plots for the three distances shown.

5.2.2 ^{70}Br

5_1^+ and 3_1^+ State Lifetimes

The 321 keV transition from the 5_1^+ state in ^{70}Br exhibited a complete absence of ‘fast’ RDDS component in any of the distance γ -ray spectra (see Fig. 5.21). This, coupled with the lower-than-literature recorded energy for the 321 keV γ ray and the low-energy tail, suggests that the lifetime of the state is very long (hundreds of picoseconds). The lifetime was therefore determined using a lineshape method as described in Ref. [10]. For long-lived (≥ 100 ps) lifetimes, γ -ray lineshapes recorded at backward SeGA angles are much less sensitive (and sometimes completely insensitive) to state lifetime and so only forward ring (30°) SeGA data were used in the analysis of the 5_1^+ state. Significant background noise in the 425 μm and 4.275 mm spectra (source unknown) meant that the χ^2 fits failed to find a mini-

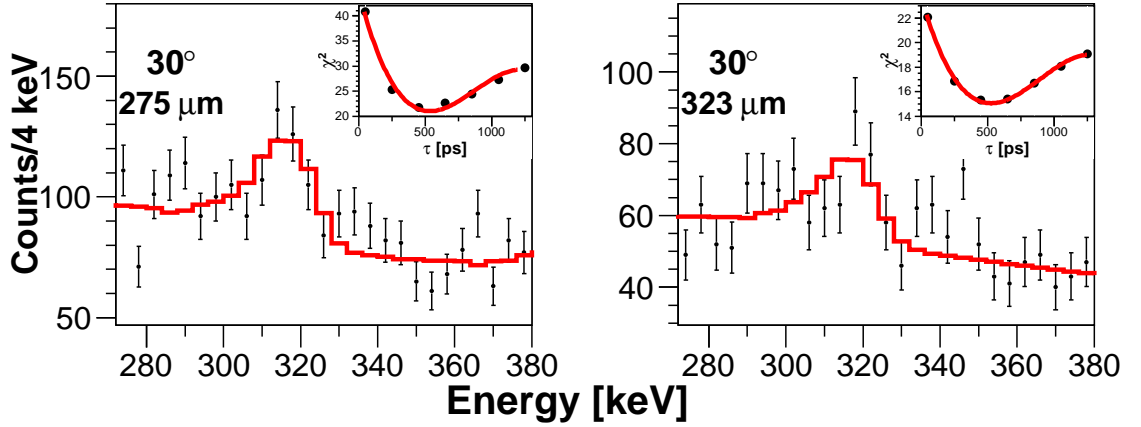


Figure 5.21: Experimental data (black points) and best-fit simulated lineshapes (red line) for the $5_1^+ \rightarrow 3_1^+$ transition in ^{70}Br . Data are shown for forward angles for target-degrader separations of $275 \mu\text{m}$ and $323 \mu\text{m}$ (left and right panels, respectively). The inset to each plot shows the corresponding χ^2 minimisation plot.

mum. The lifetime extracted from fits to the $275 \mu\text{m}$ and $323 \mu\text{m}$ forward angle data is $540(120)$ ps. These fits are shown in Fig. 5.21. Since there is no clear evidence for higher-lying states feeding the 5_1^+ state, this result is assumed to represent the actual lifetime of the state. The measured lifetime gives a corresponding $B(E2; 5_1^+ \rightarrow 3_1^+)$ of $450(100) e^2\text{fm}^4$.

The 403 keV γ ray from the 3_1^+ state only contained ‘fast’ and ‘slow’ RDDS components at the largest distance measured (4.275 mm) - see Fig. 5.22. The lifetime deduced from the χ^2 fits is $32(15)$ ps (see Fig. 5.23). This is assumed to be the true lifetime since the only observed feeding transition (321 keV) was taken into account in the analysis. The long lifetime of the 5_1^+ state results in the low-energy tail on the slow component of the 403 keV γ ray at the forward SeGA angle (see Fig. 5.23). The χ^2 fit is not as good as others shown in the analysis owing to influences from background fluctuations, low statistics and the effects of the long-lived 5_1^+ state. It was noted that large fluctuations ($\sim 100\%$) in the lifetime of the 3_1^+ state had a negligible effect on the lifetime of the 2_1^+ state (presented and discussed below). At these $\pm 100\%$ 3_1^+ lifetime extremes, the simulated γ spectra matched very badly to the experimental spectra for the $3_1^+ \rightarrow 2_1^+$ transition, whereas (despite the poor χ^2 fit) the γ -ray lineshape simulated fits look quite reasonable in Fig. 5.23. Assuming a pure M1 decay, a feature consistent with the published directional correlation from oriented state (DCO) measurements [12] and shell model calculations (see Section 6.3.2) for the 403 keV γ ray, the measured lifetime yields a $B(M1; 3_1^+ \rightarrow 2_1^+)$ of

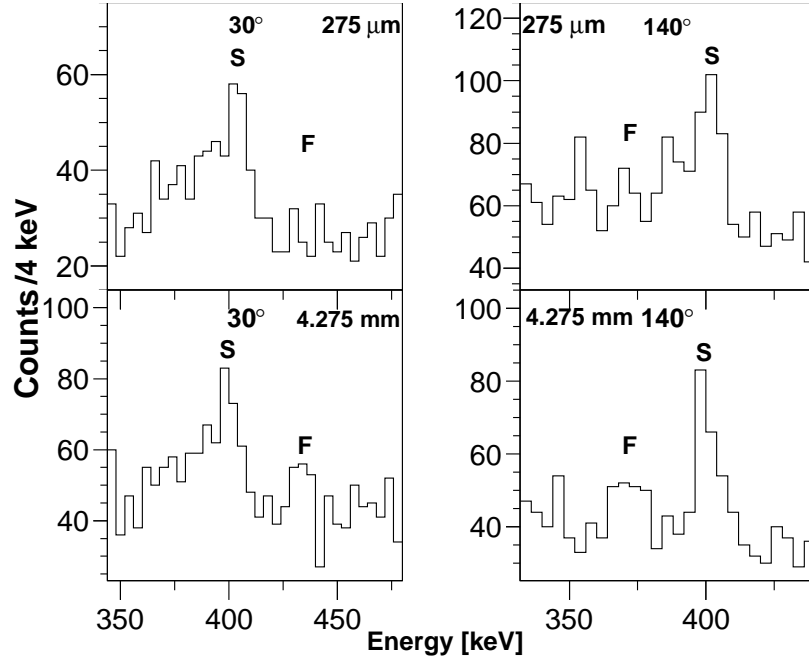


Figure 5.22: Experimental data gated on ^{70}Br recoils, showing the $3_1^+ \rightarrow 2_1^+$ transition. Data are shown for target-degrader separations of $275 \mu\text{m}$ (top) and 4.275 mm (bottom). Fast (F) and slow (S) components are labelled and correspond to decays before and after the degrader foil, respectively. At large distance (4.275 mm) there is evidence of a ‘fast’ RDDS component, but no such component is visible in the smaller target-degrader separation spectra.

$$0.027(13) \mu_N^2.$$

2_1^+ State Lifetime

The simulated fits used to extract the yrast 2^+ state lifetime in ^{70}Br , following corrections for feeding, are shown in Fig. 5.24. The χ^2 plots shown are for both SeGA rings added together, except for the $425 \mu\text{m}$ plot which only contains forward angle contributions. During the analysis it was noted that the experimental γ spectrum of ^{70}Br at $425 \mu\text{m}$ 140° showed an unconventional lineshape, where the ‘slow’ experimental RDDS peak appeared much wider than the simulated equivalent in all backward SeGA detectors (see bottom right panel of Fig. 5.24). It is not clear what caused this effect. The simulated fit to this spectrum yielded a lifetime value that was inconsistent with lifetimes extracted from the other target-degrader separations (differing by more than three standard deviations from the average of the other fits), and so this particular result was excluded. The deduced mean lifetime using a χ^2 fit

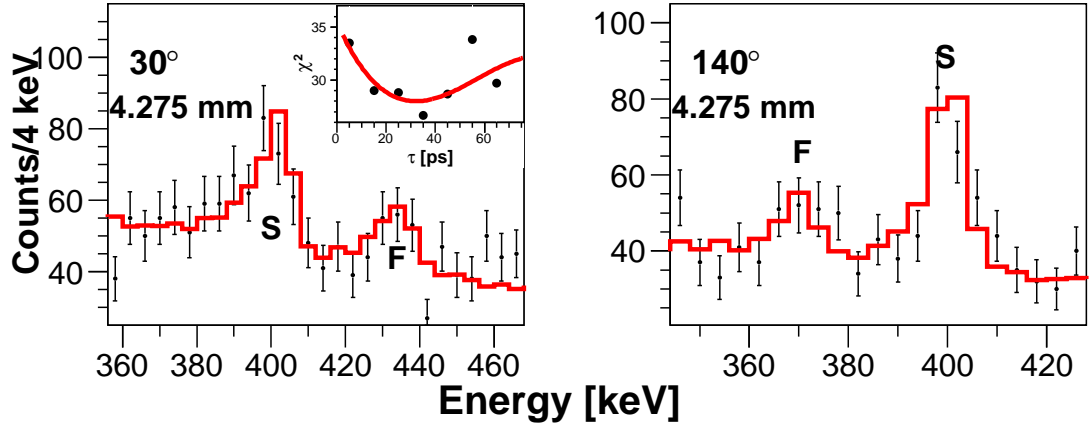


Figure 5.23: Experimental data (black points) and best-fit simulated lineshapes (red line) for the $3_1^+ \rightarrow 2_1^+$ transition in ^{70}Br . Data are shown for forward and backward angles (left and right panels, respectively) for the large target-degrader separation of 4.275 mm. The inset to the left-hand figure shows the χ^2 minimisation plot for both angles used to calculate the lifetime.

is $\tau(2_1^+) = 3.96(58)$ ps, which gives a corresponding $B(E2; 2_1^+ \rightarrow 0_{gs}^+)$ of $291(43) e^2\text{fm}^4$.

It is assumed in this work that the de-orientation effect acts to rapidly wash out any spatial alignment of recoils after emergence from the target foil (see Subsection 3.3.1). Effects of a 20% spatial alignment of recoils (typical for one-nucleon knockout [71]) were nevertheless investigated in this work for the case of ^{70}Br . Assuming an alignment of 20% for the recoils results in an effective increase of the 403 keV γ -ray intensity from 23.6% to 27.5%, which in turn decreases the lifetime of the 2_1^+ state by 0.06 ps from the value quoted above to 3.90 ps ($B(E2\downarrow) = 296 e^2\text{fm}^4$). This effect is small compared to other systematic errors considered in this work.

5.2.3 ^{68}Se

The $4_1^+ \rightarrow 2_1^+$ transition in ^{68}Se sat next to another, previously unobserved γ -ray peak at 1123(3) keV. In all distance spectra the RDDS peaks corresponding to the two decays overlapped, making determination of the 4_1^+ state effective lifetime impossible. As a result, the lifetime of the 2_1^+ state in ^{68}Se was obtained via two methods (a) assuming 100% fast feeding and (b) assuming the 4_1^+ state lifetime follows the rotational model estimate. The deduced lifetime under the first of these conditions is $\tau(2_1^+) = 4.6(8)$ ps, and is the value given in Table 5.10. Fig. 5.25 shows the fits.

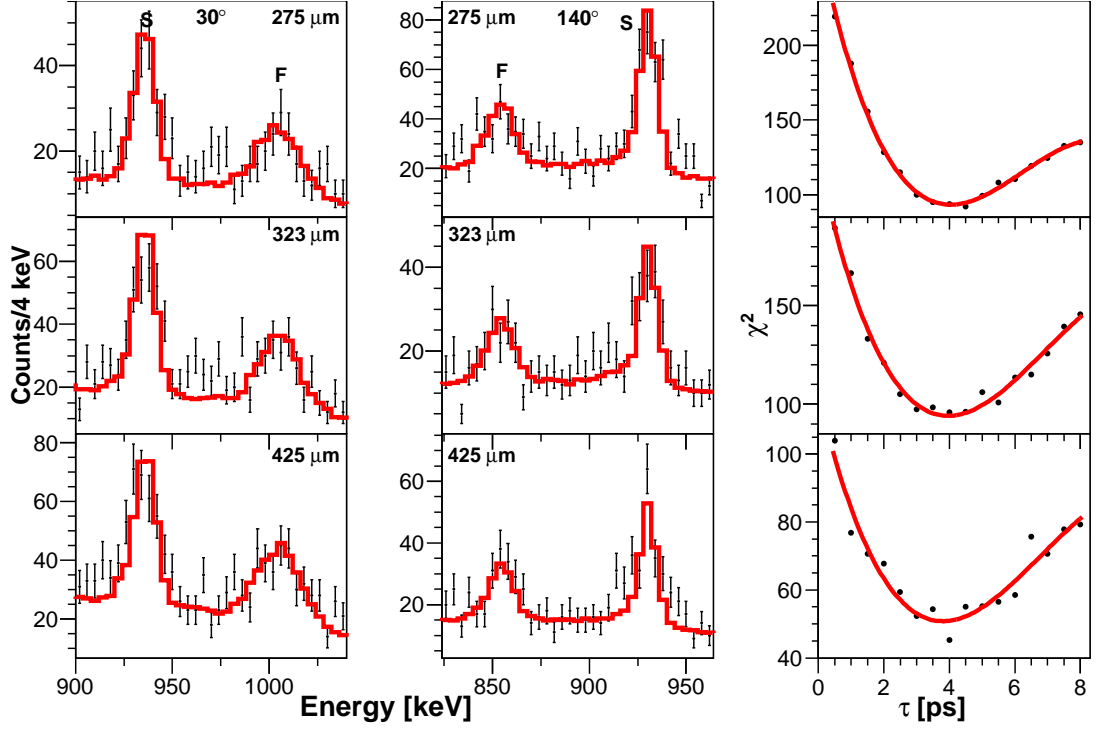


Figure 5.24: Left and centre columns: Experimental data (black points) and best-fit simulated lineshapes (red line) for the 934 keV $2_1^+ \rightarrow 0_{gs}^+$ transition in ^{70}Br at 30° (left) and 140° (centre) detector angles. Fast (F) and slow (S) peaks are labelled and correspond to decays before and after the degrader foil, respectively. Note that the simulated fit to 425 μm 140° data was not included in the analysis. Right column: χ^2 minimisation plots for the three distances shown.

Due to the very low statistics most of the fits failed to find a χ^2 minimum. Only data at forward angles/275 μm separation and backward angles/323 μm separation could be used. The corresponding $B(E2; 2_1^+ \rightarrow 0_{gs}^+)$ of 392(70) e^2fm^4 is in good agreement with the equivalent $B(E2; 2_1^+ \rightarrow 0_{gs}^+)$ in the literature of 432(58) e^2fm^4 obtained via a Coulex measurement (this has been converted from the $B(E2; 0_{gs}^+ \rightarrow 2_1^+)$ result given in Ref. [7]).

The rigid rotor estimate, discussed by Heyde [106], approximates the reduced transition strength of a $J + 2 \rightarrow J$ transition as

$$B(E2; J + 2 \rightarrow J) = \frac{5}{16\pi} Q_0^2 \frac{3}{2} \frac{(J + 1)(J + 2)}{(2J + 3)(2J + 5)} \quad (5.1)$$

where Q_0^2 is the intrinsic quadrupole moment given by the relation

$$Q_0^2 = \sqrt{\frac{16\pi}{5}} \frac{3}{4\pi} ZeR_0^2\beta \quad (5.2)$$

for a nucleus of charge Ze , mean radius R_0^2 and deformation β . Assuming deformation (and hence Q_0^2) remains constant for a rotational band, the ratio of reduced transition strengths for a feeding transition $J + 2 \rightarrow J$ and depopulating transition $J \rightarrow J - 2$ can be expressed as

$$\frac{(E2; J + 2 \rightarrow J)}{(E2; J \rightarrow J - 2)} = \frac{\frac{(J+1)(J+2)}{(2J+3)(2J+5)}}{\frac{(J-1)(J)}{(2(J-2)+3)(2(J-2)+5)}}. \quad (5.3)$$

The 4_1^+ state lifetime based on the rotational model estimate, given by Equation 5.3, is 1.0 ps. Using this assumed lifetime and the measured feeding intensity of 48%, the lifetime of the 2_1^+ state reduces to 4.0 ps, which lies within 1σ of the uncorrected value. This corresponds to a $B(E2; 2_1^+ \rightarrow 0_{gs}^+)$ of $450 \text{ e}^2\text{fm}^4$, which remains in very good agreement with the literature value [7].

One must assume that the depopulation of the 4_1^+ state is not delayed by higher-lying states. This assumption may not necessarily be valid as it is possible that higher-lying states are delaying the 4_1^+ state decay. Analysis of the target-only spectrum for ^{68}Se (see Section 5.3) revealed the presence of the known 1629 keV ($5_1^- \rightarrow 4_1^+$) transition, feeding the 4_1^+ state with a relative intensity of 52(37)%. It was not possible to extract a lifetime for the (5_1^-) state and no lifetime is known in the literature.

A thorough lifetime analysis of the 2_1^+ state in ^{68}Se would require the identification of the previously unobserved transitions in ^{68}Se and a determination of the lifetimes of the states from which they decay. Determining the lifetime of the previously unobserved states is important if it is discovered they decay through the 2_1^+ to the ground state. The lifetimes of these states would have a delaying effect on the 2_1^+ state lifetime, meaning that the result extracted in this work would be an overestimate.

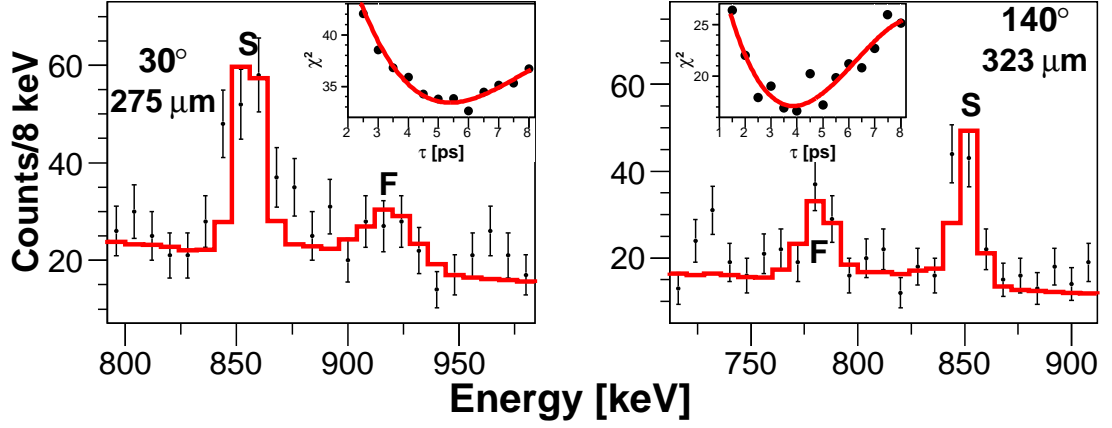


Figure 5.25: Experimental data (black points) and best-fit simulated lineshapes (red line) for the $2_1^+ \rightarrow 0_{gs}^+$ transition in ^{68}Se . Data are shown for forward angles/ $275 \mu\text{m}$ separation (left) and backward angles/ $323 \mu\text{m}$ separation (right). Fast (F) and slow (S) peaks are labelled and correspond to decays before and after the degrader foil, respectively. The inset to each spectrum shows the corresponding χ^2 minimisation plot.

5.2.4 ^{72}Kr

The ^{72}Kr 4_1^+ state lifetime could not be measured in this work due to the low statistics, therefore the literature lifetime of $\tau(4_1^+) = 3.5(7)$ ps is assumed [9]. This is believed to be a safe assumption as no transitions are observed to feed the 4_1^+ state in this work.

Only the forward ring data at target-degrader separations of $275 \mu\text{m}$ and $425 \mu\text{m}$ had sufficient statistics for a 2_1^+ lifetime to be measured (due to the longer run times - see Table 4.3). The fits to the backward angle data failed to find χ^2 minima. The successful fits are shown in Fig. 5.26. Even the successful fits show a weak sensitivity to the lifetime on the high-lifetime side of the χ^2 minima, therefore the lifetime results presented for the 2_1^+ state in ^{72}Kr have asymmetrical errors. The lifetime of the 2_1^+ state extracted in this work of $4.3_{-1.7}^{+2.3}$ ps gives a corresponding $B(E2; 2_1^+ \rightarrow 0_{gs}^+)$ of $1050_{-590}^{+420} \text{e}^2\text{fm}^4$, which is in agreement with the weighted average results from the literature of $\tau(2_1^+) = 4.9(5)$ ps / $B(E2; 2_1^+ \rightarrow 0_{gs}^+) = 919(98) \text{e}^2\text{fm}^4$ [8, 9].

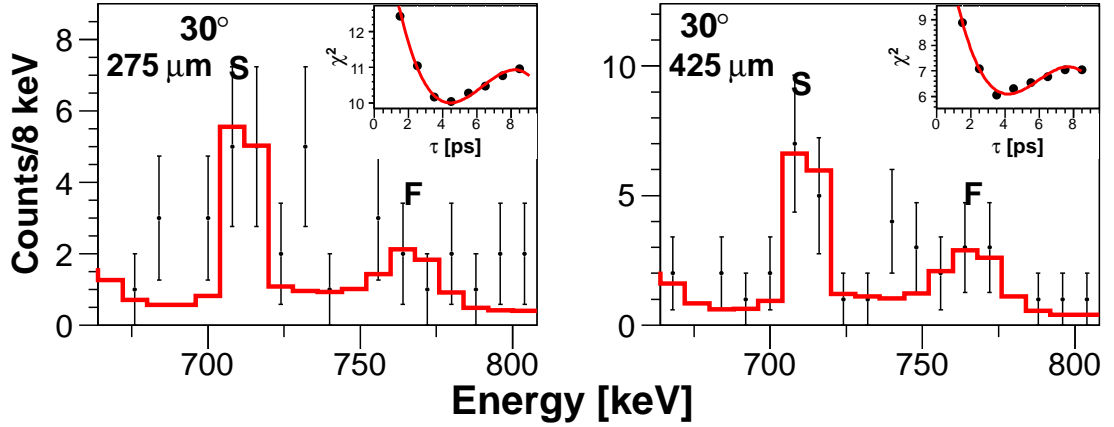


Figure 5.26: Experimental data (black points) and best-fit simulated lineshapes (red line) for the $2_1^+ \rightarrow 0_{gs}^+$ transition in ^{72}Kr . Data are shown for forward angles only at target-degrader separations of $275\ \mu\text{m}$ (left) and $425\ \mu\text{m}$ (right). Fast (F) and slow (S) peaks are labelled and correspond to decays before and after the degrader foil, respectively. The inset to each spectrum shows the corresponding χ^2 minimisation plot.

5.2.5 ^{70}Se

Lifetimes Of The Feeding States To The 2_1^+ State

The effective lifetime of the 4_1^+ state in ^{70}Se could only be determined via a fit to $323\ \mu\text{m}$ data. Data at the other two target-degrader separations yielded lifetimes in forward and backward SeGA rings that were inconsistent, differing by many standard deviations, whereas the $323\ \mu\text{m}$ data returned consistent results for both rings. It is unknown what caused this disagreement between the rings. It should be noted that, for $275\ \mu\text{m}$ and $425\ \mu\text{m}$ data, the 4_1^+ lifetime extracted from both SeGA rings averaged together was consistent with the $323\ \mu\text{m}$ result. It is not clear whether this was just coincidental, so the $275\ \mu\text{m}$ and $425\ \mu\text{m}$ data were not used for the determination of the effective lifetime of the 4_1^+ state. The effective lifetime extracted using a χ^2 fit was $4.38(37)$ ps - see Fig. 5.27. The large discrepancy between the measured effective lifetime and the literature 4_1^+ state lifetime ($1.4(1)$ ps [93]) arises due to feeding contributions to the 4_1^+ state from the higher-lying (5_2^-) state observed in this work (see Fig. 5.9), whose lifetime could not be measured due to insufficient statistics. An upper limit to the (5_2^-) state lifetime in the literature (≤ 12 ps [92]) suggests that this state potentially has a relatively long lifetime, helping to explain the large effective 4_1^+ lifetime measured in this work.

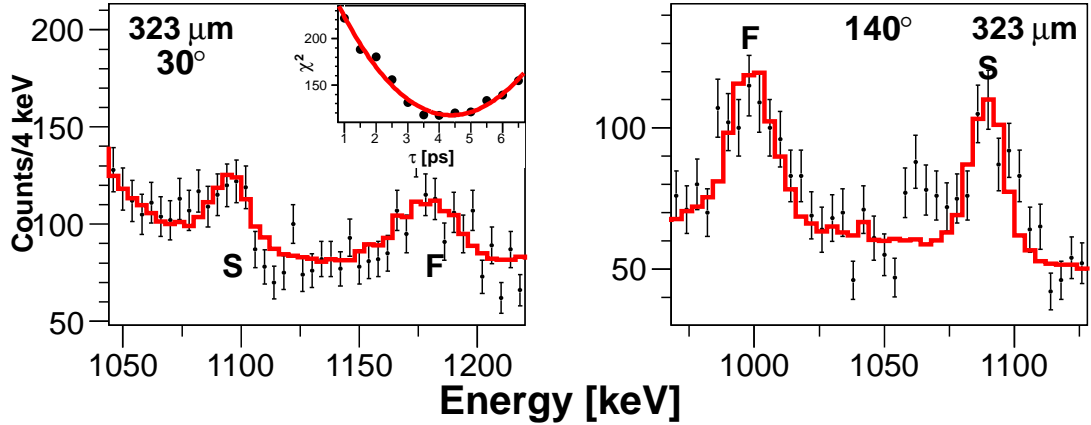


Figure 5.27: Experimental data (black points) and best-fit simulated lineshapes (red line) for the $4_1^+ \rightarrow 2_1^+$ transition in ^{70}Se . Data are shown for 30° (left) and 140° (right) detector angles at a target-degrader separation of $323 \mu\text{m}$. Fast (F) and slow (S) peaks are labelled and correspond to decays before and after the degrader, respectively. A second-order polynomial background was used in these spectra. The inset to the left figure shows the χ^2 minimisation plot for both angles.

Only one of the experimental γ spectra ($425 \mu\text{m}$ 140°) gave a successful χ^2 minimisation for the 2_2^+ state in ^{70}Se . The $2_2^+ \rightarrow 2_1^+$ RDDS peaks sat directly on the Compton edge of the $2_1^+ \rightarrow 0_{gs}^+$ RDDS peaks, making fits difficult to perform. A fit to the $425 \mu\text{m}$, backward angle spectrum gave a 2_2^+ state effective lifetime of $6.73(74)$ ps [92]. The previously published lifetime for this state is $4.8(13)$ ps [92]. The fit to the present data is shown in Fig. 5.28.

The $3_1^{(-)}$ state lifetime was difficult to extract as the 1574 keV peak overlapped with the 1600 keV $2_2^+ \rightarrow 0_{gs}^+$ transition. The relative intensities of these two convoluted peaks were extracted using fits of simulations with varying $2_2^+/3_1^{(-)}$ intensity to target-only data. The effective lifetime of the 2_2^+ state was determined from the $2_2^+ \rightarrow 2_1^+$ transition RDDS measurement. Therefore the only unknown parameter in the fits was the lifetime of the $3_1^{(-)}$ state. The lifetime extracted for the $3_1^{(-)}$ state in this work is $1.86(57)$ ps. The literature lifetime for this state is $6.1(9)$ ps [92]. The fits are shown in Fig. 5.29. Only the $275 \mu\text{m}$ data had sufficient statistics to allow a χ^2 fit. The other target-degrader distances did not successfully minimise, in part due to the complicated overlap of the γ rays and possibly in part due to the short lifetime of the $3_1^{(-)}$ state (the larger target-degrader distances may be insensitive to the $3_1^{(-)}$ state lifetime, i.e., beyond the lifetime region of sensitivity - see Subsection 3.3.1).

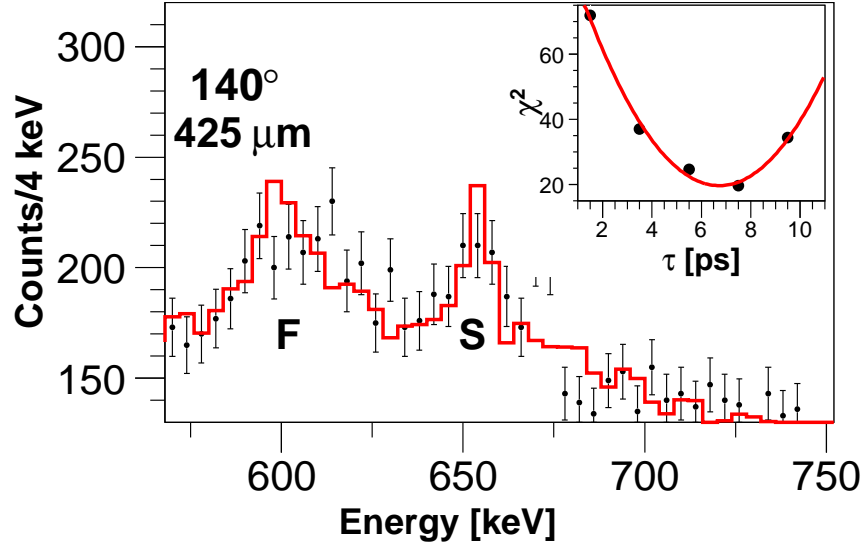


Figure 5.28: Experimental data (black points) and best-fit simulated lineshape (red line) for the $2_2^+ \rightarrow 2_1^+$ transition in ^{70}Se . Only data at $425 \mu\text{m}$ 140° had clean enough statistics for a lifetime to be extracted. Fast (F) and slow (S) peaks are labelled and correspond to decays before and after the degrader foil, respectively. The inset to the figure shows the χ^2 minimisation plot.

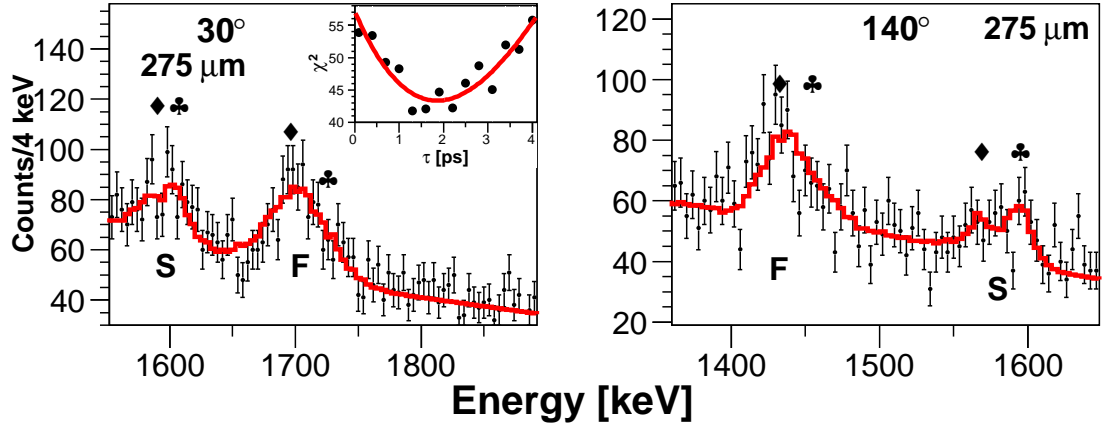


Figure 5.29: Experimental data (black points) and best-fit simulated lineshapes (red line) for the $3_1^{(-)} \rightarrow 2_1^+$ transition in ^{70}Se , labelled with diamonds. Data are shown for 30° (left) and 140° (right) at a target-degrader separation of $275 \mu\text{m}$. The $3_1^{(-)} \rightarrow 2_1^+$ RDDS peaks overlap with peaks corresponding to the $2_2^+ \rightarrow 0_{gs}^+$ transition (clubs). Fast (F) and slow (S) peaks are labelled and correspond to decays before and after the degrader foil, respectively. The inset to the left figure shows the χ^2 minimisation plot for both angles.

5.2. LIFETIME RESULTS

Table 5.9: Effective lifetimes of feeding states to the 2_1^+ state in ^{70}Se compared to their literature values. Both systematic and statistical errors are included (see Section 4.8 for details).

State	E_x [keV]	τ [ps] (Pres.)	τ [ps] (Lit.)
4_1^+	2038	4.38(37)	1.4(1) [†]
2_2^+	1600	6.73(74)	4.8(13) [‡]
$3_1^{(-)}$	2518	1.86(57)	6.1(9) [‡]

[†] from [93]; [‡] from [92].

The effective lifetimes of feeding states to the 2_1^+ state in ^{70}Se are listed in Table 5.9. As one can see from this table, the effective lifetimes of two of the states follow the expected trend of being longer than the literature lifetimes, since they are delayed by observed higher-lying feeding states (see Fig. 5.9). The $3_1^{(-)}$ state lifetime does not follow this trend. The literature value, however, comes from old data [92] which has since been shown to have suspect lifetimes [93]. It is possible that incorrect feeding information was assumed when extracting the lifetime of this state in the literature. The lifetime of the $3_1^{(-)}$ state has been quoted as an ‘effective’ lifetime in this work as any potential delay due to the higher-lying (5_2^-) state could not be taken into account.

2_1^+ State Lifetime

Figure 5.30 shows simulated fits used to extract the 2_1^+ state lifetime in ^{70}Se , following corrections for feeding. The resulting mean lifetime is $\tau(2_1^+) = 3.28(37)$ ps. This value and the corresponding $B(E2; 2_1^+ \rightarrow 0_{gs}^+)$ of $332(37)$ e²fm⁴ are in excellent agreement with the literature values of $\tau(2_1^+) = 3.2(2)$ ps and $B(E2; 2_1^+ \rightarrow 0_{gs}^+) = 342(19)$ e²fm⁴, respectively [93].

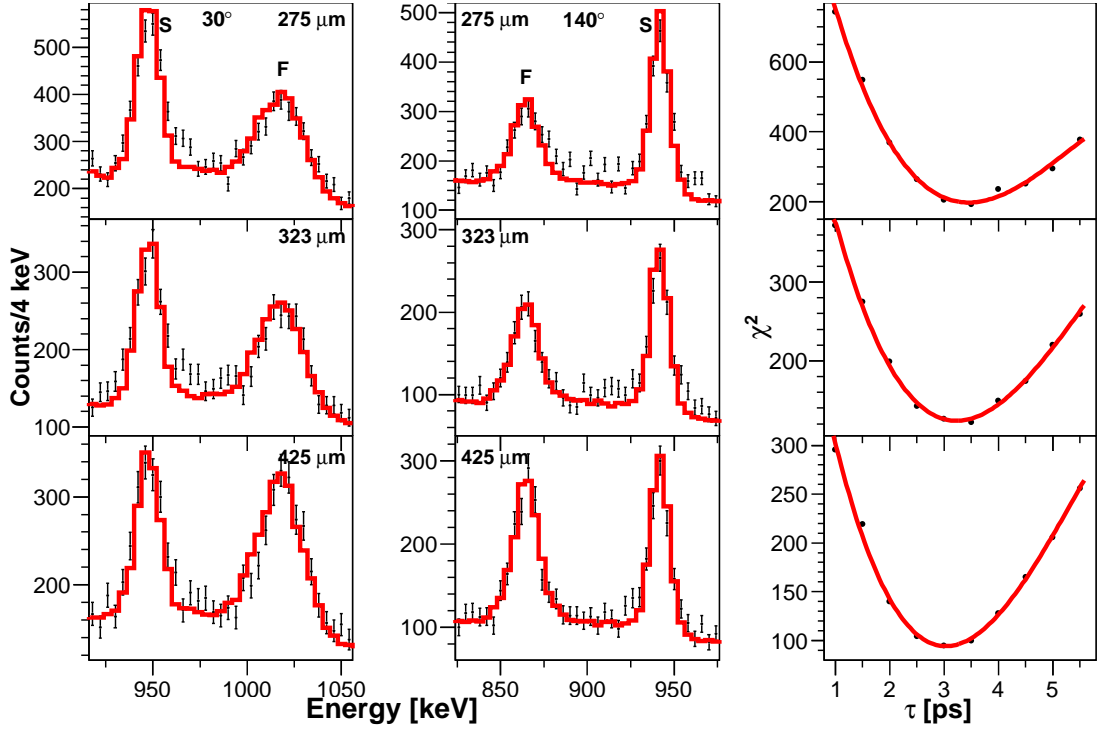


Figure 5.30: Left and centre columns: Experimental data (black points) and best-fit simulated lineshapes (red line) for the 945 keV $2_1^+ \rightarrow 0_{gs}^+$ transition in ^{70}Se at 30° (left) and 140° (centre) detector angles. Fast (F) and slow (S) peaks are labelled and correspond to decays before and after the degrader foil, respectively. Right column: χ^2 minimisation plots for the three distances shown.

5.2.6 ^{66}Ge

The 7_1^- state

The 7_1^- state in ^{66}Ge decays via the 521 keV γ ray to the $E_x = 3683$ keV 5_1^- state (see Fig. 5.12). The literature gives the lifetime of this state as 276(13) ps. The 7_1^- state is known in the literature to be fed by many states, however in the present work only the 338 keV $7_2^- \rightarrow 7_1^-$ transition was observed (with an intensity of 24(5)% relative to the $7_1^- \rightarrow 5_1^-$ transition). It was not possible to extract the lifetime of the 7_2^- state in this work due to low statistics, so instead the literature lifetime of 86(6) ps was assumed [95]. No states were observed to feed the 7_2^- state.

Only 275 μm and 425 μm distance spectra were used as these contained sufficient statistics for a χ^2 fit to successfully extract a lifetime, and of these only forward angle data were used due to the lack of lineshape sensitivity for long lifetimes at

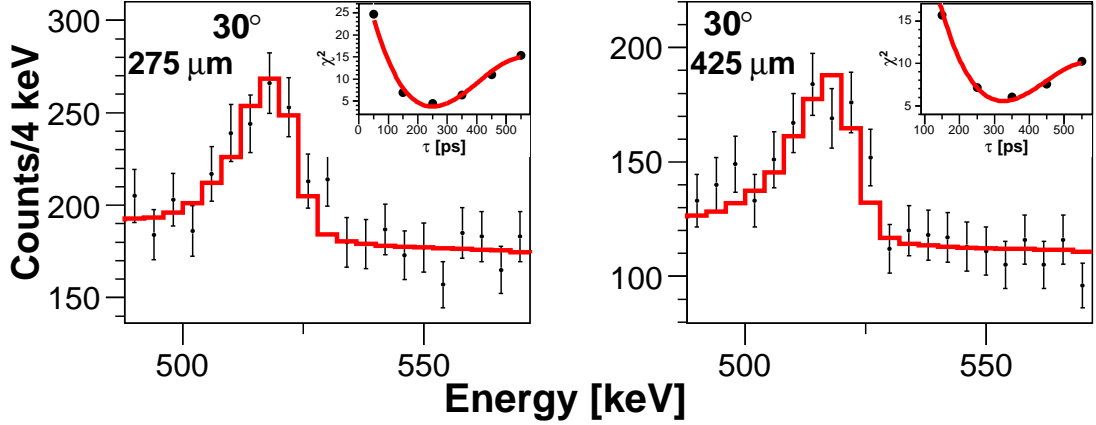


Figure 5.31: Experimental data (black points) and best-fit simulated lineshapes (red line) for the $7_1^- \rightarrow 5_1^-$ transition in ^{66}Ge . Data are shown for 30° SeGA detector angles at target-degrader separations of $275\ \mu\text{m}$ (left) and $425\ \mu\text{m}$ (right). The inset to each spectrum shows the corresponding χ^2 minimisation plot.

backward detector angles. The fits to the 7_1^- state, after corrections for feeding contributions, are shown in Fig. 5.31. The 7_1^- state lifetime in ^{66}Ge extracted in this work is $281(44)$ ps. This corresponds to a $B(\text{E}2; 7_1^- \rightarrow 5_1^-)$ of $76(12)$ e^2fm^4 . These results are in excellent agreement with the literature results of $\tau(7_1^-) = 276(13)$ ps / $B(\text{E}2; 7_1^- \rightarrow 5_1^-) = 77(4)$ e^2fm^4 [95].

The 2_1^+ state

The yrast 2^+ state in ^{66}Ge is fed by transitions from two states in this work, of which both were populated with sufficient intensity for effective lifetimes to be extracted. The effective lifetime of the 4_1^+ state, feeding the 2_1^+ state with a 49% intensity, was the easiest to extract due to the higher level of statistics. The fits are shown in Fig. 5.32 and give an effective lifetime of $2.57(22)$ ps for the 4_1^+ state. Note that the fit to the $275\ \mu\text{m}$ 30° data gave a result over three standard deviations away from the average of the other fits. The literature gives an upper limit to the absolute lifetime of this state of 2 ps [98]. The disagreement between the measured effective lifetime and the literature limit can be explained by the presence of feeding contributions to the 4_1^+ state, for which there is evidence in the target-only spectrum (see Fig. 5.11). The 5_1^- state and its higher-lying feeding states in particular have been shown in the literature to have relatively long lifetimes (see Table 5.6), which would significantly delay the decay of the 4_1^+ state. The overlapping of the 1510 keV $5_1^- \rightarrow 4_1^+$ transition

5.2. LIFETIME RESULTS

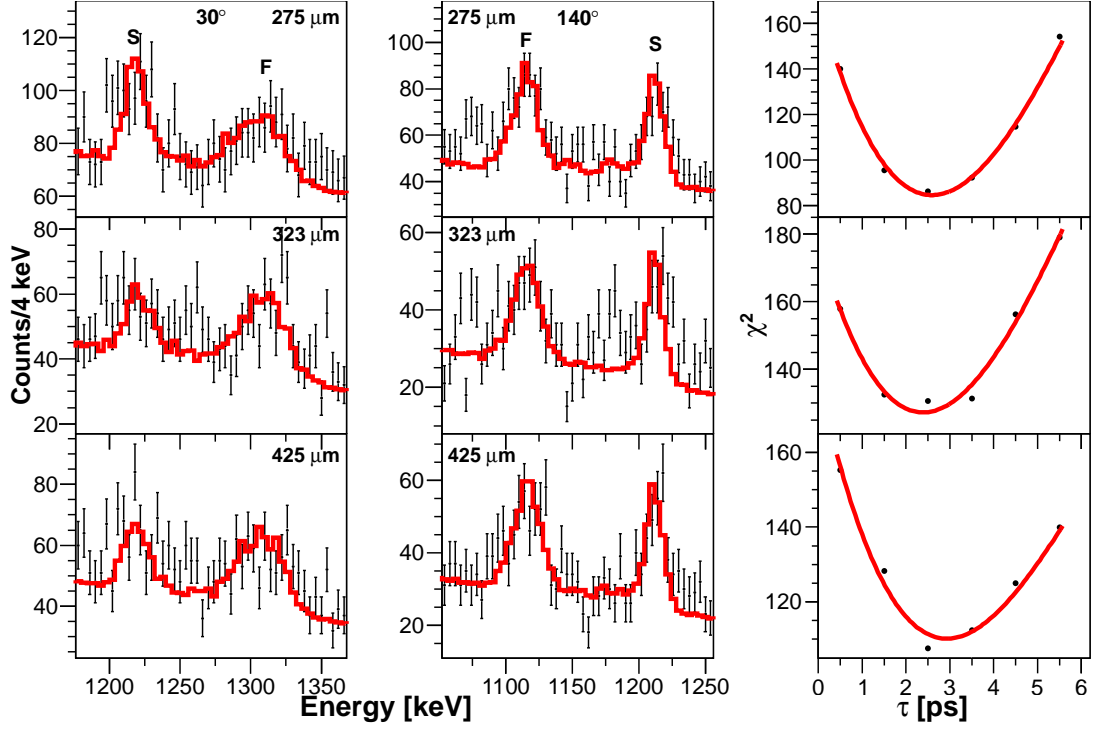


Figure 5.32: Left and centre columns: Experimental data (black points) and best-fit simulated lineshapes (red line) for the $4_1^+ \rightarrow 2_1^+$ transition in ^{66}Ge . Data are shown for 30° (left) and 140° (right) detector angles for target-degrader separations of $275\ \mu\text{m}$ (top), $323\ \mu\text{m}$ (middle) and $425\ \mu\text{m}$ (bottom). Fast (F) and slow (S) peaks are labelled and correspond to decays before and after the degrader foil, respectively. Right column: χ^2 minimisation plots for the three distances shown ($275\ \mu\text{m}$ 30° data were excluded - see text).

with the $6_1^+ \rightarrow 4_1^+$ transition at $1480\ \text{keV}$ made it impossible for the lifetimes of these states to be extracted.

The 2_2^+ feeding state, populating the yrast 2^+ state with a 19% intensity, was weakly populated and so it was not as straightforward to extract a lifetime. Only the $275\ \mu\text{m}$ distance experimental spectra had sufficient statistics. The fits are shown in Fig. 5.33 and returned an effective lifetime of $5.5(6)\ \text{ps}$. This agrees with the absolute lifetime in the literature ($6.5(25)\ \text{ps}$ [95]).

The fits to the 2_1^+ state, after corrections for feeding contributions, are shown in Fig. 5.34. The fits give a lifetime of $4.0(5)\ \text{ps}$ for the ^{66}Ge 2_1^+ state, corresponding to a $B(E2; 2_1^+ \rightarrow 0_{gs}^+)$ of $255(32)\ \text{e}^2\text{fm}^4$. These values are in good agreement with the weighted results of previous measurements in the literature ($\tau(2_1^+) = 3.68(17)\ \text{ps}$ / $B(E2; 2_1^+ \rightarrow 0_{gs}^+) = 277(13)\ \text{e}^2\text{fm}^4$ [95–97]).

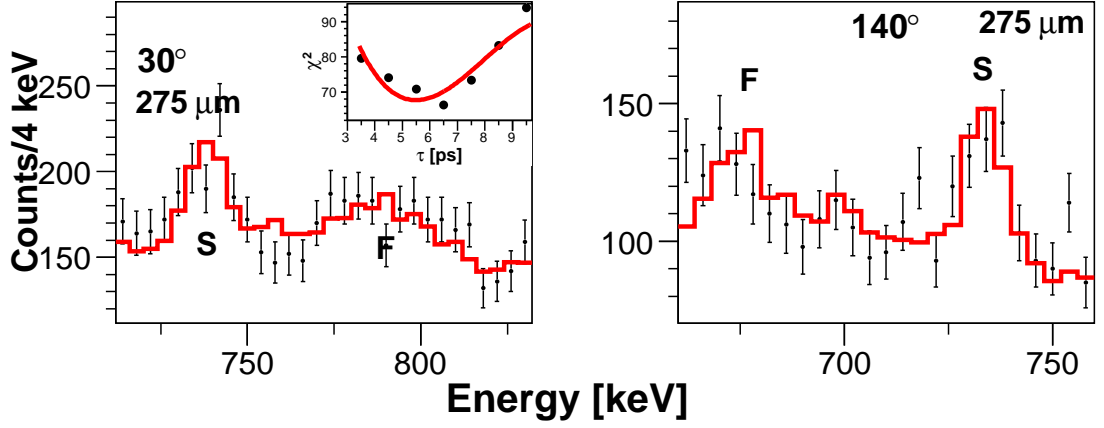


Figure 5.33: Experimental data (black points) and best-fit simulated lineshapes (red line) for the $2_2^+ \rightarrow 2_1^+$ transition in ^{66}Ge . Data are shown for 30° (left) and 140° (centre) detector angles at a target-degrader separation of $275 \mu\text{m}$. The inset to the left spectrum shows the χ^2 minimisation plot for both distances.

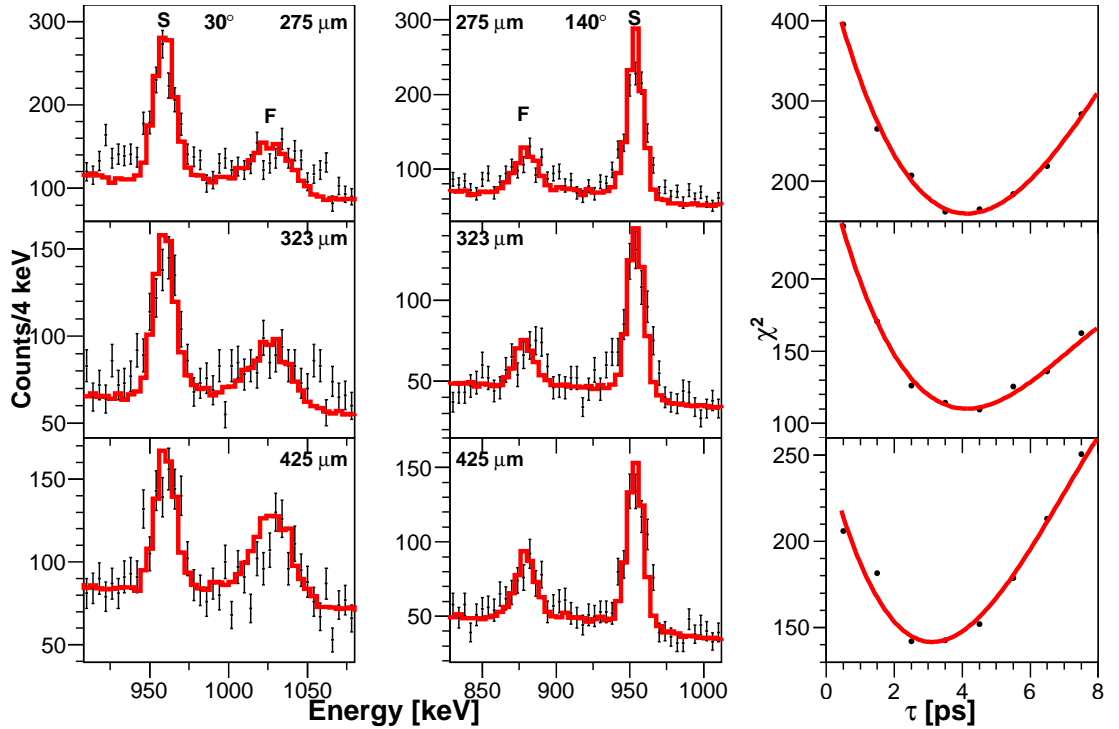


Figure 5.34: Left and centre columns: Experimental data (black points) and best-fit simulated lineshapes (red line) for the $2_1^+ \rightarrow 0_{gs}^+$ transition in ^{66}Ge . Data are shown for forward and backward angles (left and right panels, respectively) for the three target-degrader distances $275 \mu\text{m}$ (top), $323 \mu\text{m}$ (middle) and $425 \mu\text{m}$ (bottom). Right column: χ^2 minimisation plots for the three distances shown.

5.2.7 ^{69}Se

Lifetime analysis of the low-lying excited states in ^{69}Se was performed using target-only data, not the ‘distance’ data. This decision was made because the γ -ray energies of the state de-excitations were quite low (100-250 keV) and so were very close to the SeGA energy threshold. It was therefore difficult to accurately fit the background below the ^{69}Se transitions with distance data. Furthermore, in the distance runs, the lowest energy γ transitions (90 keV, 129 keV) were Doppler shifted below the SeGA energy threshold at backward angles and so do not appear. This problem is not present in the target-only runs due to the lower SeGA energy threshold used. For forward ring data an exponential curve was fit to the background. For backward ring data, a combination of second-order polynomial and exponential was used to replicate the background. As stated before, it was found that the backward ring SeGA γ -ray lineshapes were much less sensitive to changes in lifetime compared to the forward ring data. Nevertheless, it was possible to extract lifetimes from both forward and backward ring data.

Feeding Transitions To The $\frac{3}{2}_1^-$ State

The yrast $\frac{3}{2}^-$ state at an excitation energy of 129 keV is fed in this work by two transitions. The strongest of these transitions is the 161 keV transition from the known $\frac{3}{2}_2^-$ state, feeding with 51(3)% intensity relative to the 129 keV $\frac{3}{2}_1^- \rightarrow \frac{1}{2}_{gs}^-$ transition (see Figs. 5.13/5.14 and Table 5.7). Note that this corresponds to a *level feeding intensity* of 38(5)%, as one must account for the intensities of all depopulating transitions (in this case, both the 129 keV and the 90 keV transitions) when describing level feeding intensities. The yrast $\frac{3}{2}^-$ state in ^{69}Se is the only level studied in this work where this distinction between γ intensity and level feeding intensity needs to be made, as almost all other states studied in this work have only one depopulating transition. The $\frac{3}{2}_2^-$ state also decays via the 251 keV transition to the $\frac{5}{2}_1^-$ state. This allowed the determination of the $\frac{3}{2}_2^-$ state lifetime via simulated fits to two γ decays. The $\frac{3}{2}_2^-$ state is believed to be fed by the 500 keV transition, identified for the first time in this work, with an intensity of 11(1)% relative to the 129 keV $\frac{3}{2}_1^- \rightarrow \frac{1}{2}_{gs}^-$ transition (see Table 5.7). It was not possible to identify the lifetime of the unknown state. Lifetime analysis was performed assuming 100% direct population of the $\frac{3}{2}_2^-$ state.

5.2. LIFETIME RESULTS

The lifetime of the $\frac{3}{2}^-$ state was obtained from the weighted mean of fits to both the 161 keV and the 251 keV transitions, since the lifetimes extracted should be the same for both (as both γ rays originate from the same state). It is assumed that the extracted lifetime of the $\frac{3}{2}^-$ state represents the actual lifetime, i.e., that feeding contributions have a negligible effect. The lifetime of the $\frac{3}{2}^-$ state extracted from the weighted mean of fits to the 161 keV transition (target-only data) is 325(16) ps. The lifetime extracted from the weighted mean of fits to the 251 keV transition is 360(28) ps. These two results are in reasonable agreement with each other. The lifetime of the $\frac{3}{2}^-$ state extracted in this work is therefore 332(15) ps (from the weighted mean of the two results above).

Stefanescu *et al.* extracted a DCO ratio for the 161 keV $\frac{3}{2}^- \rightarrow \frac{3}{2}^-$ transition and determined it was pure dipole in character [101]. Therefore the $B(M1\downarrow)$ for this transition was determined to be 0.041(2) μ_N^2 . Similar DCO measurements for the 251 keV $\frac{3}{2}^- \rightarrow \frac{5}{2}^-$ transition revealed a mixed M1/E2 character. If one assumes the transition is pure dipole in character, the corresponding reduced transition strength is $B(M1\downarrow) = 0.0099(8) \mu_N^2$. If instead a pure E2 transition is assumed, the corresponding reduced transition strength is $B(E2\downarrow) = 2280(180) e^2\text{fm}^4$.

The $\frac{3}{2}^-$ state in ^{69}Se was also observed to be fed by a 786 keV transition from the $\frac{7}{2}^-$ state with an intensity of 14(1)% relative to the $\frac{3}{2}^- \rightarrow \frac{3}{2}_{gs}^-$ decay (see Figs. 5.13/5.14 and Table 5.7). This corresponds to a level feeding intensity of 11(1)%. No feeding states to the $\frac{7}{2}^-$ state were observed. Transitions from the $\frac{7}{2}^-$ state only exhibited ‘fast’/‘slow’ RDDS components at the largest target-degrader distance (4.275 mm), indicating a $\frac{7}{2}^-$ lifetime on the order of tens of picoseconds. Statistics were not sufficient to extract a lifetime for this state. The lifetime of the $\frac{3}{2}^-$ state was analysed assuming a negligible $\frac{7}{2}^-$ state lifetime.

The $\frac{3}{2}^-$ State

The $\frac{3}{2}^-$ state was observed to decay to the $\frac{1}{2}^-$ ground state via the 129 keV transition and to the $\frac{5}{2}^-$ state via the 90 keV transition (see Figs. 5.13/5.14 and Table 5.7). The lifetime of the $\frac{3}{2}^-$ state was extracted from simulated fits to the 129 keV $\frac{3}{2}^- \rightarrow \frac{1}{2}_{gs}^-$ transition using target-only data. The lifetime deduced from these fits is 380(18) ps. The fits for this transition, and other transitions in ^{69}Se analysed in this section,

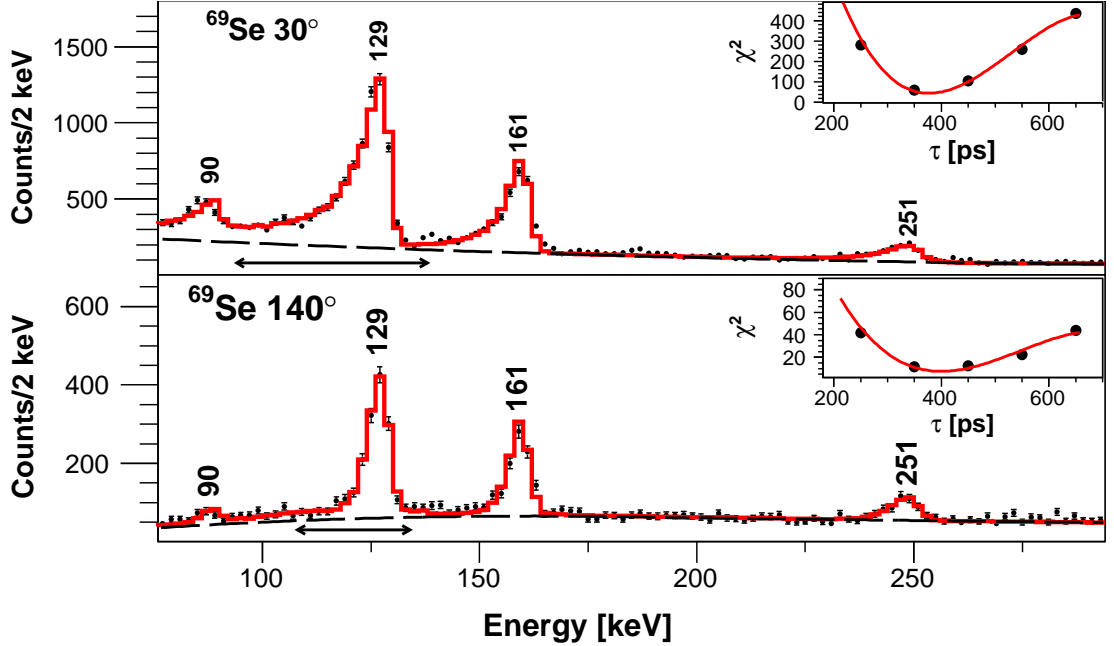


Figure 5.35: Doppler-shift corrected target-only γ -ray spectra obtained for ^{69}Se for forward (top) and backward (bottom) SeGA angles. The simulated fits to the γ spectra are shown (red line). The background fits are shown (dashed black lines). Arrows denote the region of lifetime sensitivity used in the extraction of the 129 keV $\frac{3}{2}^-$ state. The insets to the spectra show the corresponding χ^2 minimisation plots for the ^{69}Se 129 keV state lifetime determination.

are shown in Fig. 5.35. The lifetime extracted from a fit to the 90 keV transition is 446(72) ps. A zoomed-in version of Fig. 5.35 showing the area around the 90 keV peak is given in Fig. 5.36. The fit does not appear satisfactory, with a clear centroid mismatch between experiment and simulation. Whilst increasing the lifetime of the state in the simulation would shift the simulated peak centroid down in line with the data, this would create a much larger γ energy tail than is seen experimentally. The energy of the γ ray is known to high precision in the literature: 90.3(1) keV [101]. Despite the poor fit, the extracted result of 446(72) ps is consistent with the 380(18) ps result obtained from fits to the 129 keV transition. Including the 90 keV target-only result makes a difference of less than a picosecond to the lifetime extracted using the 129 keV transition fits when taking the weighted mean, and so it has not been included in the weighted mean result of the $\frac{3}{2}^-$ state lifetime.

DCO measurements for the 129 keV $\frac{3}{2}^- \rightarrow \frac{1}{2}_{gs}^-$ transition indicate a mixed E2/M1 character [101]. If one assumes the transition is pure M1 in character, the reduced transition strength is $B(\text{M1}\downarrow) = 0.069(3) \mu_N^2$. If instead a pure E2 transition is

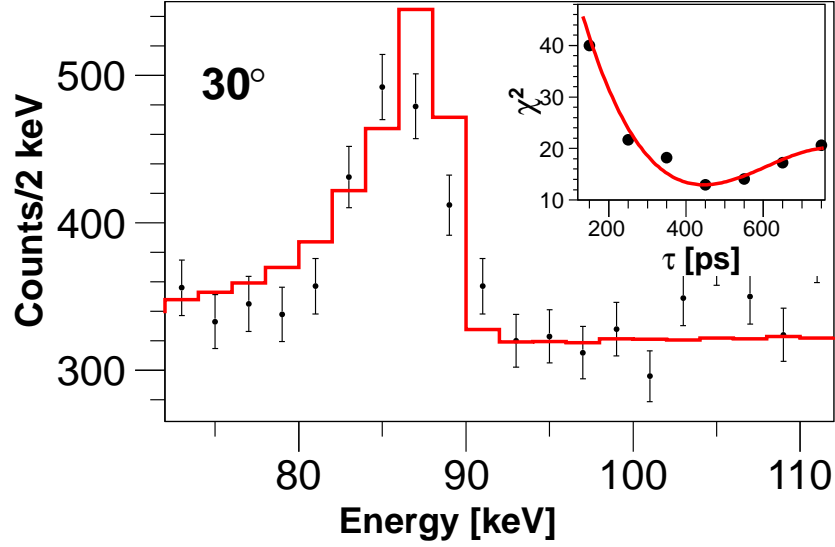


Figure 5.36: Experimental data (black points) and best-fit simulated lineshape (red line) for the $\frac{3}{2}^- \rightarrow \frac{5}{2}^-$ transition in ^{69}Se . 30° target-only data are shown. The inset shows the corresponding χ^2 minimisation plot.

assumed, the reduced transition strength is $B(E2\downarrow) = 60200(2800) e^2\text{fm}^4$. This is an unrealistically large $B(E2\downarrow)$ value, suggesting that the transition is closer to pure dipole in character than pure quadrupole. The 90 keV $\frac{3}{2}^- \rightarrow \frac{5}{2}^-$ transition has also been shown to have a mixed E2/M1 nature [101]. Taking the lifetime of the $\frac{3}{2}^-$ state as 380 ps, and assuming the transition is pure dipole in character, the corresponding reduced transition strength is $B(M1\downarrow) = 0.20(1) \mu_N^2$. If instead a pure E2 transition is assumed, the corresponding reduced transition strength is $B(E2\downarrow) = 364000(17000) e^2\text{fm}^4$. Again, this is unrealistically large and suggests that the transition is closer to pure dipole in nature.

5.2.8 ^{65}Ga

Just as with ^{69}Se , the largest γ -ray transition in ^{65}Ga sat at very low energy and so distance data could not be reliably used to extract a lifetime. Target-only data were used instead. As with ^{69}Se , an exponential was used to fit the background for forward SeGA ring data, and a combination of second-order polynomial and exponential was used to fit the backward ring background.

Due to the complication of the ^{65}Ga level scheme it was only possible to measure the

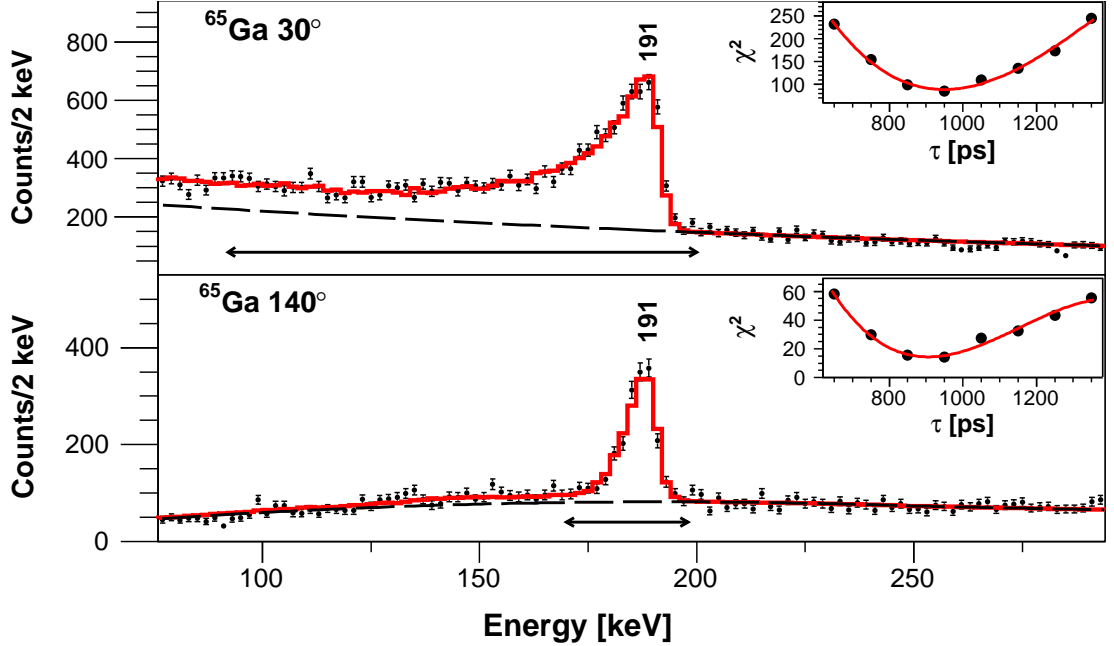


Figure 5.37: Doppler-shift corrected target-only γ -ray spectra obtained for ^{65}Ga for forward (top) and backward (bottom) SeGA angles. The simulated fits to the γ spectra are shown (red line). The background fits are shown (dashed black lines). Arrows denote the region of lifetime sensitivity used in the extraction of the 191 keV $\frac{5}{2}^-$ state. The insets to the spectra show the corresponding χ^2 minimisation plots for the ^{65}Ga 191 keV state lifetime determination.

lifetime the $\frac{5}{2}^-$ state, which decays via the 191 keV transition (see Figs. 5.17/5.18 and Table 5.8). The state was observed to be fed by the 885 keV transition from the known $\frac{7}{2}^-$ state and the 1096 keV transition from the known $(\frac{9}{2})_1^-$ state. The $\frac{7}{2}^-$ state feeds with a small intensity (6(2)% relative to the 191 keV intensity) and so its feeding contribution was considered negligible. The $(\frac{9}{2})_1^-$ state appeared to have a larger feeding contribution than the $\frac{7}{2}^-$ state (47(9)% relative to the 191 keV decay) and a previously measured upper lifetime limit of ≤ 2.0 ps is quoted in the literature [105]. This feeding contribution, despite its large intensity, is negligible as the yrast $\frac{5}{2}^-$ state lifetime is approximately two orders of magnitude longer (see below).

For this analysis the ^{65}Ga experimental γ spectra from the two secondary beams ^{70}Se and ^{69}As were added together. The $\frac{5}{2}^-$ state mean lifetime from fits to the target-only data is 938(34) ps. This is consistent with the literature lifetime limit of ≤ 1010 ps [105]. Assuming a pure dipole transition, a feature supported by angular distribution of oriented states measurements for the $\frac{5}{2}^- \rightarrow \frac{3}{2}_{gs}^-$ transition [107], gives a

corresponding reduced transition strength of $B(M1; \frac{5}{2}_1^- \rightarrow \frac{3}{2}_{gs}^-) = 0.0086(3) \mu_N^2$. This is consistent with the lower limit in the literature of $\geq 0.0080 \mu_N^2$ [105].

5.2.9 Summary Of Lifetime Results

The lifetimes of excited states extracted in this work are summarised in Table 5.10. Reduced transition strengths are also quoted where possible. Both statistical and systematic uncertainties are quoted (see Section 4.8). Also included for comparison in Table 5.10, where possible, are literature results.

5.2. LIFETIME RESULTS

Table 5.10: Experimental results for excited state mean lifetimes in all recoils studied in this work. Reduced transition strengths are also quoted where possible. Both present (Pres.) and literature (Lit.) values are shown. Errors quoted in the table include both statistical and systematic effects (see Section 4.8).

Nucleus	E_γ [keV]	E_x [keV]	Observable	Pres.	Lit.	Unit
^{72}Kr	709.72(14)	710	$\tau_{2_1^+}$	$4.3_{-1.7}^{+2.4}$	4.9(5) [♠]	ps
^{70}Br	320.7(3)	1657	$\tau_{5_1^+}$	540(120)	-	ps
^{70}Br	402.6(3)	1336	$\tau_{3_1^+}$	32(15)	-	ps
^{70}Br	933.6(3)	934	$\tau_{2_1^+}$	3.96(58)	-	ps
^{70}Se	944.51(5)	945	$\tau_{2_1^+}$	3.28(37)	3.2(2) [†]	ps
^{68}Se	853.8(2)	854	$\tau_{2_1^+}$	4.6(8)	4.2(7) [‡]	ps
^{66}Ge	521.4(2)	4205	$\tau_{7_1^-}$	281(44)	276(13) [♣]	ps
^{66}Ge	956.9(1)	957	$\tau_{2_1^+}$	4.0(5)	3.68(17) [*]	ps
^{69}Se	129.1(2)/ 90.3(1)	129 129	$\tau_{\frac{3}{2}1^-}$	380(18)	-	ps
^{69}Se	161.3(4)/ 250.7(2)	290 290	$\tau_{\frac{3}{2}2^-}$	332(15)	-	ps
^{65}Ga	190.8(2)	191	$\tau_{\frac{5}{2}1^-}$	938(34)	≤ 1010 [♡]	ps
^{72}Kr	709.72(14)	710	$B(E2; 2_1^+ \rightarrow 0_{gs}^+)$	1050_{-590}^{+420}	919(98) [♠]	e^2fm^4
^{70}Br	320.7(3)	1657	$B(E2; 5_1^+ \rightarrow 3_1^+)$	450(100)	-	e^2fm^4
^{70}Br	402.6(3)	1336	$B(M1; 3_1^+ \rightarrow 2_1^+)$	0.027(13)	-	μ_N^2
^{70}Br	933.6(3)	934	$B(E2; 2_1^+ \rightarrow 0_{gs}^+)$	291(43)	-	e^2fm^4
^{70}Se	944.51(5)	945	$B(E2; 2_1^+ \rightarrow 0_{gs}^+)$	332(37)	342(19) [†]	e^2fm^4
^{68}Se	853.8(2)	854	$B(E2; 2_1^+ \rightarrow 0_{gs}^+)$	392(70)	432(58) [‡]	e^2fm^4
^{66}Ge	521.4(2)	4205	$B(E2; 7_1^- \rightarrow 5_1^-)$	76(12)	77(4) [♣]	e^2fm^4
^{66}Ge	956.9(1)	957	$B(E2; 2_1^+ \rightarrow 0_{gs}^+)$	255(32)	277(13) [*]	e^2fm^4
^{69}Se	161.3(4)	290	$B(M1; \frac{3}{2}2^- \rightarrow \frac{3}{2}1^-)$	0.041(2)	-	μ_N^2
^{65}Ga	190.8(2)	191	$B(M1; \frac{5}{2}1^- \rightarrow \frac{3}{2}2^-)$	0.0086(3)	≥ 0.0080 [♡]	μ_N^2

♠ [8, 9]; † [93]; ‡ [7]; ♣ [96, 98]; * [95–97]; ♡ [105].

Chapter 6

Discussion

6.1 Collectivity In $N = Z$, $A \sim 70$ Nuclei

The $N = Z$, $A \sim 70$ region of the nuclide chart is predicted to exhibit a rapid increase in collectivity due to valence nucleons beginning to occupy the deformation-driving $g_{\frac{9}{2}}$ orbital. The main aspect of the present work focuses on self-conjugate ^{70}Br in an attempt to define the precise location along the $N = Z$ line where low-spin collectivity starts to rapidly increase. In this work the ^{70}Br $B(E2; 2_1^+ \rightarrow 0_{gs}^+)$ value was deduced to be $291(43) \text{ e}^2\text{fm}^4$, and the ^{68}Se $B(E2; 2_1^+ \rightarrow 0_{gs}^+)$ value was deduced to be $432(58) \text{ e}^2\text{fm}^4$ [7]. The $B(E2\downarrow)$ result for ^{68}Se is consistent with the literature $B(E2\uparrow)$ value for the $0_{gs}^+ \rightarrow 2_1^+$ transition [7]. The collectivity results for ^{70}Br and ^{68}Se suggest that the jump in low-spin collectivity in $N = Z$ nuclei does not occur at ^{70}Br . In fact, instead of an increase in collectivity relative to ^{68}Se , what is in fact observed is a relative decrease in collectivity at ^{70}Br . The lifetime of the 2_1^+ state in ^{72}Kr extracted in this work is $\tau(2_1^+) = 4.3_{-1.7}^{+2.4}$, which gives a corresponding $B(E2; 2_1^+ \rightarrow 0_{gs}^+)$ of $1050_{-590}^{+420} \text{ e}^2\text{fm}^4$. The present work cannot confirm the jump in collectivity at ^{72}Kr due to the large error, but the absolute value extracted is consistent with previous work ($919(98) \text{ e}^2\text{fm}^4$ [8, 9]).

Figure 6.1 shows all previous known $B(E2; 2_1^+ \rightarrow 0_{gs}^+)$ values for $N = Z$ nuclei in the $A = 64-70$ range (black squares). Included on this plot are the present results obtained for ^{68}Se , ^{70}Br and ^{72}Kr (red stars). The low-spin $B(E2\downarrow)$ systematics for

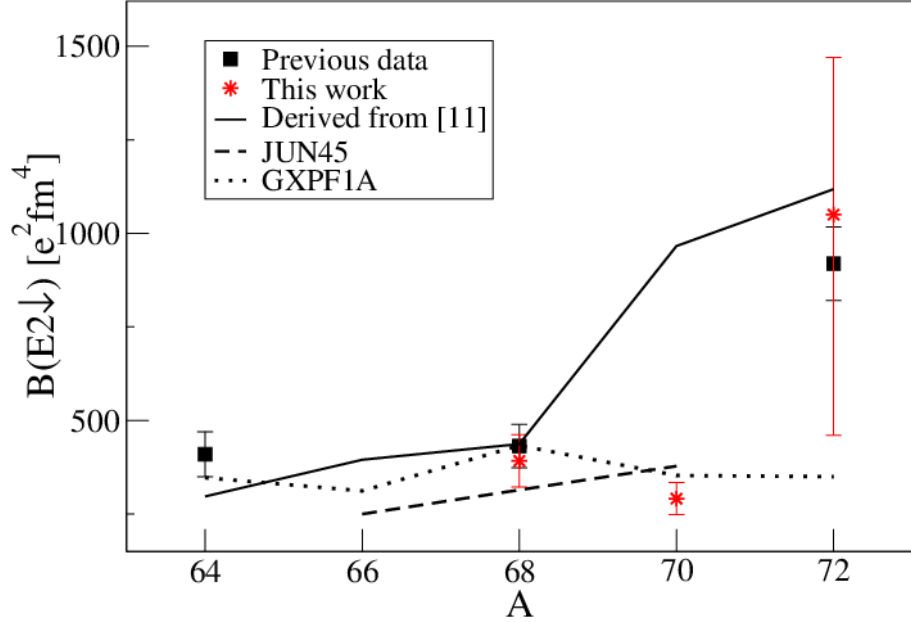


Figure 6.1: Experimental values of $B(E2; 2_1^+ \rightarrow 0_{gs}^+)$ for $N = Z$ nuclei [6–9] (black squares) compared to $B(E2\downarrow)$ values deduced in this work from calculated deformation parameters [11] (solid line). Also shown are large-scale shell model calculations using the JUN45 interaction in the $f_{5/2}pg_{9/2}$ model space (dashed line) and using the GXPF1A interaction in the fp model space (dotted line). The results obtained in this work are shown by red stars.

$N = Z$ nuclei shown in Fig. 6.1 are compared to predictions derived from deformation parameters calculated using the finite-range droplet macroscopic model and the folded Yukawa single-particle microscopic model [11] (solid line). $B(E2\downarrow)$ values from this model were deduced by the author from the deformation parameters (β_2) by assuming a rigid rotor model. The theoretical $B(E2)$ values extracted under this assumption reproduce the overall trend well but predict a sharp increase in collectivity at ^{70}Br , which is not supported by the present experimental results.

Fig. 6.1 compares the present data with shell model calculations performed using the GXPF1A interaction [29] in the fp model space (including the $f_{7/2}$ orbit) and the JUN45 interaction [28] in the $f_{5/2}pg_{9/2}$ model space (no $f_{7/2}$ orbit). The shell model calculations were performed by K. Kaneko (see Section 2.1.2) and published in Ref. [108]. Coulomb, spin-orbit and isospin non-conserving (INC) interactions were included in the calculations, further details of which can be found in Refs. [21–23]. Parameters for the INC interaction were taken from Ref. [109] for the fp model space and from [21] for the $f_{5/2}pg_{9/2}$ model space. Standard effective charges of 1.5e

and $0.5e$ were used for the protons and neutrons, respectively. The calculations performed with the GXPF1A interaction and the fp model space yield the best agreement with the experimental $B(E2\downarrow)$ values deduced for ^{68}Se and ^{70}Br , both in terms of trend and absolute values, but not ^{72}Kr . The level of agreement between the data and the GXPF1A calculations suggests that the $g_{\frac{9}{2}}$ orbital is not important for describing the low-lying states in ^{68}Se and ^{70}Br . However, it would be significant for ^{72}Kr because the calculated $B(E2\downarrow)$ value, using this interaction, of $350 e^2\text{fm}^4$ cannot reproduce the rapid enhancement at $A = 72$ seen in Fig. 6.1. Calculations using the JUN45 interaction in an $f_{\frac{5}{2}}pg_{\frac{9}{2}}$ model space fail to replicate the decrease in collectivity in ^{70}Br relative to ^{68}Se , although the absolute values are still well replicated. No calculations using the JUN45 interaction in the $f_{\frac{5}{2}}pg_{\frac{9}{2}}$ model space have been made for ^{72}Kr in Fig. 6.1 due to the excessively large model space, and consequently large amount of computing time, required to make the calculation. All calculations were repeated without the INC interaction. This resulted in virtually no change to the predicted $B(E2\downarrow)$ values.

The $B(E2\downarrow)$ values for ^{68}Se and ^{70}Br tentatively suggest a staggering in collectivity between even-even and odd-odd $N = Z$ nuclei in this region. Since the current work provides the first measurement of a 2_1^+ state lifetime in an odd-odd $N = Z$ nucleus around $A \sim 70$, it is not yet clear if this is a significant feature. Clearly, measurements of other neighbouring odd-odd nuclei such as ^{66}As and ^{74}Rb will be important in establishing whether staggering of the $B(E2:2_1^+ \rightarrow 0_{gs}^+)$ values between even-even and odd-odd $N = Z$ nuclei is a regular feature in this region.

From a theoretical perspective, it is possible that the staggering pattern results from the presence of two $\mathbf{T} = 0$ monopole attractions between the $\pi f_{\frac{7}{2}}$, $\nu f_{\frac{5}{2}}$ and $\pi p_{\frac{3}{2}}$, $\nu p_{\frac{1}{2}}$ orbitals, respectively [111]. The monopole attractions between these orbital pairs are stronger than those of other monopole matrix elements (see [29, 111] and Fig. 6.2), which impacts on the effective single-particle energies (see Fig. 6.3). The strong monopole attraction between the $p_{\frac{1}{2}}$ and $p_{\frac{3}{2}}$ orbitals acts to drastically decrease their energy. Furthermore, for ^{66}As and ^{68}Se , the Fermi energy lies between the $f_{\frac{5}{2}}$ and $p_{\frac{1}{2}}$ orbitals. The strong monopole attraction between the $f_{\frac{5}{2}}$ and $f_{\frac{7}{2}}$ orbitals therefore does not affect the $f_{\frac{5}{2}}$ as it is not occupied at $A = 68$. This leads to a large energy gap between the $p_{\frac{1}{2}}$ and $f_{\frac{5}{2}}$ orbitals near $A = 68$. Excitations to the $f_{\frac{5}{2}}$ orbital become maximum at ^{68}Se , which is shown by a drastic increase of the $f_{\frac{5}{2}}$ occupation number (see Fig. 6.4). The excitations from the $pf_{\frac{7}{2}}$ orbitals to the

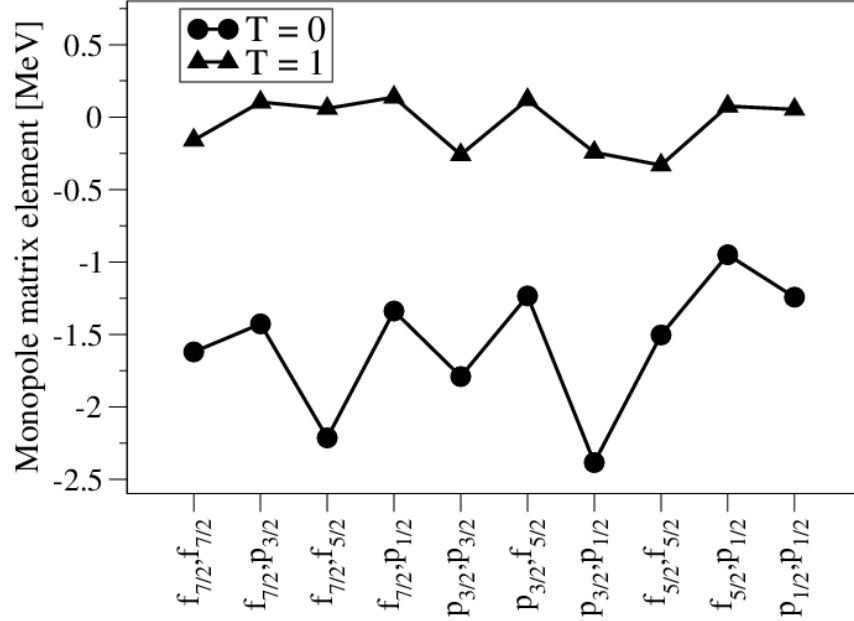


Figure 6.2: Theoretical monopole matrix elements from shell model calculations using the GXPF1A interaction (courtesy of K. Kaneko [110]). $\mathbf{T} = 0$ (circles) and $\mathbf{T} = 1$ (triangles) predictions are shown. The shell model calculations predict strong $\pi f_{7/2}^+$, $\nu f_{5/2}^+$ and $\pi p_{3/2}^+$, $\nu p_{1/2}^+$ matrix elements. See text for details.

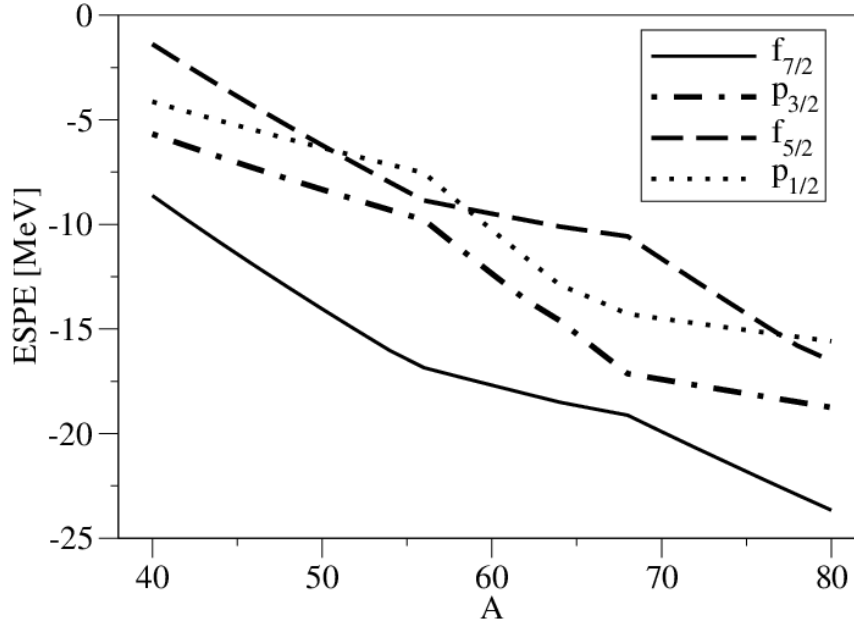


Figure 6.3: Theoretical single-particle energies for $N = Z$ nuclei in the $A = 40$ -80 region extracted from shell model work by K. Kaneko [110]. The $f_{5/2}^+$ orbital (dashed line) is maximally separated from the $p_{7/2}^+$ orbitals at $A = 68$, which is an effect caused by the presence two $\mathbf{T} = 0$ monopole attractions between the $\pi f_{7/2}^+$, $\nu f_{5/2}^+$ and $\pi p_{3/2}^+$, $\nu p_{1/2}^+$ orbitals, respectively (see Fig. 6.2).

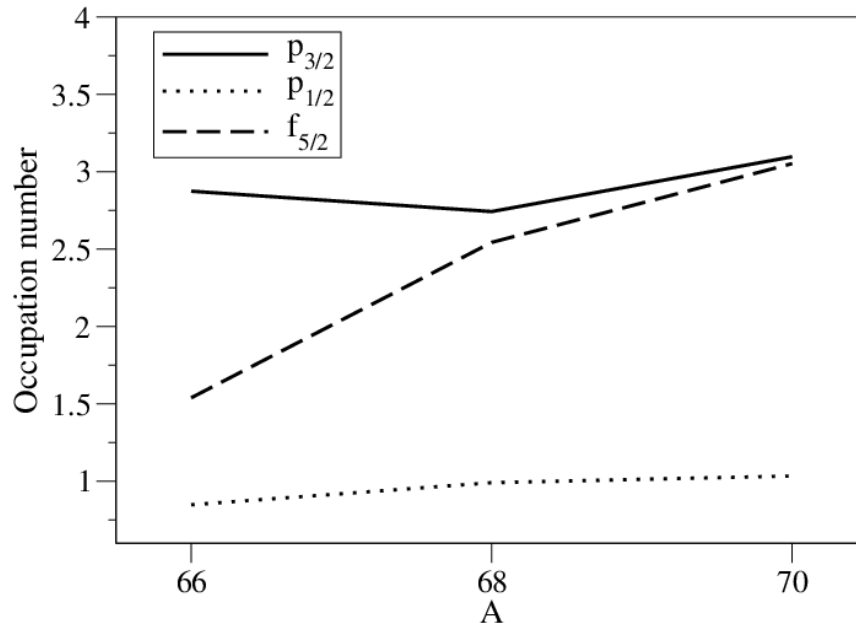


Figure 6.4: Theoretical occupation numbers for $N = Z$, $A \sim 70$ nuclei extracted from shell model work by K. Kaneko [110]. A jump in $f_{5/2}$ orbital occupation (dashed line) is seen at $A = 68$. See text for details.

$f_{5/2}$ orbital results in an increase in the $B(E2)$ value due to the large quadrupole matrix element between the $f_{7/2}$ and the $f_{5/2}$ orbitals. For odd-odd $N = Z$ nuclei, the $B(E2)$ value is expected to be reduced by Pauli blocking effects [110]. The region where staggering is observed may be limited since in the lower-mass region the $\nu f_{5/2}$ and $\nu p_{1/2}$ occupations will be small, whilst in the $A \sim 80$ region the $g_{9/2}$ orbit plays a key role. Further data are clearly required to study this interpretation further.

6.2 Collectivity In $A = 70$ Isobaric Nuclei

A comparison of 2_1^+ state lifetimes in ^{70}Br and ^{70}Se is interesting in view of previous discussions on potential differences in low-spin analogue state shapes in $A \sim 70$ nuclei [14, 16, 17, 31]. The deduced $B(E2; 2_1^+ \rightarrow 0_{gs}^+)$ values in this work would suggest that the two nuclei have similar collectivity for both of these transitions. Recent lifetime measurements [93] coupled with low-energy Coulomb excitation data [112] support an oblate ground state shape for ^{70}Se . Furthermore, since the current work is in agreement with the previously measured lifetime of Ljungvall *et al.* [93], the present work supports the oblate assignment of the ground state of ^{70}Se . The

6.2. COLLECTIVITY IN $A = 70$ ISOBARIC NUCLEI

Table 6.1: $B(E2; 2_1^+ \rightarrow 0_{gs}^+)$ results for ^{70}Br and ^{70}Se compared to various model calculations discussed in the text. All values are in e^2fm^4 .

Nucleus	JUN45	GXPF1A	VAMPIR	From Ref. [11]	β_2	Present
^{70}Br	378	353	541	966		291(43)
^{70}Se	348	365	492	743		332(37)

^{70}Br $B(E2\downarrow)$ result falls close to the equivalent measured value of the analogue state in ^{70}Se . This is consistent with the two nuclei having the same shape in their ground state, as expected for isobaric analogue states. The present work is therefore consistent with an oblate shape for the ground state structure of ^{70}Br .

Several explanations for the negative CED observed between ^{70}Br and ^{70}Se have been put forward. One explanation, now discounted, was that the negative CED is caused by the Thomas-Ehrman shift [13, 113, 114] of the loosely bound proton in ^{70}Br . The extended proton radius in this nucleus would act to lower the overlap between neutron and proton wavefunctions. This interpretation is currently not believed to be correct as it does not explain the observed positive CED in heavier systems (see Fig. 1.3), which have similar binding energy differences to the $A = 70$ system. An explanation for the negative CED based on shape stretching with increasing angular momentum was also put forward [17]. A third possible explanation is that the negative CED is due to the influence of the electromagnetic spin-orbit interaction [22]. The electromagnetic spin-orbit interaction is usually not important when describing nuclear systems as it is two orders of magnitude weaker than the nuclear spin-orbit interaction. However, in $N = Z$ nuclei the influence of the electromagnetic spin-orbit term is believed to become more prominent [22]. Energy shifts due to this interaction increase the gap between the $p_{3/2}f_{5/2}$ and the $g_{7/2}$ orbitals for neutrons, however it decreases the gap for protons. This means that excitations across this gap for the two types of nucleon contribute differing amounts to the CED, which can result in an overall negative CED when comparing the $N = Z$ nucleus to its relatively neutron-rich/proton-deficient isobaric partner. Another explanation for the negative CED, based on shape mixing, suggests that ^{70}Br and ^{70}Se have different shapes in their ground state due to the polarising effect of the Coulomb interaction on the valence nucleons. The theoretical studies that resulted in some of these explanations being put forward are presented and discussed below.

Shell model calculations [21–23] using the GXPF1A interaction in the fp model space give $B(E2; 2_1^+ \rightarrow 0_{gs}^+)$ values for ^{70}Br (^{70}Se) of 353 (365) $e^2\text{fm}^4$. This suggests similar levels of collectivity in the two nuclei, in reasonable agreement with what is experimentally observed - see Table 6.1. The GXPF1A interaction suggests that the $B(E2\downarrow)$ value in ^{70}Se is slightly higher than in ^{70}Br , but this situation is reversed for calculations performed with the JUN45 interaction, which give calculated values of the $B(E2; 2_1^+ \rightarrow 0_{gs}^+)$ for ^{70}Br (^{70}Se) of 378 (348) $e^2\text{fm}^4$. Both shell model interactions reproduce the absolute experimental values quite well. More precise $B(E2)$ values will be required to provide a better test of any differences. Excluding the INC interaction in the shell model calculations with either the GXPF1A or JUN45 interaction was found to have a negligible effect on the calculated $B(E2)$ values.

Excited VAMPIR calculations (see Refs. [31, 32]) result in $B(E2; 2_1^+ \rightarrow 0_{gs}^+)$ values for ^{70}Br (^{70}Se) of 541 (492) $e^2\text{fm}^4$ [115] - see Table 6.1. The Excited VAMPIR approach therefore predicts a stronger difference in the collectivity seen in ^{70}Br and ^{70}Se . This is not supported by the current experimental results. Excited VAMPIR calculations allow the possibility of different prolate and oblate admixtures for isobaric nuclei, and indeed predict this for the $A \sim 70$ pair. In ^{70}Se , a predominantly oblate ground state is predicted, with oblate (prolate) wavefunction components found to be 57% (42%), 59% (41%), 64% (36%) and 39% (61%) for the first 0^+ , 2^+ , 4^+ and 6^+ states, respectively [14]. For ^{70}Br , the calculations predict a predominately prolate ground state with the oblate (prolate) wavefunction components found to be 36% (64%), 41% (59%), 41% (58%) and 20% (80%) for the analogue 0^+ , 2^+ , 4^+ and 6^+ states, respectively [14]. This shape difference is one interpretation of the cause of the negative Coulomb energy differences seen in the $A = 70$ isobar (see Fig. 1.3). This interpretation is not supported by this work. The Excited VAMPIR calculations do not reproduce the absolute collectivity values as successfully as the shell model calculations.

Experimental $B(E2\downarrow)$ values for ^{70}Br and ^{70}Se were compared to values derived by the author from published deformation parameters using the finite-range droplet macroscopic model and the folded Yukawa single-particle microscopic model [11]. Values were derived by the author assuming the rigid rotor approximation. The calculations return $B(E2; 2_1^+ \rightarrow 0_{gs}^+)$ values for ^{70}Br (^{70}Se) of 966 (743) $e^2\text{fm}^4$ - see Table 6.1. This suggests an even greater difference in collectivity between the two isobaric nuclei than the Excited VAMPIR calculations.

Table 6.2: $B(\sigma L\downarrow)$ calculations (courtesy of K. Kaneko [110]) for the $3_1^+ \rightarrow 2_1^+$ and $5_1^+ \rightarrow 3_1^+$ transitions in ^{70}Br compared to experimental results deduced in this work.

	$B(\text{ML}; J_i^\pi \rightarrow J_f^\pi)$	JUN45	GXPf1A	Present	Unit
^{70}Br	$B(\text{E2}; 5_1^+ \rightarrow 3_1^+)$	195	460	450(110)	e^2fm^4
^{70}Br	$B(\text{M1}; 3_1^+ \rightarrow 2_1^+)$	0.132	0.012	0.027(13)	μ_N^2

6.3 Further ^{70}Br Discussion

6.3.1 B(M1) Measurement: The Quasideuteron Picture

The small B(M1) value deduced for the $3_1^+ \rightarrow 2_1^+$ decay in ^{70}Br is interesting. B(M1) values resulting from $\Delta\mathbf{T} = 1$ transitions in odd-odd $N = Z$ nuclei have been discussed in terms of the quasideuteron picture of valence nucleons (see Ref. [48] and Section 2.5). Large B(M1) values have been observed between $\mathbf{T} = 0$ and $\mathbf{T} = 1$ states in a range of odd-odd nuclei in the region, such as ^{46}V [116, 117], ^{50}Mn [118] and ^{54}Co [48]. These enhanced values are converse to the inhibited nature of isoscalar M1 transitions [119]. The enhancement seen in $\Delta\mathbf{T} = 1$ M1 transition strengths is expected to disappear in the fp shell and re-emerge around ^{74}Rb , when the $g_{\frac{3}{2}}$ orbital becomes important [48]. The B(M1) strength is therefore expected to be hindered in ^{70}Br .

The small B(M1) value deduced in this work for the ^{70}Br $3_1^+ \rightarrow 2_1^+$ decay is indicative of the non-quasideuteron scenario, suggesting that the main component of the 3_1^+ wavefunction should involve the odd proton and neutron primarily occupying $f_{\frac{5}{2}}$ or $p_{\frac{1}{2}}$ orbitals (i.e., $j = \ell - \frac{1}{2}$ coupling).

The hindered nature of the B(M1) is consistent with shell model calculations using the GXPf1A interaction in the fp model space [21–23], which predict a small B(M1) value for the $3_1^+ \rightarrow 2_1^+$ transition in ^{70}Br (see Table 6.2). On a separate note, Table 6.2 shows that the GXPf1A calculations also reliably replicate the experimental $B(\text{E2}; 5_1^+ \rightarrow 3_1^+)$ transition strength measured in ^{70}Br .

A potential way of extracting information on single-particle orbital occupations is by measuring the momentum distribution of the recoil nuclei that have undergone

nucleon knockout. The parallel momentum distribution (that is, the momentum of recoil nuclei parallel to the direction of beam propagation) is intrinsically related to the orbital angular momentum ℓ of the knocked-out nucleon. Classically, for example, if the nucleon was orbiting the nucleus with its angular momentum vector pointing along the beam direction, it would be orbiting in a plane perpendicular to the beam direction and thus would have a very small parallel momentum component in the recoil rest frame. If, however, it was orbiting with its angular momentum vector pointing perpendicular to the beam direction, it could potentially have a large parallel momentum in the recoil rest frame when knocked out. Quantum mechanically, higher- ℓ nucleon single-particle orbitals have a larger number of possible projections. The width of the recoil parallel momentum distribution, therefore, gives information on the orbital angular momentum ℓ of the knocked-out nucleon. More information can be found in Ref. [120].

Fig. 6.5 shows the experimental momentum distribution of the ^{70}Br recoils after gating on the $3_1^+ \rightarrow 2_1^+$ transition with a background subtraction, compared to various calculated momentum distributions based on the eikonal reaction theory [43], performed by E. C. Simpson. Background contributions were removed by subtracting a momentum distribution gated on a γ background close in energy to the $3_1^+ \rightarrow 2_1^+$ transition peak and with an identical width (in bins) to the gate for the 403 keV γ ray. The solid, dot-dashed and dotted theoretical distributions correspond to calculations assuming the knocked-out neutron in ^{71}Br resides in the $p_{\frac{3}{2}}$, $f_{\frac{5}{2}}$ and $g_{\frac{9}{2}}$ orbital, respectively. The experimental distribution, which includes feeding to the 3_1^+ state as well as direct population, appears most consistent with the removal of an $l = 3$ ($f_{\frac{5}{2}}$) orbit nucleon. This interpretation is consistent with the information deduced from the B(M1) value for the $3_1^+ \rightarrow 2_1^+$ transition.

It is important to note that the momentum distribution comparison made in this section does not conclusively prove that the 3_1^+ state is primarily made up of $f_{\frac{5}{2}}$ configurations, as the experimental momentum distribution includes contributions from the 5_1^+ state and any other potential feeding states that were not populated with significant enough intensity to be observed in this work. If the 3_1^+ state had a significant $p_{\frac{1}{2}}$ component, with the higher-lying feeding states having $f_{\frac{5}{2}}$ configurations, then the momentum distribution width would still be characteristic of $f_{\frac{5}{2}}$ configurations. A significant $p_{\frac{1}{2}}$ component would still result in a hindered B(M1) value as it is also a $j = \ell - \frac{1}{2}$ orbital.

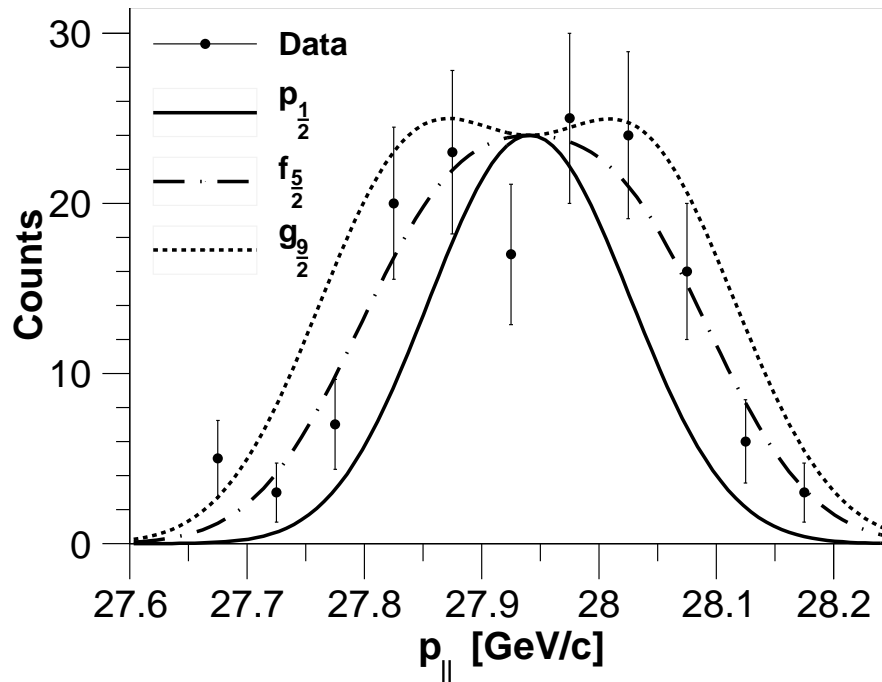


Figure 6.5: Experimental momentum distribution of ^{70}Br recoils gated on the $3_1^+ \rightarrow 2_1^+$ transition with background subtraction (black points). The solid, dot-dashed and dotted lines show calculated recoil momentum distributions assuming the knocked-out neutron in ^{71}Br resides in the $p_{3/2}$, $f_{5/2}$ and $g_{9/2}$ single particle orbital, respectively [43]. The calculations have been adjusted to account for target-broadening effects.

6.3.2 Theoretical Spectroscopic Factors For ^{70}Br

The neutron most likely to be knocked out of ^{71}Br is the unpaired, valence neutron, whose spin-parity dictates the ^{71}Br ground state. Shell model calculations (courtesy of E. C. Simpson) were used to predict proton and neutron occupancies for the ^{71}Br ground state in order to ascertain what spin-parity is predicted. The results are shown in Table 6.3 and predict a $\frac{5}{2}^-$ ground state for ^{71}Br . This supports the tentative assignment of a $\frac{5}{2}^-$ ground state for ^{71}Br in the literature [121]. The calculations predict that the $\frac{5}{2}^-$ state is very complicated with many states near the Fermi surface being involved, therefore one cannot say too much about the orbitals from which the knocked-out neutron in ^{71}Br was removed.

Shell model calculations in a truncated fp model space using the GXPF1A interaction were performed in order to extract the spectroscopic factors of neutron knockout from ^{71}Br to excited states in ^{70}Br (see Table 6.4). The shell model calculations were

6.3. FURTHER ^{70}Br DISCUSSION

Table 6.3: Shell model calculations by E. C. Simpson of ground state orbital occupancies in ^{71}Br . See text for details.

	Proton	Neutron
$f_{\frac{7}{2}}$	7.812	7.846
$p_{\frac{3}{2}}$	3.069	3.111
$f_{\frac{5}{2}}$	3.182	3.895
$p_{\frac{1}{2}}$	0.938	1.148

performed by E. C. Simpson [122] using the shell model code *Antoine* [123]. In the lowest configuration of ^{70}Br it was assumed that 16 nucleons occupied the $f_{\frac{7}{2}}$ orbital, with the remaining 14 nucleons distributed over the rest of the fp shell. The truncation was to $t = 5$, i.e., all configurations with up to five holes in the $f_{\frac{7}{2}}$ shell were considered (for either species of nucleon). The ‘missing’ values in the table are due to angular momentum coupling restrictions.

The calculations in Table 6.4 predict a more compressed level scheme compared to reality, with the first excited 2^+ state (934 keV) predicted to lie at 432 keV. The calculations also predict two 1^+ states below the first 2^+ state, which are not experimentally observed. The shell model calculations predict a very small population of the yrast 1^+ state, which is consistent with the lack of evidence for the $1_1^+ \rightarrow 0_{gs}^+$ transition in the experimental spectra. The calculations in Table 6.4 imply a significant direct population of the 5_1^+ state, which is predicted to predominately involve the $f_{\frac{5}{2}}$ orbital. The calculations also predict a non-negligible occupation of the known 5_2^+ state (also $f_{\frac{5}{2}}$ dominant), but the known decays from this state [12] are not observed in this work. Significant population of the 3_1^+ state is seen, which is predicted to primarily involve the $p_{\frac{1}{2}}$ orbital. If it is assumed that this state corresponds to the experimentally observed 3_1^+ state at an excitation energy of 1336 keV (despite the calculations predicting it to lie below the 2_1^+ state), this is consistent with the hindered $B(M1; 3_1^+ \rightarrow 2_1^+)$ strength deduced in this work as the $p_{\frac{1}{2}}$ state is a $j = \ell - \frac{1}{2}$ orbital. The shell model calculations predict a strong direct population of two non-yrast 3^+ states, both of which have strong $f_{\frac{5}{2}}$ components, which is also a $j = \ell - \frac{1}{2}$ orbital. Assuming one of these two states is not the experimentally observed 3_1^+ state at 1336 keV, decays from these states are not observed experimentally. The shell model calculations predict very small spectroscopic factors for direct population to the yrast 4^+ state, consistent with it not being observed experimentally. The shell

6.3. FURTHER ^{70}Br DISCUSSION

Table 6.4: Theoretical spectroscopic factors for one-neutron knockout to excited states in ^{70}Br from shell model calculations using the GXPF1A interaction in a truncated fp model space. The largest spectroscopic values are shown in bold. Theoretical excitation energies are also included (E_{theo}). Courtesy of E. C. Simpson.

State	E_{theo} [keV]	Spectroscopic Factor			
		$f_{\frac{7}{2}}$	$p_{\frac{3}{2}}$	$f_{\frac{5}{2}}$	$p_{\frac{1}{2}}$
0_{gs}^+	0.0	-	-	0.004849	-
1_1^+	68	0.001498	0.061226	0.038027	-
3_1^+	99	0.000052	0.003526	0.014139	0.107380
1_2^+	333	0.001252	0.021709	0.009634	-
2_1^+	432	0.001345	0.014134	0.003998	0.030831
3_2^+	517	0.007492	0.013410	0.302488	0.042899
5_1^+	522	0.006400	-	0.774740	-
1_3^+	535	0.005801	0.015012	0.023667	-
2_2^+	642	0.005585	0.075044	0.003006	0.050054
4_1^+	665	0.002906	0.009751	0.023490	-
2_3^+	764	0.004944	0.007956	0.073259	0.005043
3_3^+	893	0.000620	0.008669	0.177451	0.007276
5_2^+	1108	0.000006	-	0.100538	-
4_2^+	1386	0.007578	0.040077	0.003861	-
4_3^+	1486	0.001330	0.040825	0.019060	-
6_1^+	1721	0.003113	-	-	-
6_2^+	1828	0.002937	-	-	-
6_3^+	2491	0.010183	-	-	-

model calculations predict a very small direct population of the 2_1^+ state, whereas in this work it was assumed that 76.4% direct population of the state occurred. It is possible that other states are decaying through the 2_1^+ state that were too low in intensity to be identified, however only the known 4_1^+ and 3_1^+ states have been observed to decay to the 2_1^+ state in the literature [12]. Population of other states is predicted by these calculations, however this population is predicted to be weak. This is consistent with the lack of evidence for transitions from these states in the experimental spectra.

6.4 ⁶⁹Se: Comparison To Shell Model Calculations

Antoine shell model calculations were performed by the author for one-neutron knockout to ⁶⁹Se in order to understand the excited states populated in this work. The results of these calculations are summarised in Table 6.5. Calculations were performed using the GXPF1A interaction in the *fp* model space, truncated to $t = 5$ (i.e., allowing up to five particle-hole excitations from the $f_{7/2}$ orbital). Table 6.5 contains predicted spectroscopic factors (S.F.) and excitation energies E_{theo} . Based on the predicted energies and spectroscopic factors, certain states have been attributed to the states experimentally observed (results in the E_{exp} column). Since the shell model calculations are for single-nucleon knockout from the 0^+ ground state in ⁷⁰Se, population of excited states in ⁶⁹Se is very pure, e.g., 7_2^- states can only be populated via knockout of a neutron from the $f_{7/2}$ orbital, and so on.

The shell model calculations correctly predict the observed $1/2^-$ ground state in ⁶⁹Se (see Table 6.5). The calculations also correctly predict two low-lying $3/2^-$ states and predict that direct population to the $3/2_2^-$ state is strong, with only a weak direct population of the yrast $3/2^-$ state. The calculations predict a significant population of the $5/2_1^-$ state in ⁶⁹Se, however the decay from this state is not seen experimentally so this cannot be verified. The calculations correctly predict that the $3/2_1^-$ and $5/2_1^-$ states lie close to each other in energy, however the calculations place the $5/2_1^-$ state above the $3/2_1^-$ state in energy, contrary to what is experimentally observed. The calculations predict a vanishingly small population of the yrast $7/2^-$ state (see Table 6.5), with larger populations of the $7/2_2^-$ and $7/2_3^-$ states. It has been assumed, therefore, that the

Table 6.5: *Antoine* shell model calculations performed by the author for one-neutron knockout to excited states in ⁶⁹Se using the GXPF1A interaction in a truncated *fp* model space. Quoted are predicted spectroscopic factors (S.F.) and excitation energies (E_{theo}). Experimentally observed excited states have been assigned in the E_{exp} column. See text for details.

J^π	N	S.F.	E_{theo} [keV]	E_{exp} [keV]
$\frac{1}{2}$	1	0.306698	0.0	0.0
$\frac{3}{2}$	1	0.059930	110	129
$\frac{5}{2}$	1	2.102255	133	39
$\frac{3}{2}$	2	0.955750	534	290
$\frac{3}{2}$	3	0.004850	692	(790?)
$\frac{5}{2}$	2	0.185608	753	713
$\frac{7}{2}$	1	0.000027	885	-
$\frac{1}{2}$	2	0.340468	978	(790?)
$\frac{5}{2}$	3	0.004949	1109	(790?)
$\frac{7}{2}$	2	0.094992	1163	915
$\frac{5}{2}$	4	0.025454	1322	-
$\frac{7}{2}$	3	0.266637	1391	1123
$\frac{3}{2}$	4	0.015506	1548	-
$\frac{3}{2}$	5	0.050388	1818	-
$\frac{5}{2}$	5	0.062983	1825	-
$\frac{7}{2}$	4	0.011035	1842	-
$\frac{1}{2}$	3	0.015767	2006	-
$\frac{7}{2}$	5	0.087977	2499	-
$\frac{1}{2}$	4	0.007993	2576	-
$\frac{1}{2}$	5	0.071708	2815	-

spectroscopic factors to the $\frac{7}{2}_2^-$ and $\frac{7}{2}_3^-$ states in the calculations correspond to the experimentally observed $\frac{7}{2}_1^-$ and $\frac{7}{2}_2^-$ states, respectively.

As indicated in Table 6.5, three candidate states (with spin-parities of $\frac{1}{2}^-$, $\frac{3}{2}^-$ and $\frac{5}{2}^-$) have been selected as potentially giving rise to the previously unobserved 500 keV γ transition in ^{69}Se (see Table. 5.7). Of these, it is believed that the most likely candidate for this new state is an excited $\frac{1}{2}^-$ state. No excited $\frac{1}{2}^-$ states have been observed experimentally in ^{69}Se [100,101]. The $\frac{1}{2}_2^-$ state predicted in the shell model calculations has a much larger associated spectroscopic factor than the other two candidate states (see Table 6.5). If the $\frac{1}{2}^-$ spin-parity assignment is correct, this would help to explain why it has not been observed previously, as previous studies have employed fusion-evaporation reactions (e.g., [100,101]) whereas this work uses single-neutron knockout for the first time. This however does not rule out the state being the previously unobserved $\frac{3}{2}_3^-$ or $\frac{5}{2}_3^-$ states, as these are both non-yrast and are also unlikely to be strongly populated in fusion-evaporation reactions. A $\frac{1}{2}^-$ assignment for this state supports a lack of conclusive evidence for the 125 keV transition from the $\frac{7}{2}_1^-$ state, as this would require at least an M3 transition.

Theoretical spectroscopic factors have been combined with branching ratio data [100,101] to give the theoretical ^{69}Se partial level scheme in Fig. 6.6. Note that the branching ratio from the $\frac{7}{2}_1^-$ state was taken from Ref. [100], which was in agreement with the branching ratio measured in this work. The experimental level scheme is also reprinted in the figure for comparison. The $\frac{1}{2}_2^-$ state has been assigned to the new state, however the other two candidates are also included on the figure as dashed levels.

6.5 Evidence Of Radiative Electron Capture

Electron capture is the process whereby an incoming heavy-ion projectile nucleus captures an electron from a light target nucleus [124]. Radiative electron capture (REC) involves the transfer of an electron to a shell of the projectile atom. In the REC process the electron loses energy, which is converted to electromagnetic energy in the form of an X ray. The energy of the X ray is dependent on the nature of the projectile nucleus. The K-shell REC peak energy in the projectile rest frame, E_{peak} ,

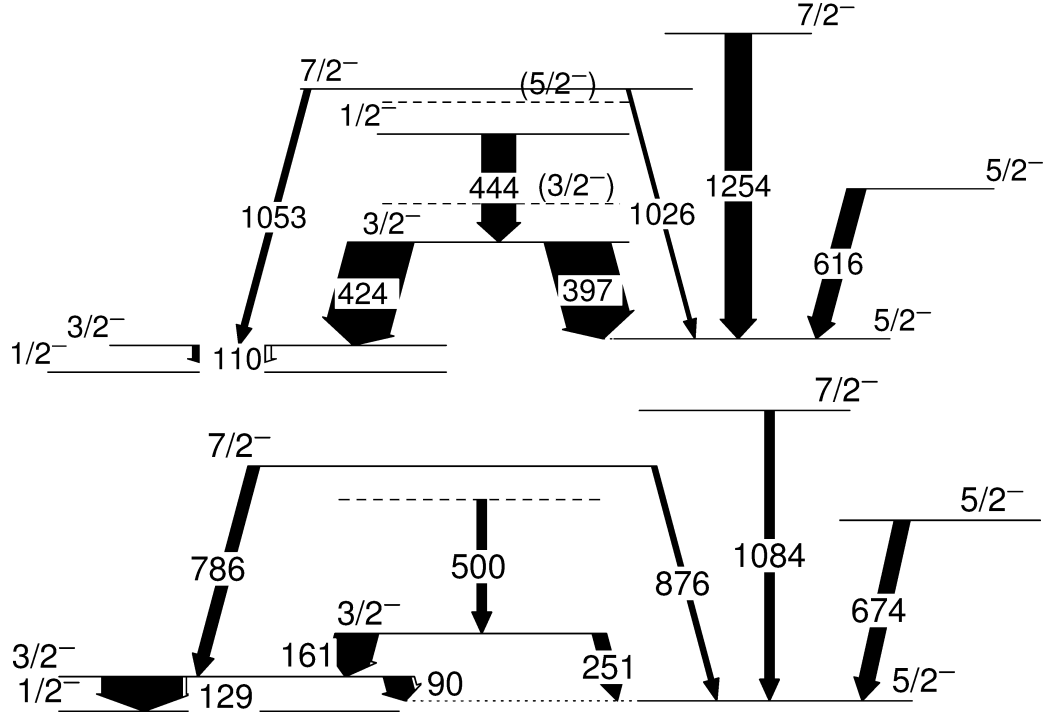


Figure 6.6: Theoretical level scheme of ^{69}Se (top) based on shell model calculations. Arrow width corresponds to transition intensity relative to the 129 keV $\frac{3}{2}^- \rightarrow \frac{1}{2}^-_{gs}$ transition, extracted using theoretical spectroscopic factors from Table 6.5 and known branching ratios from the literature [100, 101]. The new state (see Fig. 5.14) has been assigned as a $\frac{1}{2}^-$ state, however the two other candidate states are also shown as dashed levels. Also reprinted in this figure for convenience is the experimental partial level scheme for ^{69}Se deduced from this work (bottom).

is given by the sum of the electron relativistic kinetic energy $E_{kin} = (\gamma - 1)mc^2$ and the K-electron binding energy E_K [124]. Radiative electron capture to the L or M shells in the projectile nucleus is also possible.

Considering a secondary beam nucleus in this work undergoing REC, the kinetic energy of an electron in the projectile rest frame is approximately 49 keV. The velocity of the projectile assumed in this calculation is $0.4c$, which was the centroid of the measured β distribution of the incoming particles as recorded during an experimental run with no secondary target foil in place. The electron binding energies in this work were taken from Ref. [125]; these binding energies, assuming an incoming ^{70}Se projectile, were 13 keV (K shell), 2 keV (L shell) and ≤ 1 keV (other shells). Therefore, it was expected in this work to observe a K-shell REC peak in the projectile rest frame at an energy of $49 + 13 = 62$ keV, with a possible satellite peak from L-shell capture at $49 + 2 = 51$ keV. It would not be possible to differentiate

higher-shell REC peaks from each other as the electron binding energy becomes negligible relative to the electron kinetic energy.

The REC phenomenon was studied in this work as part of the target-only runs by deliberately turning down the low-energy thresholds on the SeGA detectors to around 20 keV. Fig. 6.7 shows the secondary beam identification plot for target-only recoils. Indicated on the plot are the distributions corresponding to recoils created from the four major secondary beams (^{71}Br , ^{70}Se , ^{69}As and ^{68}Ge). These ‘banana’ distributions contain all recoils generated from the individual secondary beams after detection in the S800 focal plane. Gating on individual secondary beam distributions and plotting OBJ scintillator time vs. ion chamber energy (see Fig. 6.8) allows one to isolate individual recoils (see Section 4.3 for more details). In Fig. 6.7 one can see narrow distributions that partially overlap with the long secondary beam distributions (labelled $^{71}\text{Br}^*$, $^{70}\text{Se}^*$, $^{69}\text{As}^*$ and $^{68}\text{Ge}^*$ in Fig. 6.7). These distributions are absent from the secondary beam identification plots using distance data (see Fig 4.7), suggesting γ -rays decaying from these particular recoils are below the SeGA threshold in the distance runs but not the target-only runs (i.e., the γ -rays fall in the 20-100 keV range). As will be demonstrated and discussed below, these small distributions contain the REC X-ray components. The small REC distributions in Fig. 6.7 contrast with the long ‘banana’ structures of the secondary beam components. The reason for their localisation in scintillator time is because REC only occurs onto the secondary beam nuclei that remain intact after passing through the target, and so the narrow distributions correspond to only one ‘blob’ on the recoil PID (e.g., Fig. 6.8).

Placing software gates on the secondary beam plot produces the recoil PID plots shown in Fig. 6.8. The left-hand plot shows the resulting PID after gating on both the ^{70}Se and $^{70}\text{Se}^*$ secondary beam distributions. The ^{70}Se recoil distribution is labelled. The right-hand plot in Fig. 6.8 shows the recoil PID after gating on *just* the $^{70}\text{Se}^*$ secondary beam distribution. Here one can see that only one major recoil distribution appears. Gating on the recoil distribution seen in the right-hand plot of Fig. 6.8 gives the γ -ray spectrum shown in Fig. 6.9. The REC X ray corresponding to K-shell electron capture is clearly seen at an energy of 62.3(2) keV, in line with expectation (62 keV). The K-shell REC peak appears to have a low-energy tail that contains a small peak at 50.0(5) keV. This corresponds very closely to the expected location of the L-shell REC peak (51 keV). The low-energy tail of the K-shell REC

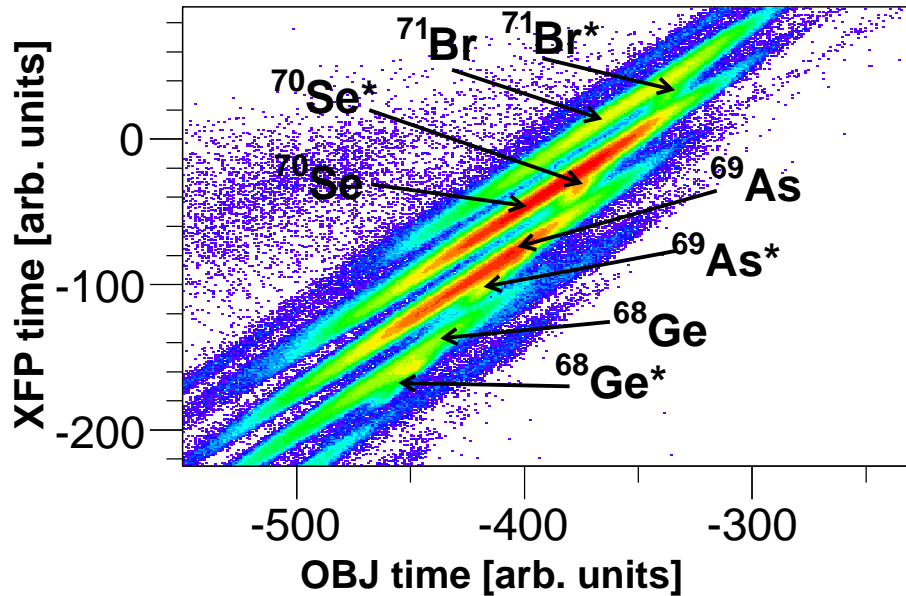


Figure 6.7: Secondary beam identification plot for target-only data. The main secondary beam distributions are labelled (^{71}Br , ^{70}Se , ^{69}As and ^{68}Ge). Also labelled are the distributions corresponding to radiative electron capture of the secondary beam projectiles ($^{71}\text{Br}^*$, $^{70}\text{Se}^*$, $^{69}\text{As}^*$ and $^{68}\text{Ge}^*$).

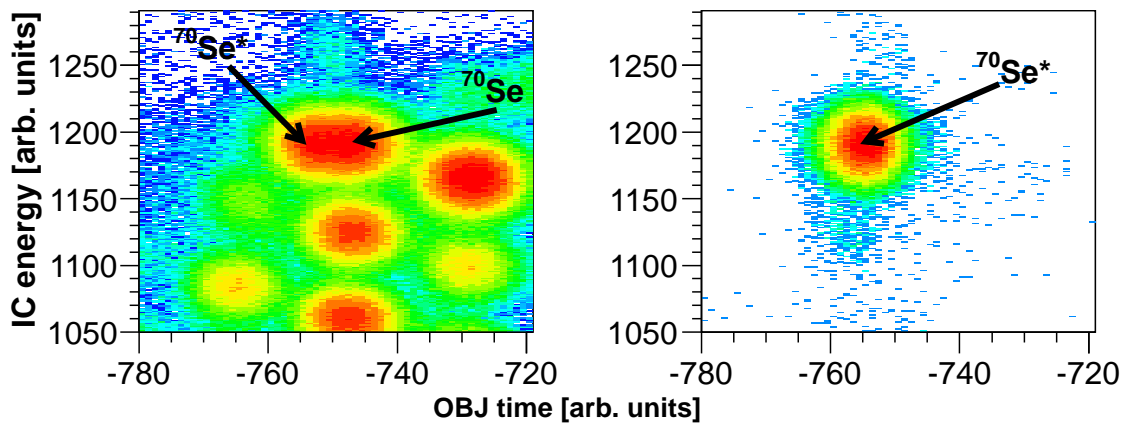


Figure 6.8: Recoil particle identification plots after gating target-only data on all ^{70}Se secondary beam events (left) and after gating on just the REC secondary beam component $^{70}\text{Se}^*$ (right) (see Fig. 6.7). It is clear that the small $^{70}\text{Se}^*$ distribution seen in Fig. 6.7 corresponds to just one distribution on the recoil PID.

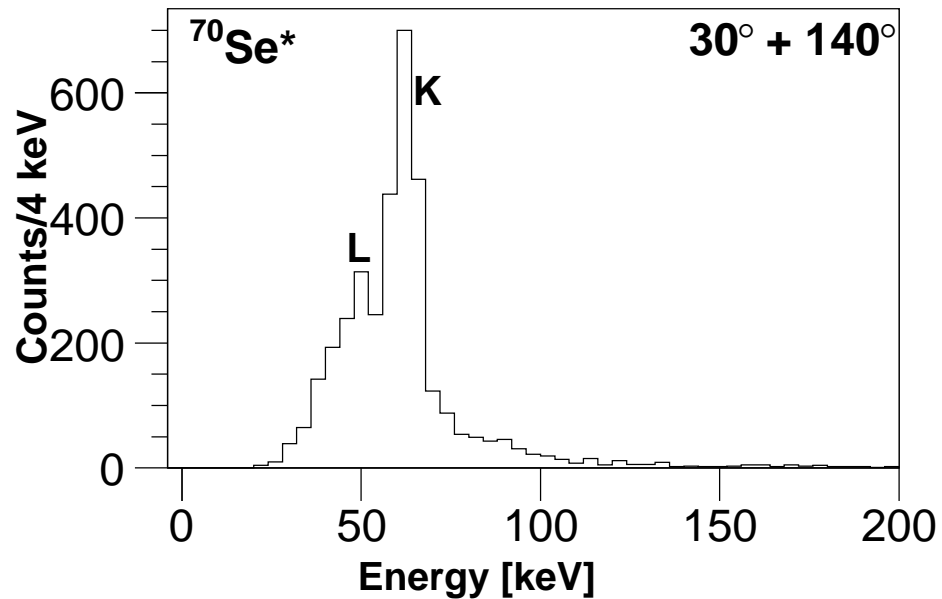


Figure 6.9: γ spectrum after gating on the $^{70}\text{Se}^*$ secondary beam distribution in Fig. 6.7 and the resulting recoil distribution seen on the right-hand plot in Fig. 6.8. The X rays corresponding to radiative electron capture to the projectile K and L shells are labelled.

peak most likely contains contributions from M- or N-shell REC, however it is not possible to separate these and higher-shell contributions.

It is worth noting that the REC peaks are from electron capture onto the secondary beam nuclei only. However, the REC distributions are quite wide on the recoil ID plots and can therefore ‘spill over’ into recoil software cuts made on surrounding nuclei. This is the reason for the small REC peak in the target-only ^{69}Se spectrum (see Fig. 5.13)

Chapter 7

Summary And Future Work

7.1 Summary

To summarise, an experiment was performed at the National Superconducting Cyclotron Laboratory (NSCL) in November/December 2011 using the SeGA germanium array and the S800 spectrograph. Secondary beams of ^{71}Br , ^{70}Se and ^{69}As were created via projectile fragmentation of a ^{78}Kr primary beam at 150 MeV/u. These secondary beams were subsequently used to populate excited states in recoils using a variety of direct reactions and inelastic scattering. The primary focus of the experiment was to measure the lifetimes of low-lying excited states in the odd-odd $N = Z$ nucleus ^{70}Br and a number of other recoils by employing the recoil distance Doppler shift (RDDS) and γ -ray lineshape techniques. The experiment was the commissioning run of a new plunger device, TRIPLEX, designed at NSCL for RDDS measurements.

Excited states in ^{70}Br were populated via single-neutron knockout from the ^{71}Br secondary beam on the ^9Be target. The lifetimes of the $\mathbf{T} = 1$ 2_1^+ , $\mathbf{T} = 0$ 3_1^+ and $\mathbf{T} = 0$ 5_1^+ states were measured. The level of collectivity deduced from the measured lifetimes, together with shell model calculations utilising the fp model space, suggest that the deformation-driving $g_{\frac{9}{2}}$ orbital plays no significant role in the low-lying excited state structure of ^{70}Br . The $B(E2; 2_1^+ \rightarrow 0_{gs}^+)$ strength deduced in this work for ^{70}Br suggests a reduced collectivity relative to the lower neighbouring $N = Z$ nucleus,

^{68}Se . This result, when combined with shell model calculations for $N = Z$ nuclei in the $A = 64\text{--}72$ region, tentatively suggests the presence of a staggering in the $B(E2)$ values between even-even and odd-odd nuclei. The results for ^{70}Br are reproduced by shell model calculations using the GXPF1A interaction in the fp model space including the Coulomb, spin-orbit and isospin non-conserving interactions. The $3_1^+ \rightarrow 2_1^+$ decay in ^{70}Br is found to have a very small $B(M1)$ value, which is consistent with the configuration of the state being dominated by the coupling of $j = l - \frac{1}{2}$ ($f_{\frac{5}{2}}$ and $p_{\frac{1}{2}}$) orbital nucleons.

States in ^{68}Se were populated via two-neutron knockout from the ^{70}Se secondary beam. The measured lifetime yields a $B(E2\downarrow)$ value that is consistent with the $B(E2\uparrow)$ obtained from relativistic Coulomb excitation measurements [7]. The results are well produced by shell model calculations using both the GXPF1A interaction (fp model space) and the JUN45 interaction ($f_{\frac{5}{2}}pg_{\frac{9}{2}}$ model space). Previously unknown γ rays are reported in this work for ^{68}Se , but coincidence measurements were not possible due to low statistics and so these new γ rays could not be placed in the known level scheme.

^{72}Kr excited states were populated via the one-proton pickup reaction on the ^{71}Br secondary beam. The measured lifetime of the 2_1^+ state in this work has a very large error, however it supports the lifetime measured in the literature [8, 9]. The 2_1^+ lifetime result suggests an increased collectivity relative to ^{70}Br and supports the presence of $g_{\frac{9}{2}}$ orbital configurations in ^{72}Kr . This is reflected by the inability of shell model calculations to replicate the experimental collectivity in ^{72}Kr when the $g_{\frac{9}{2}}$ orbital is not included.

Excited states in ^{70}Se were populated via inelastic scattering of the ^{70}Se secondary beam on the target. The 2_1^+ lifetime result is in agreement with a previous lifetime result [93] and acts to support the previously assigned oblate shape to low-lying states in this nucleus. The $B(E2)$ values for the decays of the ($\mathbf{T} = 1$) 2_1^+ states in ^{70}Br and ^{70}Se deduced in this work are almost identical, suggesting there is no major shape change between the two nuclei at low spin.

Excited states in ^{66}Ge were populated via $2p2n$ knockout from the ^{70}Se secondary beam. Lifetimes were extracted for the 7_1^- and 2_1^+ states. Both results were found to be in good agreement with the previously published values [95–97].

^{69}Se low-lying excited states were populated via one-neutron knockout from the ^{70}Se secondary beam. Lifetimes of the $\frac{3}{2}_1^-$ and $\frac{3}{2}_2^-$ states were measured for the first time in this work. Two previously unobserved γ rays were seen in ^{69}Se . The new 500 keV transition was observed to come in coincidence with decays from the yrast and non-yrast $\frac{3}{2}^-$ states and is believed to result from the decay of a new level at 790 keV excitation energy. Shell model calculations were used to tentatively assign a $\frac{1}{2}^-$ spin-parity to this previously unobserved state. The new 524 keV transition in ^{69}Se was too weak for coincidence measurements and hence it was not possible to assign it a position in the level scheme.

Excited states in ^{65}Ga were populated via multiple-nucleon knockout from both the ^{70}Se and the ^{69}As secondary beams. Excited state populations were found to be virtually identical for both reactions. The lifetime of the $\frac{5}{2}_1^-$ state was measured in this work and found to be consistent with the upper limit quoted in the literature [105].

7.2 Future Work

The tentative staggering of $B(E2; 2_1^+ \rightarrow 0_{gs}^+)$ values seen between odd-odd and even-even $N = Z$ nuclei in this work is interesting and calls for further studies to extract excited state lifetimes in other odd-odd self-conjugate nuclei in the region, such as ^{66}As and ^{74}Rb . These lifetime measurements would help to complete the mapping of mid-shell collectivity changes. This forms part of a greater undertaking, which would be to fully map the collectivity in the *fp*g shell from $A = 56$ to $A = 100$. Comparison of absolute $B(E2)$ values for ^{68}Se and ^{70}Br to shell model calculations would benefit from repeat lifetime measurements to increase the precision of the results. A more precise $B(E2; 2_1^+ \rightarrow 0_{gs}^+)$ result for ^{70}Br would also be helpful for comparisons to the analogue $B(E2\downarrow)$ in ^{70}Se to understand any potential collectivity differences in the two isobaric nuclei.

It will be important in future to perform multi-step Coulex studies of ^{70}Br to confirm the oblate shape at low spin. Further to these experiments, γ spectroscopy studies of ^{70}Kr to identify the low-lying excited states would allow for a fuller analysis of potential isospin-breaking effects in the $A = 70$ isobar.

7.2. FUTURE WORK

If a single-neutron knockout experiment of ^{70}Br were to be repeated it would be useful to assign sufficient time to study excited states in ^{70}Se via one-proton knockout, which was the original intention of the experiment analysed in this work. ^{70}Br and ^{70}Se excited states generated via mirrored reaction mechanisms in the same experimental set-up would allow for a thorough study of potential structural differences between the two nuclei.

It would be beneficial to perform a direct lifetime measurement of ^{68}Se excited states as part of a dedicated experiment in order to achieve clean enough statistics to measure a lifetime for the 4_1^+ state and identify the origins of the previously unobserved γ rays seen in this work.

In conclusion, the experiment performed at NSCL on nuclei in the $A \sim 70$, $N = Z$ region was highly successful and revealed new physics which is directly useful for the understanding of these exotic nuclei. Of particular importance is the measurement of the 2_1^+ state lifetime in ^{70}Br , which helps to identify the location of the low-spin collectivity jump in the mid- fp shell. The ^{70}Br 2_1^+ lifetime measurement is consistent with a lack of any significant $g_{\frac{9}{2}}$ orbital occupation in the low-lying excited states of $A \sim 70$, $N = Z$ nuclei up to and including ^{70}Br .

Appendix A

The Lifetime Suite: An Example Code

This appendix shows an example code from the *Lifetime Suite* of programs that was written by the author to analyse various aspects of the data such as excited state lifetimes, target/degrader ratios and feeding intensities. This particular code extracts the lifetime of the first excited 2^+ state in ^{70}Br using simulated fits to $275\ \mu\text{m}$ distance data.

```
//calculates lifetime of excited 2+ state in 70Br
//touching distance data

#include <string.h>
#include "TChain.h"
#include "TFile.h"
#include "TH1.h"
#include "TF1.h"
#include "TTree.h"
#include "TKey.h"
#include "Riostream.h"
#include "TMath.h"
#include "TString.h"

void lifetime_calculator_br70_2_0um(){

    //used to scale the simulated spectra to the experimental spectra
    double scale30 = 0.108;
    double scale140 = 0.077;

    Int_t maxsimfiles =16; //defines the number of simulation files made
```

```

int ring = 3; //front ring =1, back = 2, both = 3

//define bin limits of 'region of lifetime sensitivity'
Int_t minbin30 = 230;
Int_t maxbin30 = 259;
Int_t minbin140 = 209;
Int_t maxbin140 = 237;

double start = 1.5; //lifetime of the first datapoint (in ps)

//variable declarations
double realbinvalue30[500];
double realspecerror30[500];
double simbinvalue30[500][500];
double sum30[500][500];
double total30[500];
double p30;
double a30[500][500];
double a30_error[500][500];
double b30[500][500];

double realbinvalue140[500];
double realspecerror140[500];
double simbinvalue140[500][500];
double sum140[500][500];
double total140[500];
double p140;
double a140[500][500];
double a140_error[500][500];
double b140[500][500];

double p;
double total[500];

//histogram declarations
TH1D *sim30[500];
TH1D *sim140[500];

TKey *keysim30[500];
TKey *keysim140[500];

TFile *realfile30 = new TFile("./histograms/br_70/runs-at-0um-hist.root");
TFile *realfile140 = new TFile("./histograms/br_70/runs-at-0um-hist.root");
TFile *simfile[16];

simfile[0] = new TFile("./g4work/70Br/Output/2/0um/br_lifetime2_0um_1.5.root");
simfile[1] = new TFile("./g4work/70Br/Output/2/0um/br_lifetime2_0um_2.0.root");
simfile[2] = new TFile("./g4work/70Br/Output/2/0um/br_lifetime2_0um_2.5.root");
simfile[3] = new TFile("./g4work/70Br/Output/2/0um/br_lifetime2_0um_3.0.root");
simfile[4] = new TFile("./g4work/70Br/Output/2/0um/br_lifetime2_0um_3.5.root");
simfile[5] = new TFile("./g4work/70Br/Output/2/0um/br_lifetime2_0um_4.0.root");

```

```

simfile [6] = new TFile("./g4work/70Br/Output/2/0um/br_lifetime2_0um_4.5.root");
simfile [7] = new TFile("./g4work/70Br/Output/2/0um/br_lifetime2_0um_5.0.root");
simfile [8] = new TFile("./g4work/70Br/Output/2/0um/br_lifetime2_0um_5.5.root");
simfile [9] = new TFile("./g4work/70Br/Output/2/0um/br_lifetime2_0um_6.0.root");
simfile [10] = new TFile("./g4work/70Br/Output/2/0um/br_lifetime2_0um_6.5.root");
simfile [11] = new TFile("./g4work/70Br/Output/2/0um/br_lifetime2_0um_7.0.root");
simfile [12] = new TFile("./g4work/70Br/Output/2/0um/br_lifetime2_0um_7.5.root");
simfile [13] = new TFile("./g4work/70Br/Output/2/0um/br_lifetime2_0um_8.0.root");
simfile [14] = new TFile("./g4work/70Br/Output/2/0um/br_lifetime2_0um_8.5.root");
simfile [15] = new TFile("./g4work/70Br/Output/2/0um/br_lifetime2_0um_9.0.root");

```

```

//check to establish whether histogram is present in file
TKey *keyreal30 = realfile30 ->FindKey("egamdc30_in71Brout70Br");
if (keyreal30 == 0){
    cout << "!!Histogram in realfile does not exist!!" <<endl;
    throw 1;
}

```

```

TKey *keyreal140 = realfile140 ->FindKey("egamdc140_in71Brout70Br");
if (keyreal140 == 0){
    cout << "!!Histogram in realfile does not exist!!" <<endl;
    throw 1;
}

```

```

for (Int_t k =0; k < maxsimfiles; k++){
    keysim30[k] = simfile [k]->FindKey("DetEDC.R1");
    if (keysim30[k] == 0){
        cout << "!!Histogram in simfile " << k << " does not exist!!" <<endl;
        throw 1;
    }
}

```

```

for (Int_t k =0; k < maxsimfiles; k++){
    keysim140[k] = simfile [k]->FindKey("DetEDC.R2");
    if (keysim140[k] == 0){
        cout << "!!Histogram in simfile " << k << " does not exist!!" <<endl;
        throw 1;
    }
}

```

```

}

```

```

/***** 30 DEGREE SPECTRA*****/

```

```

realfile30 ->cd();
TH1D* real30 = (TH1D*)gDirectory->Get("egamdc30_in71Brout70Br");

```

```

for (Int_t l =0; l < maxsimfiles; l++){

```

```

    //scale and add linear background

```

```

    simfile [1]->cd ();
    sim30 [1] = (TH1D*)gDirectory->Get("DetEDC_R1");
    sim30 [1]->Scale(scale30);
    TF1 *fa1 = new TF1("fa1", "-0.055*x+78", 0, 1500);
    sim30 [1]->Add(fa1, 1);
}

//calculate chi-square
for (Int_t j =0; j < maxsimfiles; j++){
    total30 [j] = 0;
    for (Int_t i=minbin30; i<maxbin30; i++){
        realbinvalue30 [i-minbin30] = real30->GetBinContent(i);
        realspecerror30 [i-minbin30] = real30->GetBinError(i);
        a30 [i-minbin30][j] = realbinvalue30 [i-minbin30];

        a30_error [i-minbin30][j] = realspecerror30 [i-minbin30];

        simbinvalue30 [i-minbin30][j] = sim30 [j]->GetBinContent(i);
        b30 [i-minbin30][j] = simbinvalue30 [i-minbin30][j];

        sum30 [i-minbin30][j] = (a30 [i-minbin30][j] - b30 [i-minbin30][j]);
        total30 [j] = {total30 [j] +
            (sum30 [i-minbin30][j]*sum30 [i-minbin30][j])/
            (a30_error [i-minbin30][j]*a30_error [i-minbin30][j])};
    }
}

/***** END OF 30 DEGREE SPECTRA*****/

/***** 140 DEGREE SPECTRA*****/

realfile140->cd ();
TH1D* real140 = (TH1D*)gDirectory->Get("egamdc140_in71Brout70Br");

for (Int_t l =0; l < maxsimfiles; l++){

    //scale and add linear background
    simfile [1]->cd ();
    sim140 [1] = (TH1D*)gDirectory->Get("DetEDC_R2");
    sim140 [1]->Scale(scale140);
    TF1 *fa2 = new TF1("fa2", "-0.040*x+55", 0, 1500);
    sim140 [1]->Add(fa2, 1);

}

//calculate chi-square
for (Int_t j =0; j < maxsimfiles; j++){
    total140 [j] = 0;
    for (Int_t i=minbin140; i<maxbin140; i++){
        realbinvalue140 [i-minbin140] = real140->GetBinContent(i);

```

```

    realspecerror140[i-minbin140] = real140->GetBinError(i);
    a140[i-minbin140][j] = realbinvalue140[i-minbin140];

    a140_error[i-minbin140][j] = realspecerror140[i-minbin140];

    simbinvalue140[i-minbin140][j] = sim140[j]->GetBinContent(i);
    b140[i-minbin140][j] = simbinvalue140[i-minbin140][j];

    sum140[i-minbin140][j] = (a140[i-minbin140][j] - b140[i-minbin140][j]);
    total140[j] = {total140[j] +
    (sum140[i-minbin140][j]*sum140[i-minbin140][j])/
    (a140_error[i-minbin140][j]*a140_error[i-minbin140][j])};
}
}

/***** END OF 140 DEGREE SPECTRA*****/

//add ring spectra together
total[j] = 0;

for (Int_t j =0; j < maxsimfiles; j++){
    if (ring ==1)
        total[j] = total30[j];
    else if (ring ==2)
        total[j] = total140[j];
    else if (ring ==3)
        total[j] = total30[j] + total140[j];
    else {
        cout << "!!Invalid ring number parameter!!" <<endl;
        throw 1;
    }
}

//plot the chi-square spectrum
new TCanvas("hello");
TH1D *squarediff = new TH1D("squarediff", "squarediff", 10000, 0, 10);

for (Int_t m =0; m < maxsimfiles; m++){
    p=1000*start+500*m;
    squarediff->SetBinContent(p, total[m]);
}

squarediff->SetMarkerStyle(20);
squarediff->GetXaxis()->SetTitle("Lifetime (ps)");
squarediff->GetYaxis()->SetTitle("Difference");
squarediff->SetStats(kFALSE);
squarediff->Draw("E1");

```

```

//fitting the data points with a cubic
TF1 *fit1 = new TF1(" fit1 ", " pol3 ", 1.4, 9.1);
squareddiff->Fit(" fit1 ", " 0");
fit1->DrawCopy("SAME");

double C = fit1->GetParameter(1);
double square = fit1->GetParameter(2);
double cube = fit1->GetParameter(3);

double A = 3*cube;
double B = 2*square;

double solution1 = (-B + sqrt(B*B-4*A*C))/(2*A);
double solution2 = (-B - sqrt(B*B-4*A*C))/(2*A);

double C = fit1->GetParameter(1);
double square = fit1->GetParameter(2);
double cube = fit1->GetParameter(3);

double A = 3*cube;
double B = 2*square;

double solution1 = (-B + sqrt(B*B-4*A*C))/(2*A);
double solution2 = (-B - sqrt(B*B-4*A*C))/(2*A);

double errA = fit1->GetParError(3);
double errB = fit1->GetParError(2);
double errC = fit1->GetParError(1);

double P = -B/(2*A);
double errP = -P*sqrt((errB/B)*(errB/B)+(errA/A)*(errA/A));

double Q = sqrt(B*B-4*A*C);
double errQ = sqrt((1/(B*B-4*A*C))*(4*errA*errA+4*errC*errC+(B*B)*(errB*errB)));
double R = Q/(2*A);
double errR = R*sqrt((errQ/Q)*(errQ/Q)+(errA/A)*(errA/A));

double solerr = sqrt((errR*errR)+(errP*errP));

// the 'minimum' solution is taken
cout.precision(3);
cout << "TWO SOLUTIONS!!" << endl;
cout << "Solution One: " << solution1 << " +/- ";
cout.precision(2);
cout << solerr << ". " << endl;
cout.precision(3);
cout << "Solution Two: " << solution2 << " +/- ";
cout.precision(2);
cout << solerr << ". " << endl;
}

```

Bibliography

- [1] A. O. Macchiavelli *et al.*, Phys. Rev. C 61 (2000) 041303(R).
- [2] M. Hasegawa *et al.*, Phys. Lett. B 656 (2007) 51.
- [3] W. Nazarewicz *et al.*, Nucl. Phys. A 435 (1985) 397.
- [4] Y. Fu *et al.*, Phys. Rev. C 87 (2013) 054305.
- [5] M. Bender *et al.*, Phys. Rev. C 74 (2006) 024312.
- [6] K. Starosta *et al.*, Phys. Rev. Lett. 99 (2007) 042503.
- [7] A. Obertelli *et al.*, Phys. Rev. C 80 (2009) 031304(R).
- [8] A. Gade *et al.*, Phys. Rev. Lett. 95 (2005) 022502.
- [9] H. Iwasaki *et al.*, Phys. Rev. Lett. 112 (2014) 142502.
- [10] A. Lemasson *et al.*, Phys. Rev. C 85 (2012) 041303(R).
- [11] P. Möller *et al.*, Atom. Nucl. Data Tables 59 (1995) 185–381.
- [12] D. G. Jenkins *et al.*, Phys. Rev. C 100 (2002) 064307.
- [13] G. de Angelis *et al.*, Eur. Phys. J. A 12 (2001) 51.
- [14] G. de Angelis *et al.*, Phys. Rev. C 85 (2012) 034320.
- [15] A. Petrovici *et al.*, J. Phys. G 32 (2006) 583–597.
- [16] M. A. Bentley, S. M. Lenzi, Prog. Part. Nucl. Phys. 59 (2007) 497–561.
- [17] B. S. Nara Singh *et al.*, Phys. Rev. C 75 (2007) 061301(R).

- [18] R. K. Wallace, S. Wolsey, APJS 45 (1981) 389–420.
- [19] J. Savory *et al.*, Phys. Rev. Lett. 102 (2009) 132501.
- [20] N. Tajima, N. Suzuki, Phys. Rev. C 64 (2001) 037301.
- [21] K. Kaneko *et al.*, Phys. Rev. C 82 (2010) 061301.
- [22] K. Kaneko *et al.*, Phys. Rev. Lett. 109 (2012) 092504.
- [23] K. Kaneko *et al.*, Phys. Rev. C 89 (2014) 031302(R).
- [24] K. Kaneko *et al.*, Phys. Rev. Lett. 110 (2013) 172505.
- [25] T. Mizusaki *et al.*, Phys. Rev. C 82 (2010) 024310.
- [26] T. Mizusaki *et al.*, Acta. Phys. Pol. B 42 (2011) 447.
- [27] C. Lanczos, J. Res. Natl. Bur. Stand. 12 (2001) 51.
- [28] M. Honma *et al.*, Phys. Rev. C 80 (2009) 064323.
- [29] M. Honma *et al.*, Phys. Rev. C 69 (2004) 034335.
- [30] K. W. Schid, F. Grummer, Rep. Prog. Phys. 50 (1987) 731–781.
- [31] A. Petrovici *et al.*, Nucl. Phys. A 605 (1996) 290.
- [32] A. Petrovici *et al.*, Nucl. Phys. A 483 (1988) 317–347.
- [33] A. Petrovici *et al.*, Nucl. Phys. A 728 (2003) 396–414.
- [34] W. D. Myers, W. J. Swiatecki, Ann. Phys. N.Y. 55 (1969) 395.
- [35] W. D. Myers, W. J. Swiatecki, Ann. Phys. N.Y. 84 (1974) 186.
- [36] M. Bolsterli *et al.*, Phys. Rev. C 5 (1972) 1050.
- [37] P. Möller, J. R. Nix, Nucl. Phys. A 20 (1974) 992.
- [38] W. Heisenberg, Z. Phys. 77 (1932) 1–11.
- [39] D. D. Warner *et al.*, Nature Physics 2 (2006) 311–318.
- [40] A. V. Afanasjev, S. Frauendorf, Phys. Rev. C 71 (2005) 064318.

BIBLIOGRAPHY

- [41] J. A. Tostevin, Nucl. Phys. A 682 (2001) 320c–331c.
- [42] V. Maddalena *et al.*, Nucl. Phys. A 682 (2001) 332c–338c.
- [43] P. G. Hansen, J. A. Tostevin, Annu. Rev. Nucl. Part. Sci. 53 (2003) 219–261.
- [44] T. Glasmacher, Nucl. Phys. A 693 (2001) 90–104.
- [45] A. Gorgen, J. Phys. G 37 (2010) 103101.
- [46] H. Esbensen, Phys. Rev. C 78 (2008) 024608.
- [47] A. Winther, K. Alder, Nucl. Phys. A 319 (1979) 518–532.
- [48] A. F. Lisetskiy *et al.*, Phys. Rev. C 60 (1999) 064310.
- [49] P. A. Zavodskzy *et al.*, in: CP749, Electron Cyclotron Resonance Ion Sources - 16th International Workshop on ECR Ion Sources, 2005.
- [50] P. A. Zavodskzy *et al.*, Nucl. Instr. Meth. Phys. Res. B 241 (2005) 959.
- [51] R. Geller, IOP Publishing Ltd., London, 1996.
- [52] D. J. Morissey, Nucl. Phys. A 616 (1997) 45c–55c.
- [53] S. Gammino *et al.*, Rev. Sci. Instrum. 67 (1996) 155.
- [54] D. J. Morissey *et al.*, Nucl. Instr. Meth. Phys. Res. B 126 (2003) 316.
- [55] H. Geissel *et al.*, Annu. Rev. Nucl. Part. Sci. 405 (1995) 163–203.
- [56] D. J. Morissey *et al.*, Nucl. Instr. Meth. Phys. Res. B 204 (2003) 90.
- [57] D. Bazin *et al.*, Nucl. Instr. Meth. Phys. Res. B 204 (2003) 629.
- [58] M. Matoš *et al.*, Nucl. Instr. Meth. Phys. Res. A 696 (2012) 171.
- [59] Y. Fuchi *et al.*, in: IEEE NSS 92CH3232-6, 1992.
- [60] D. Habs *et al.*, Prog. Part. Nucl. Phys. 38 (1997) 111.
- [61] J. Eberth *et al.*, Prog. Part. Nucl. Phys. 38 (1997) 29.
- [62] I. Y. Lee *et al.*, Prog. Part. Nucl. Phys. 38 (1997) 65.
- [63] W. F. Mueller *et al.*, Nucl. Instr. Meth. Phys. Res. A 466 (2001) 492–498.

- [64] L. Sajo-Bohus *et al.*, Nucl. Instr. Meth. Phys. Res. A 648 (2011) 132–138.
- [65] J. P. Nolan, J. F. Sharpey-Schafer, Rep. Prog. Phys. 42 (1979) 1.
- [66] P. Petkov *et al.*, Nucl. Phys. A 589 (1994) 341–362.
- [67] A. Dewald *et al.*, Prog. Part. Nucl. Phys. 67 (2012) 786–839.
- [68] D. Ward *et al.*, Nucl. Phys. A 332 (1979) 433–454.
- [69] A. Chester *et al.*, Nucl. Instr. Meth. Phys. Res. A 562 (2006) 230–240.
- [70] K. S. Krane *et al.*, Nuclear Data Tables 11 (1973) 351–406.
- [71] H. Olliver *et al.*, Phys. Rev. C 68 (2003) 044312.
- [72] P. Petkov *et al.*, Nucl. Instr. Meth. Phys. Res. A 431 (1999) 208–223.
- [73] O. B. Tarasov, Eur. Phys. J. A 25 (2005) 751.
- [74] A. Dewald *et al.*, *Manuscript in preparation*.
- [75] D. P. Sanderson, W. F. Mueller, in: Proceedings of the 7th International Workshop on Accelerator Alignment, SPring-8, 2002.
- [76] D. P. Sanderson, in: 9th International Workshop on Accelerator Alignment, 2006.
- [77] R. Brun, F. Rademakers, Nucl. Instr. Meth. Phys. Res. A 389 (1997) 81–86.
- [78] M. Berz *et al.*, Phys. Rev. C 47 (1993) 537.
- [79] D. Bazin, S800 Spectrograph Inverse Map Server.
URL <http://maps.nslc.edu/~s800maps>
- [80] M. J. Martin *et al.*, Nucl. Data Sheets 114 (2013) 1497–1847.
- [81] S. Agostinelli *et al.*, Nucl. Instr. Meth. Phys. Res. A 598 (2003) 250–303.
- [82] P. J. Voss, Ph.D. thesis, Michigan State University (2011).
- [83] P. Adrich *et al.*, Nucl. Instr. Meth. Phys. Res. A 598 (2009) 454.
- [84] B. Pritychenko *et al.*, Atom. Nucl. Data Tables 98 (2012) 798–811.
- [85] A. Dewald, *Private communication*.

- [86] A. L. Nichols, B. Singh, J. K. Tuli, Nuclear Data Sheets 113 (2012) 973–1114.
- [87] N. J. Ward *et al.*, J. Phys. G 7 (1981) 815–836.
- [88] S. M. Fischer *et al.*, Phys. Rev. Lett. 84 (2000) 4064–4067.
- [89] E. A. McCutchan, Nuclear Data Sheets 113 (2012) 1735–1870.
- [90] D. Abriola, Nuclear Data Sheets 111 (2010) 1–140.
- [91] J. K. Tuli, Nuclear Data Sheets 103 (2004) 389–514.
- [92] J. Heese *et al.*, Z. Phys. A 325 (1986) 43–53.
- [93] J. Ljungvall *et al.*, Phys. Rev. Lett. 100 (2008) 102502.
- [94] E. Browne, Nuclear Data Sheets 111 (2010) 1093–1209.
- [95] R. Lüttke *et al.*, Phys. Rev. C 85 (2012) 017301.
- [96] R. Wadsworth *et al.*, J. Phys. G 5 (1979) 1761.
- [97] A. Corsi *et al.*, Phys. Rev. C 88 (2013) 044311.
- [98] L. Cleeman *et al.*, Nucl. Phys. A 334 (1980) 157.
- [99] E. A. Stefanova *et al.*, Phys. Rev. C 67 (2003) 054319.
- [100] D. G. Jenkins *et al.*, Phys. Rev. C 64 (2001) 064311.
- [101] I. Stefanescu *et al.*, Phys. Rev. C 69 (2004) 034333.
- [102] C. D. Nesaraja, Nuclear Data Sheets 115 (2014) 1–134.
- [103] E. Browne, Nuclear Data Sheets 111 (2010) 2425–2553.
- [104] H. Kawakami *et al.*, Phys. Rev. C 21 (1980) 1311–1320.
- [105] P. Banerjee *et al.*, Nuovo Cim. 110A (1997) 1365.
- [106] K. Heyde, Basic Ideas and Concepts in Nuclear Physics, IOP Publishing Ltd., London, 1994.
- [107] M. Weiszflog *et al.*, Eur. Phys. J. A 11 (2001) 25–38.
- [108] A. J. Nichols *et al.*, Phys. Lett. B 733 (2014) 52–57.

BIBLIOGRAPHY

- [109] A. P. Zuker *et al.*, Phys. Rev. Lett. 89 (2002) 142502.
- [110] K. Kaneko, *Private Communication*.
- [111] K. Kaneko *et al.*, Phys. Rev. C 89 (2014) 011302(R).
- [112] A. M. Hurst *et al.*, Phys. Rev. Lett. 98 (2007) 072501.
- [113] R. G. Thomas *et al.*, Phys. Rev. 88 (1952) 1109.
- [114] J. B. Ehrman *et al.*, Phys. Rev. 81 (1951) 412.
- [115] A. Petrovici, *Private Communication*.
- [116] P. von Brentano *et al.*, Nucl. Phys. A 682 (2001) 48c.
- [117] C. D. O’Leary *et al.*, Phys. Lett. B 459 (1999) 73.
- [118] A. Schmidt *et al.*, Phys. Rev. C 62 (2000) 044319.
- [119] G. Morpurgo, Phys. Rev. 110 (1958) 721.
- [120] C. A. Betulani, P. G. Hansen, Phys. Rev. C 70 (2004) 034609.
- [121] S. M. Fischer *et al.*, Phys. Rev. C 72 (2005) 024321.
- [122] E. Simpson, *Private communication*.
- [123] E. Caurier, F. Nowacki, Acta. Phys. B 30 (1999) 705.
- [124] R. Anholt *et al.*, Phys. Rev. Lett. 53 (1984) 234–237.
- [125] J. A. Bearde, A. F. Burr, Rev. Mod. Phys. 39 (1967) 125–142.